LBL-7061 c.2
SAC-22
UC-70

SWEDISH-AMERICAN COOPERATIVE PROGRAM ON RADIOACTIVE WASTE STORAGE IN MINED CAVERNS IN CRYSTALLINE ROCK

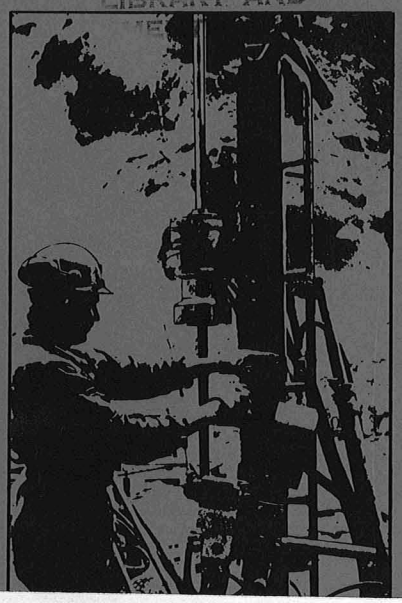

Technical Information Report No. 22

CALCULATED THERMALLY INDUCED DISPLACEMENTS AND STRESSES FOR HEATER EXPERIMENTS AT STRIPA, SWEDEN

Linear Thermoelastic Models Using Constant Material Properties

Tin Chan
Lawrence Berkeley Laboratory
University of California
Berkeley, California 94720

Neville G. W. Cook
Department of Materials Science and Mineral Engineering
University of California
Berkeley, California 94720

December 1979

t Project of

Swedish Nuclear Fuel Supply Co.
Fack 10240 Stockholm, Sweden

Operated for the Swedish
Nuclear Power Utility Industry

Lawrence Berkeley Laboratory
Earth Sciences Division
University of California
Berkeley, California 94720, USA

Operated for the U.S. Department of
Energy under Contract W-7405-ENG-48

LBL-7061
SAC-22
UC-70

CALCULATED THERMALLY INDUCED DISPLACEMENTS AND STRESSES FOR HEATER EXPERIMENTS AT STRIPA, SWEDEN

Linear Thermoelastic Models Using Constant Material Properties

Tin Chan

Lawrence Berkeley Laboratory
University of California
Berkeley, California 94720

Neville G. W. Cook

Department of Materials Science and Mineral Engineering
University of California
Berkeley, California 94720

This report was prepared by Lawrence Berkeley Laboratory under the University of California contract W-7405-ENG-48 with the Department of Energy. The contract is administered by the Office of Nuclear Waste Isolation at Battelle Memorial Institute, Columbus, Ohio.

This report is one of a series documenting the results of the Swedish-American cooperative research program in which the cooperating scientists explore the geological, geophysical, hydrological, geochemical, and structural effects anticipated from the use of a large crystalline rock mass as a geologic repository for nuclear waste. This program has been sponsored by the Swedish Nuclear Power Utilities through the Swedish Nuclear Fuel Supply Company (SKBF), and the U.S. Department of Energy (DOE) through the Lawrence Berkeley Laboratory (LBL).

The principal investigators are L.B. Nilsson and O. Degerman for SKBF, and N.G.W. Cook, P.A. Witherspoon, and J.E. Gale for LBL. Other participants will appear as authors of the individual reports.

Previous technical reports in this series are listed below.

1. Swedish-American Cooperative Program on Radioactive Waste Storage in Mined Caverns by P. A. Witherspoon and O. Degerman (LBL-7049, SAC-01).

2. Large Scale Permeability Test of the Granite in the Stripa Mine and Thermal Conductivity Test by Lars Lundstrom and Haken Stille (LBL-7052, SAC-02).

3. The Mechanical Properties of the Stripa Granite by Graham Swan (LBL-7074, SAC-03).

4. Stress Measurements in the Stripa Granite by H. Carlsson (LBL-7078, SAC-04).

5. Borehole Drilling and Related Activities at the Stripa Mine by Pavel J. Kurfurst, T. Hugo-Persson, and G. Rudolph (LBL-7080, SAC-05).

6. A Pilot Heater Test in the Stripa Granite by Hans Carlsson (LBL-7071, SAC-06).

7. An Analysis of Measured Values for the State of Stress in the Earth's Crust by Dennis B. Jamison and Neville G. W. Cook (LBL-7071, SAC-07).

8. Mining Methods Used in the Underground Tunnels and Test Rooms at Stripa by B. Andersson and P. A. Halen (LBL-7081, SAC-08).

9. Theoretical Temperature Fields for the Stripa Heater Project by Tin Chan, Neville G. W. Cook, and Chin-Fu Tsang (LBL-7082, SAC-09).

10. Mechanical and Thermal Design Considerations for Radioactive Waste Repositories in Hard Rock. Part I: An Appraisal of Hard Rock for Potential Underground Repositories of Radioactive Wastes by Neville G. W. Cook; Part II: In Situ Heating Experiments in Hard Rock: Their Objectives and Design by Neville G. W. Cook and Paul A. Witherspoon (LBL-7073, SAC-10).

11. Full-Scale and Time-Scale Heating Experiments at Stripa: Preliminary Results by Neville G. W. Cook and Michael Hood (LBL-7072, SAC-11).

12. Geochemistry and Isotope Hydrology of Groundwaters in the Stripa Granite: Results and Preliminary Interpretation by P. Fritz, J. F. Barker, and J. E. Gale (LBL-8285, SAC-12).

13. Electrical Heaters for Thermo-mechanical Tests at the Stripa Mine by R. H. Burleigh, E. P. Binnall, A. O. DuBois, D. U. Norgren, and A. R. Ortiz (LBL-7063, SAC-13).

14. Data Acquisiton, Handling and Display for the Heater Experiments at Stripa by Maurice B. McEvoy (LBL-7062, SAC-14).

15. An Approach to the Fracture Hydrology at Stripa: Preliminary Results by J. E. Gale and P. A. Witherspoon (LBL-7079, SAC-15).

16. Preliminary Report on Geophysical and Mechanical Borehole Measurements at Stripa by P. Nelson, B. Paulsson, R. Rachiele, L. Andersson, T. Schrauf, W. Hustrulid, O. Duran, and K. A. Magnusson (LBL-8280, SAC-16).

17. Observations of a Potential Size-Effect in Experimental Determination of the Hydraulic Properties of Fractures by P. A. Witherspoon, C. H. Amick, J. E. Gale, and K. Iwai (LBL-8571, SAC-17).

18. Rock Mass Characterization for Storage of Nuclear Waste in Granite by P. A. Witherspoon, P. Nelson, T. Doe, R. Thorpe, B. Paulsson, J. Gale, and C. Forster (LBL-8570, SAC-18).

19. Fracture Detection in Crystalline Rock Using Shear Waves by K. H. Waters, S. P. Palmer, and W. E. Farrell (LBL-7051, SAC-19).

20. Characterization of Discontinuities in the Stripa Granite -- Time-Scale Heater Experiment by Richard Thorpe (LBL-7083, SAC-20).

21. Geology and Fracture System at Stripa by A. Olkiewicz, J. E. Gale, R. Thorpe, and B. Paulsson (LBL-8907, SAC-21).

TABLE OF CONTENTS

LIST OF FIGURES

Page

Page

LIST OF TABLES

ABSTRACT

Thermally induced displacements and stresses have been calculated by finite element analysis to guide the design, operation, and data interpretation of the in situ heating experiments in a granite formation at Stripa, Sweden. There are two full-scale tests with electrical heater canisters comparable in size and power to those envisaged for reprocessed high level waste canisters and a time-scaled test. To provide a simple theoretical basis for data analysis, linear thermoelasticity was assumed. Constant (temperature-independent) thermal and mechanical rock properties were used in the calculations. These properties were determined by conventional laboratory testing on small intact core specimens recovered from the Stripa test site. Two-dimensional axisymmetric models were used for the full-scale experiments, and three-dimensional models for the time-scaled experiment. Highest compressive axial and tangential stresses are expected at the wall of the heater borehole. For the 3.6 kW full-scale heater experiment, maximum compressive tangential stress was predicted to be below the unconfined compressive strength of Stripa granite, while for the 5 kW experiment, the maximum was approximately equal to the compressive strength before the concentric ring of eight 1 kW peripheral heaters was activated, but would exceed that soon afterwards. Three zones of tensile thermomechanical stresses will occur in each full-scale experiment. One of these, just beneath the floor of the heater drift, persists throughout most of the duration of the experiment, with largest tensile stresses comparable to the in situ stresses as well as to the tensile strength of Stripa granite. Maximum vertical displacements range from a fraction of a millimeter over

most of the instrumented area of the time-scaled experiment to a few millimeters in the higher-power full-scale experiment. Radial displacements are typically half or less than vertical displacements. The predicted thermomechanical displacements and stresses have been stored in an on-site computer to facilitate instant graphic comparison with field data as the latter are collected.

1. INTRODUCTION

Among the many alternatives that have been suggested (American Physical Society, 1978) for isolating high-level nuclear waste (reprocessed or unreprocessed spent fuel) from the biosphere, burial in deep underground caverns in a geologically stable formation appears to be the most practicable. An important difference between a nuclear waste repository and an ordinary underground excavation is that nuclear wastes generate heat by radioactive decay. Some effects of this heat are: (1) thermally induced stress in the rock, the wastes, and their containers, (2) ground water convection, and (3) accelerated chemical reactions. Thermally induced stresses are important in several respects (Cook and Witherspoon, 1978). First, high compressive stress may cause borehole decrepitation, thereby complicating waste retrieval should that be necessary. Second, if the waste is to remain retrievable for several decades, for example, then the thermal stresses must be taken into consideration in the design of the excavations for the repository, to ensure that they will not fail under the combined effects of the thermal and excavation-induced stresses. Finally, thermally induced tensile stress will reduce the effective compressive stress in the rock mass, leading to higher fracture permeability.

To understand the response of the rock to thermal loading, a suite of in situ electrical heater experiments is being conducted in a granite mass at the Stripa mine in Guldsmedshyttan, Sweden, as part of the Swedish-U.S. Cooperative Program on Radioactive Waste Storage in Mined Caverns in Crystalline Rock (Witherspoon and Degerman, 1978).

Temperature, displacement, and stress fields around the heaters have been calculated in advance to guide the design and operation of the experiments and to provide predicted data that have been stored in an on-site MODCOMP-IV computer for instant graphic comparison with field data. Description of the data acquisition, handling, and display system can be found in McElvoy (1979). The real-time comparison is important for prompt interpretation of the field data and for monitoring. This comparison, in turn, should indicate the essential physical processes that must be incorporated into a mathematical model. The authors hope this iterative procedure between theory and experiment will eventually lead to a viable predictive model for a nuclear waste repository. Temperature calculations have been reported previously (Chan, Cook, and Tsang, 1978). Displacement and stress calculations are the topics of the present report.

In the present study, thermally induced displacements and stresses were calculated using linear thermoelastic finite element models in which the rock mass was assumed to be a homogeneous, isotropic continuum with temperature-independent material properties. This approach may appear simplistic since it is known from mining and other rock mechanics experience that (1) rock properties may be temperature dependent and (2) crystalline rock masses are often heterogeneous and anisotropic and may contain discontinuities with nonlinear constitutive relationships. The rationale for this approach is as follows: (1) at the time of the initial calculations there was inadequate laboratory data on the thermal and mechancial properties of Stripa granite, and (2) there was (and still is) insufficient empirical experience with the thermomechanical response of such rock masses to permit an <u>a priori</u> choice

among different theoretical constitutive models. If a compilicated model was used and it did not correctly predict the experimental data, it would be difficult to interpret the results in terms of physical process. In contrast, by carefully analyzing the discrepancies between the field data and a simple linear model, it may be possible to decipher the actual physical mechanisms and decide on the direction of further modeling efforts.

Thermal stresses may be caused by (a) differential thermal expansion due to thermal gradients, (b) external constraints to thermal expansion, or (c) differential thermal expansion of the various grains in a polymineralic rock, or of individual grains with different orientations in a monomineralic rock in a uniform temperature field, or a combination thereof. The thermo-mechanical models in the present work only account for the macroscopic thermal stresses due to causes (a) and (b) above.

Three series of thermomechanical models have been run for the Stripa project. The first series was undertaken to aid experimental design, and a combination of thermal and thermo-mechanical properties was chosen to yield the highest possible displacements and stresses that can be reasonably expected. Typical results were reported by Chan, Cook, and Tsang (1977). This series is of lesser interest at the present stage and will not be reported here. Average material properties from laboratory measurements on small specimens of Stripa granite were used for Series 2 and Series 3. These latter two series differ only in the assumed power schedules for the heaters engendered by revisions of the test strategy.

In presenting the results, the following system of sign conventions has been adopted:

1) compressive stress is positive;
2) relative displacement between two spatial points is positive if it represents contraction;
3) absolute displacement in the positive direction of a coordinate is positive.

Items (1) and (2) conform to standard rock mechanics usage (Jaeger and Cook, 1976). The sign convention (3) was chosen so that most of the quantitites plotted are positive.

2. HEATER EXPERIMENTS BEING MODELED

The three heater experiments at Stripa have been described in previous SAC[1] reports (Witherspoon and Degerman, 1978; Cook and Witherspoon, 1978; Chan, Cook, and Tsang, 1978). For easy reference a brief summary is given below.

There are a total of three heater experiments, two full-scale experiments, and one time-scaled experiment. The full-scale experiments will assess the short-term local thermal and thermomechanical responses of the granite rock mass in the immediate vicinity of an individual nuclear waste canister while the time-scaled experiment will provide field data for the interaction between adjacent waste canisters for two different spacings over a period of time equivalent to about two decades.

[1]Swedish-American Cooperative Program on Radioactive Waste Storage in Mined Caverns in Crystalline Rock.

2.1. Full-Scale Experiments

The full-scale experiments consist of electrical heaters, with sizes and thermal powers comparable to actual nuclear waste canisters, placed in vertical drill holes on the floor of a drift 338 m below surface. One of the full-scale tests employs a single heater (designated H9) operated at a constant power output of 3.6 kW. This corresponds to a full-size canister of reprocessed PWR (pressurized water reactor) high-level waste 5 years after reprocessing, with reprocessing occurring 150 days after the spent fuel has been removed from the reactor (Kisner et al., 1977, LLewellyn, 1978). This experiment is referred to as Full-Scale Experiment 1 and the heater as H9. The other experiment (hereafter referred to as Full-Scale Experiment 2) consists of a 5 kW (corresponding to a high-level waste canister 3.6 years after reprocessing) central heater (designated H10) surrounded by a concentric ring of eight longer and slimmer peripheral heaters operated at a nominal power of 1 kW each. These peripheral heaters will be energized at an appropriate stage of the experiment to simulate the rise in ambient rock temperature due to the thermal interaction between adjacent waste canisters in a repository after a few decades. Calculations (Chan, Cook, and Tsang, 1978) have shown that an almost uniform temperature distribution will be produced by this ring of peripheral heaters within its circumference about one month after they have been turned on. Fig. 1 illustrates the configuration of the full-scale experiment while Table 1 lists the dimensions.

2.2. Time-Scaled Experiment

The Time-Scaled Experiment takes advantage of the quadratic relationship between time and distance to accelerate the time development by a factor of

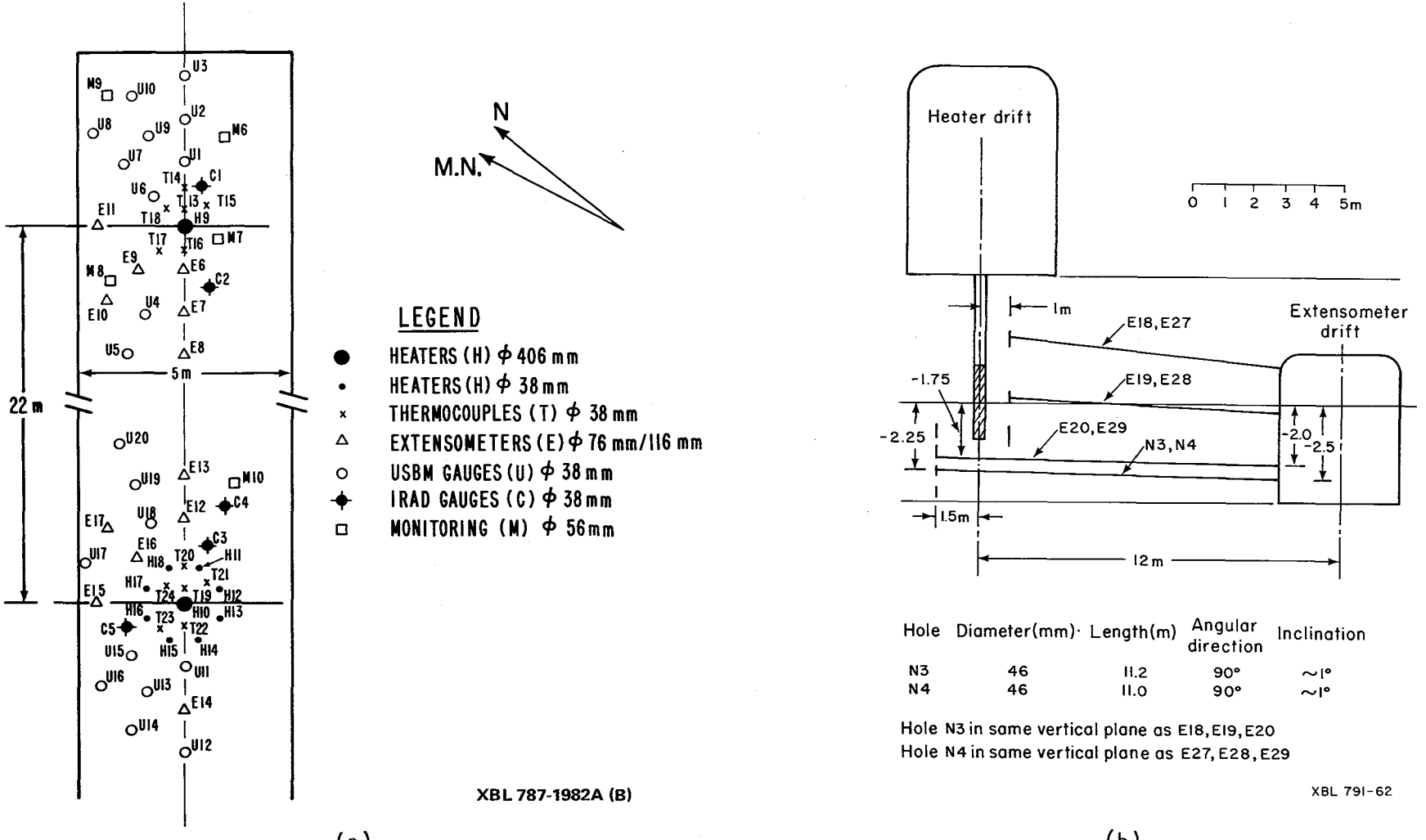

Fig. 1. Full-scale heater experiments, (a) plan view of heater drift showing borehole layout (after Kurfurst et al., 1978), (b) vertical section through heater and extensometer drifts (after Nelson et al., 1979, original design drawing by Hustrulid, 1977, unpublished).

Table 1. Dimensions of the full-scale heater experiments

Length of central heater canister	2.59 m	(8.5 ft)
Length of hot section of heater element	2.44 m	(8 ft)
Diameter of central heater canister	.324 m	(12.75 in)
Diameter of central heater hole	0.406 m	(16 in)
Length of peripheral heater	4.27 m	(14 ft)
Diameter of peripheral heater hole	0.038 m	(1.5 in)
Radius of the ring of peripheral heaters	0.9 m	(35.4 in)
Depth of the midplane of the heater array below the floor of the drift	4.25 m	(14 ft)
Center-to-center separation between the two experiments	22 m	(72.2 ft)

10.2 by scaling linear dimensions down by a factor of 3.2. Configuration and dimensions of the time-scaled heater array are shown in Fig. 2. The heaters are placed in drill holes such that the midplane of the array is 10 meters below the time-scaled drift. Each of the time-scaled heaters has an initial thermal output of 1.125 kW (equivalent to 3.6 kW in full scale), which is reduced continually to represent radioactive decay of the high-level waste as illustrated in Fig. 3. Note that in the power decay curve used in the temperature calculations for the time-scaled experiment the decay rate has been accelerated by a factor of 10.2, i.e., the time axis in Fig. 3 is the experiment time, not real time. This is necessary to maintain similitude. During the actual experiment, the decay in heater power has been delayed for two weeks due to some technical problems not related to the reduction of the heater power.

3. FINITE ELEMENT THERMOMECHANICAL MODELS

3.1. Numerical code used

Thermally induced displacements and stresses were calculated using the finite element program SAPIV (Bathe, et al., 1974). The LBL-LLL version of SAPIV (Sacket, 1978, unpublished) incorporates a bandwidth minimizer and a COMPASS (CDC assembly language) subroutine for dynamic core allocation at execution time to allow effective use of small and large core memory spaces in order to handle both small and large problems efficiently. Another improvement is that for computation of nodal loads due to thermal strains in the two-dimensional element a bilinear interpolation expansion involving the isoparametric shape functions is used for the temperature change. This provides more accurate thermal loads than the arithmetic mean temperature

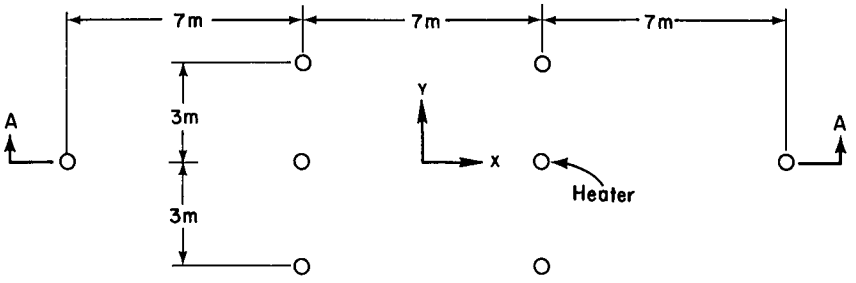

(a)

XBL782-230

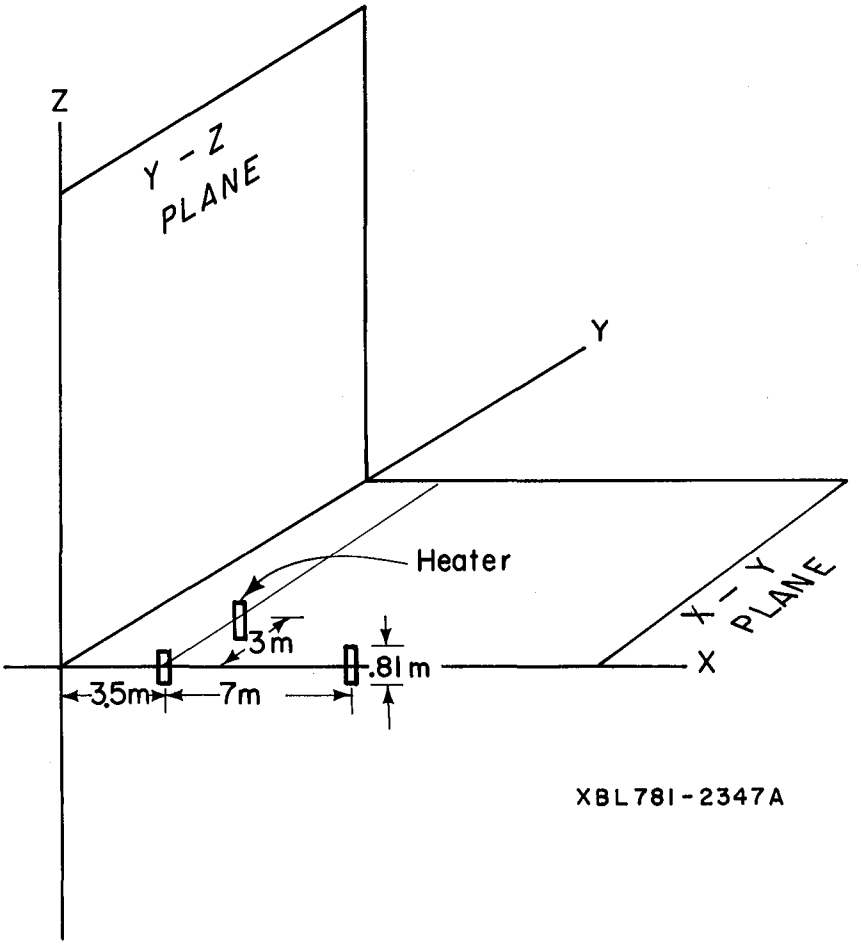

XBL781-2347A

(b)

Fig. 2. Configuration of time-scaled heater experiment illustrating the coordinate system adopted: (a) plan view, (b) cut-away view.

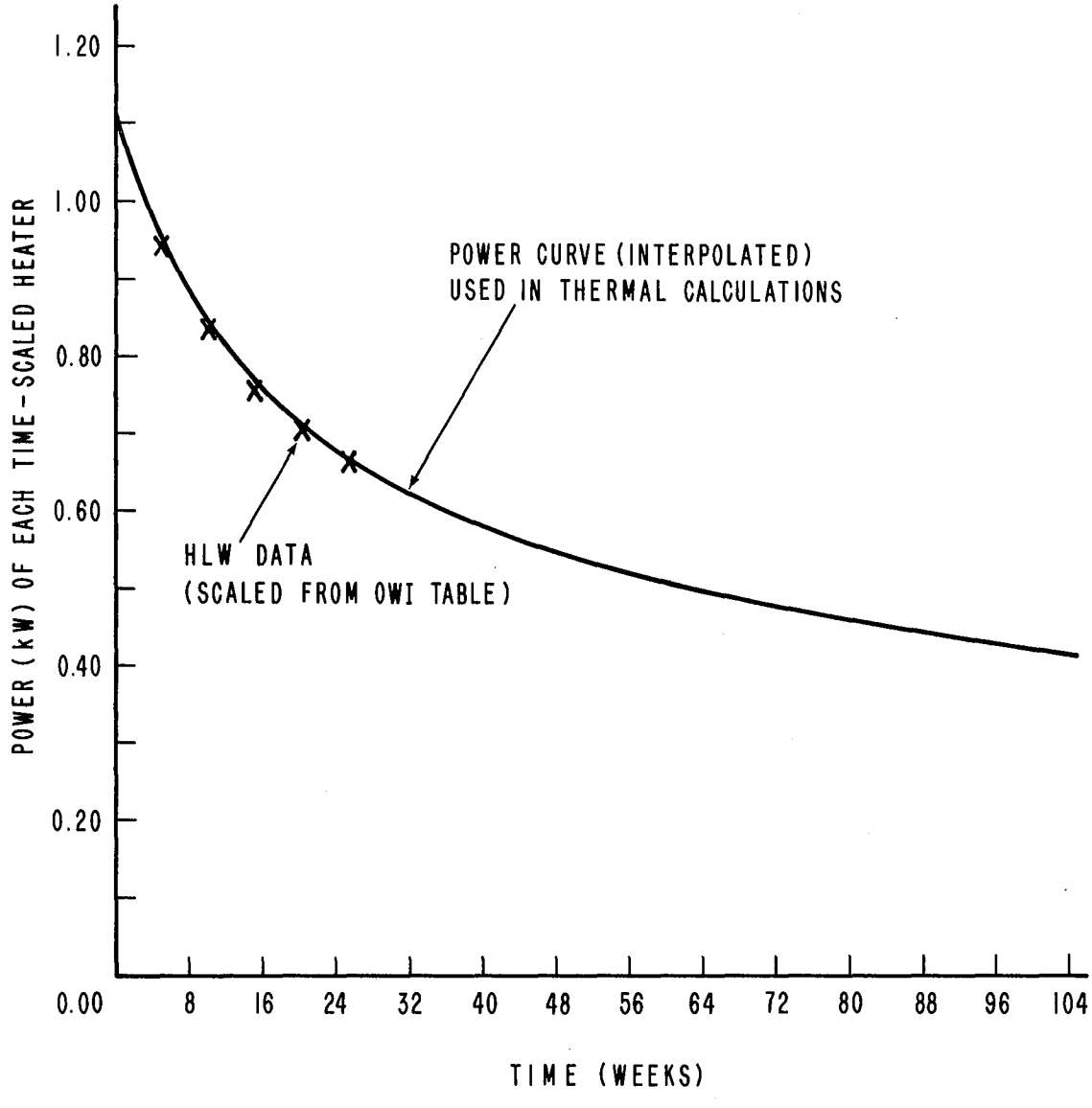

Fig. 3. Heater power decay curve used in the temperature calculations for the time-scaled experiment.

change employed in the original version. Our temperature program FILINE, based on the Green's function method (Chan, Cook, and Tsang, 1978), has been interfaced with SAPIV for thermomechanical analysis. The SAPIV program assumes linear thermoelasticity.

3.2. Assumptions and approximations

In the present calculations, the rock medium is further approximated as a homogeneous, isotropic continuum with temperature-independent properties. This is necessary because of the lack of data on *in situ* rock mass properties and conditions at the time these calculations commenced. Actually, the finite element method is the best numerical method available for modeling heterogeneities, and and the SAPIV program can handle orthotropic, temperature-dependent material properties. Calculations are now being undertaken using temperature-dependent elastic properties, and these will be reported separately.

In constructing the finite element models for the full-scale experiments, two other approximations were introduced:

1) The system is radially symmetric about the axis of the central heater.
2) The midplane of the heater array is a plane of symmetry.

3.3. Finite element meshes and boundary conditions

3.3.1. *Full-scale Experiments*. Two finite element discretization schemes, i.e., meshes, have been used. The first (hereafter referred to as Mesh 1 or M1), consisting of 651 nodes and 607 4-node isoparametric quadrilateral elements, considers the rock medium (except for the central heater

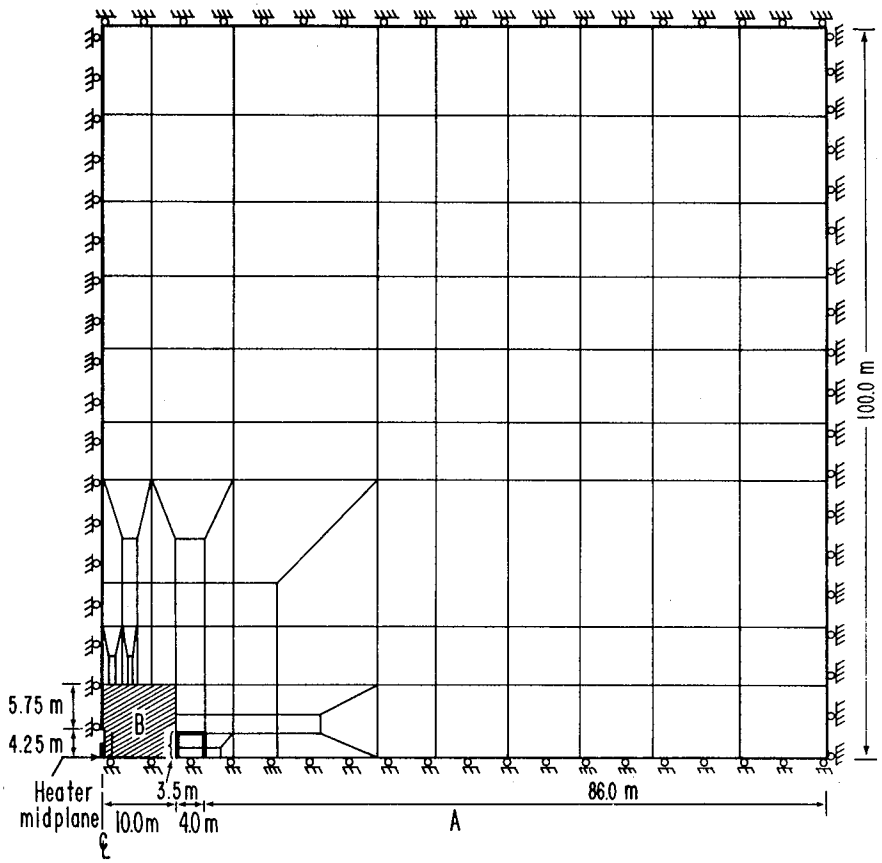

FINITE ELEMENT MESH AND BOUNDARY CONDITIONS FOR FULL SCALE HEATER EXPERIMENT 2.

XBL 786-1962A

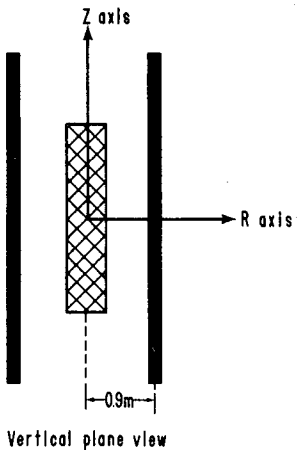

XBL 787-1993

INSET

Fig 4a. Finite element model (mesh) for each full-scale experiment. Inset illustrates the coordinate system used.

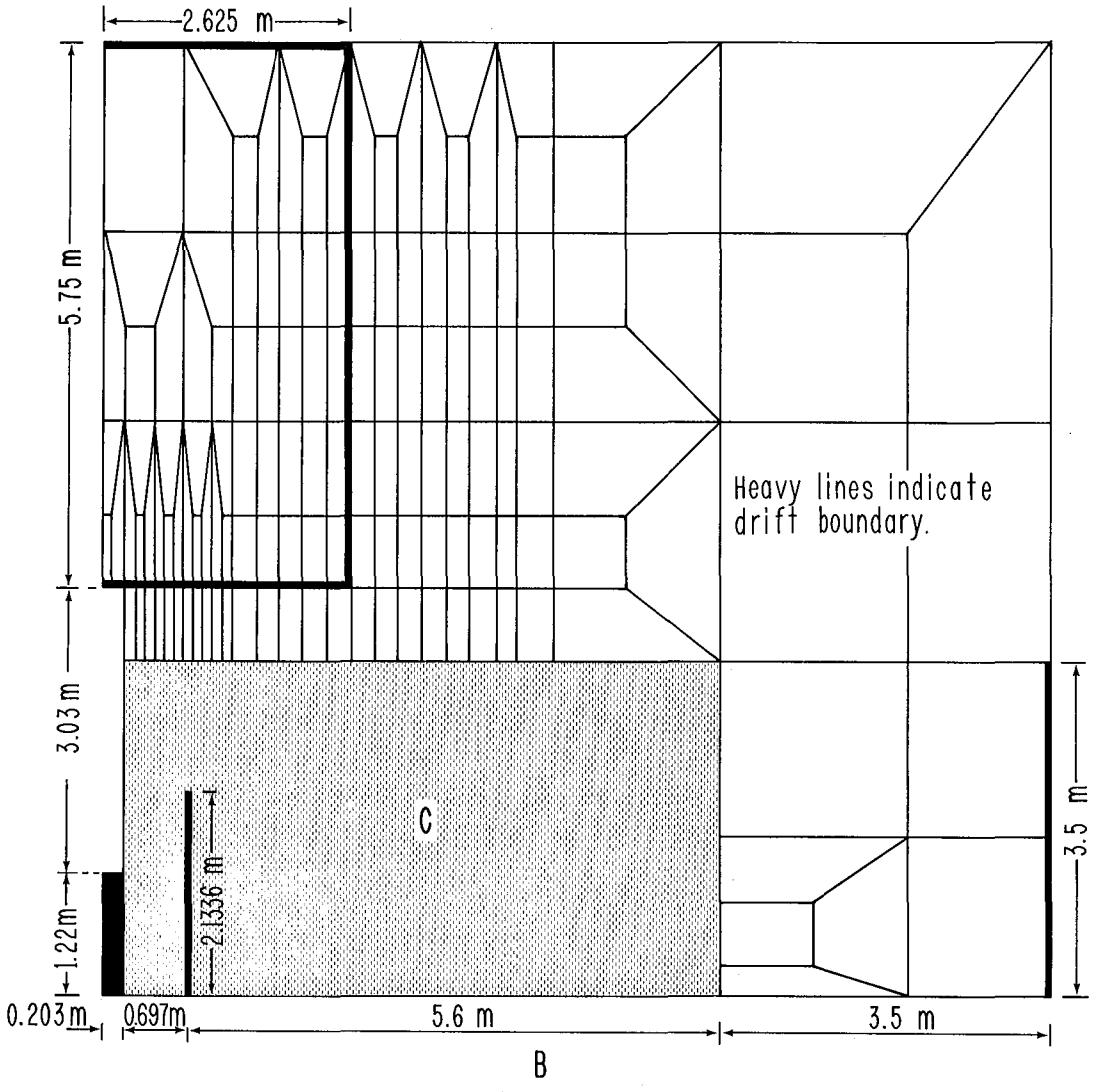

DETAILS OF AREA "B" IN "A".

XBL 786 – 1964 / C

Fig. 4b. Details of area "B" in Fig. 4a.

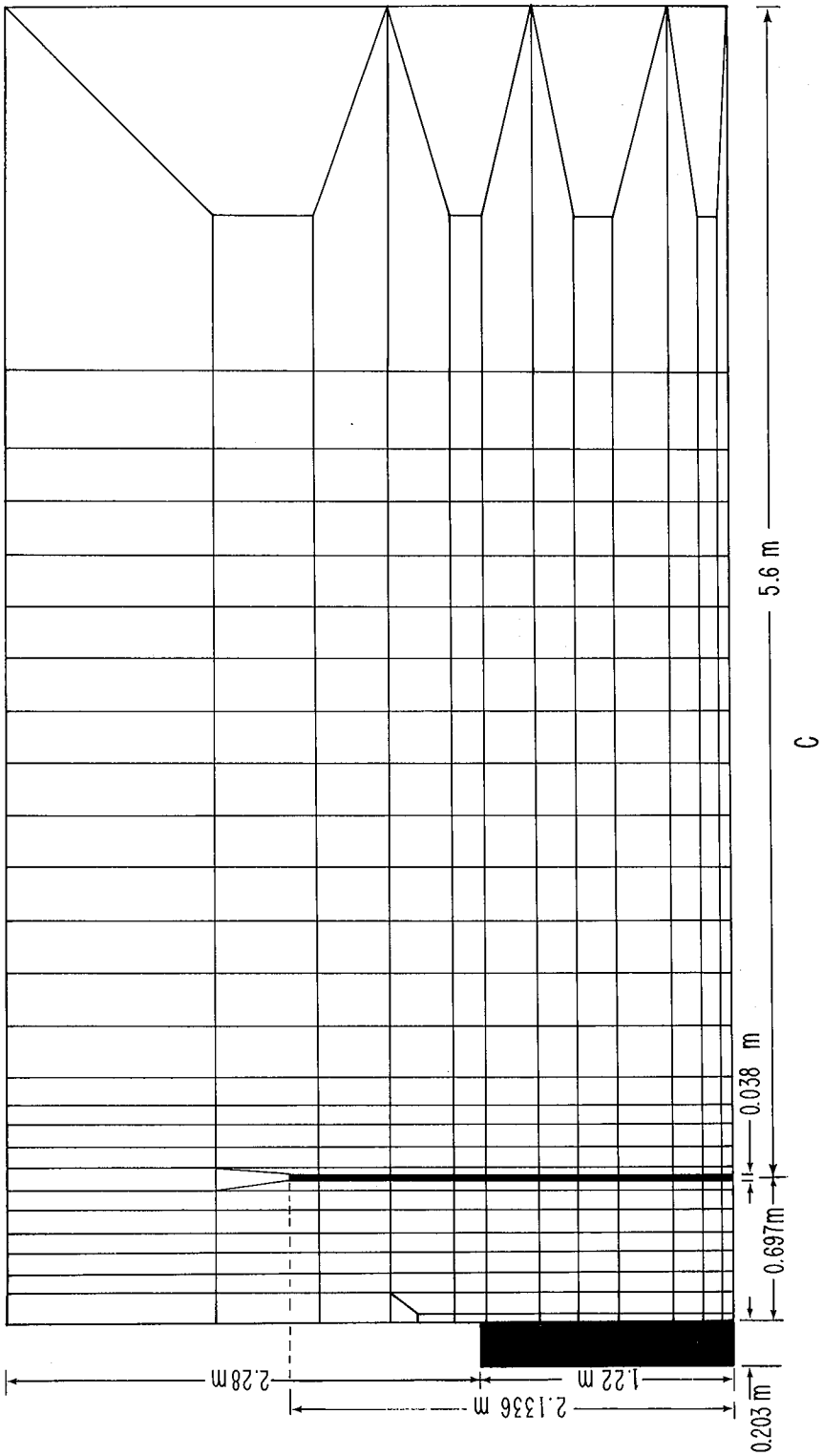

XBL 786-1965A/C

Fig. 4c. Details of area "C" in Fig. 4b.

hole) as an infinite medium. This mesh is illustrated in Figs. 4a - 4c to different degrees of detail. In the second mesh (hereafter referred to as Mesh 7 or M7), the elements within the heater drift and extensometer drift, indicated by heavy lines in the figures, are removed.[2] Zero normal displacement boundary conditions were applied to the external horizontal and vertical boundaries of the 100 m by 100 m model block. Note that, by virtue of the approximations (1) and (2) stated in the preceding paragraph, the left edge of Fig. 4a is an axis of symmetry, and the bottom edge is a mirror plane.

In the initial stage, various intermediate meshes (designated Meshes 2-6) have been constructed and used to explore the effects of different boundary and loading conditions and the trade-off between mesh fineness and computational cost. Meshes 1 and 7 were found to be sufficiently accurate representations of the physical system at a reasonable cost. Accordingly, only these latter two meshes were utilized in production runs.

In constructing the finite element models for the full-scale experiments, extra caution has been exercised to satisfy the following constraints:

1) The thermal gradient is very steep within a radius of 1 m from the axis of the central heater (Chan, Cook, aand Tsang, 1978), and, therefore, the mesh has to be very fine there.
2) Because thermally induced displacements are cumulative and pervasive, the outer (zero normal displacement) boundaries of the model have to be located very far away from the heaters, even though the temperature fields are quite localized.

[2] In practice, a very low value of Young's modulus was assigned to these elements.

3) There should be an output point for displacement or stress at every location where there is an extensometer anchor or a "stress meter" (USBM or IRAD gauge) to avoid the need for two-dimensional interpolation which may introduce further inaccuracies.

Before making production runs with the present finite element models, we have verified that our models satisfy the constraint (1) stated above by comparison with the classical analytic linear thermoelastic solution (Timoshenko and Goodier, 1951) for an infinite-length hollow cylinder with a radial temperature distribution and constraint (2) by comparison with the results obtained by applying alternative loading to Mesh 7. Sample results of this comparison are discussed in Section 4. Details are given in Appendix A.

It should be noted that the use of an axisymmetric model implies that the heater drift is approximated as a cylindrical room while the extensometer drift is approximated as a toroidal tunnel: this is necessary to avoid the need for using truly three-dimensional models which would be prohibitively expensive if the same degree of detail were to be maintained. The implications of the axisymmetric approximation are discussed in the next section in the light of results.

The finite element meshes for the two full-scale heater experiments are identical. The thermomechanical calculations for the two experiments differ only in the input temperature distributions, which were generated by means of three-dimensional analytic solutions.

3.3.2. Time-Scaled experiment. The geometry of the Time-Scaled Experiment (see Fig. 2) requires a three-dimensional model. Taking advantage of the existence of three orthogonal planes of symmetry we have discretized only one octant of space, as illustrated in Fig. 5, where (a) is the isometric view while (b), (c), and (d) are projections onto the three coordinate planes. Again heavy lines in the figures indicate the boundary of the time-scaled heater drift. A total of 1246 nodes and 924 8-node hexahedron elements have been used.

Practical limitations due to the three-dimensional nature of the Time-Scaled Experiment restricted the thermomechanical model to a coarse mesh, which ignored the presence of the heater holes. Consequently the predicted displacements and stresses would be less accurate than those for the full-scale experiments.

3.4. Applied loads

Since all the extensometers and "stress meters" were installed in the presence of the excavations and *in situ* stresses, only thermally induced changes will be detected. Hence, only these have been calculated. In the full-scale models, only thermal loads are applied to the structure yielding directly thermally induced displacements and stresses. In the time-scaled model, zero normal displacement boundary conditions cannot be used because the outer boundaries of the model cannot be moved sufficiently far away from the region of interest without incurring enormous computational expenses. To overcome this difficulty *in situ* stresses were applied to the outer boundaries and thermal loads and gravity (body force) were applied to each element.

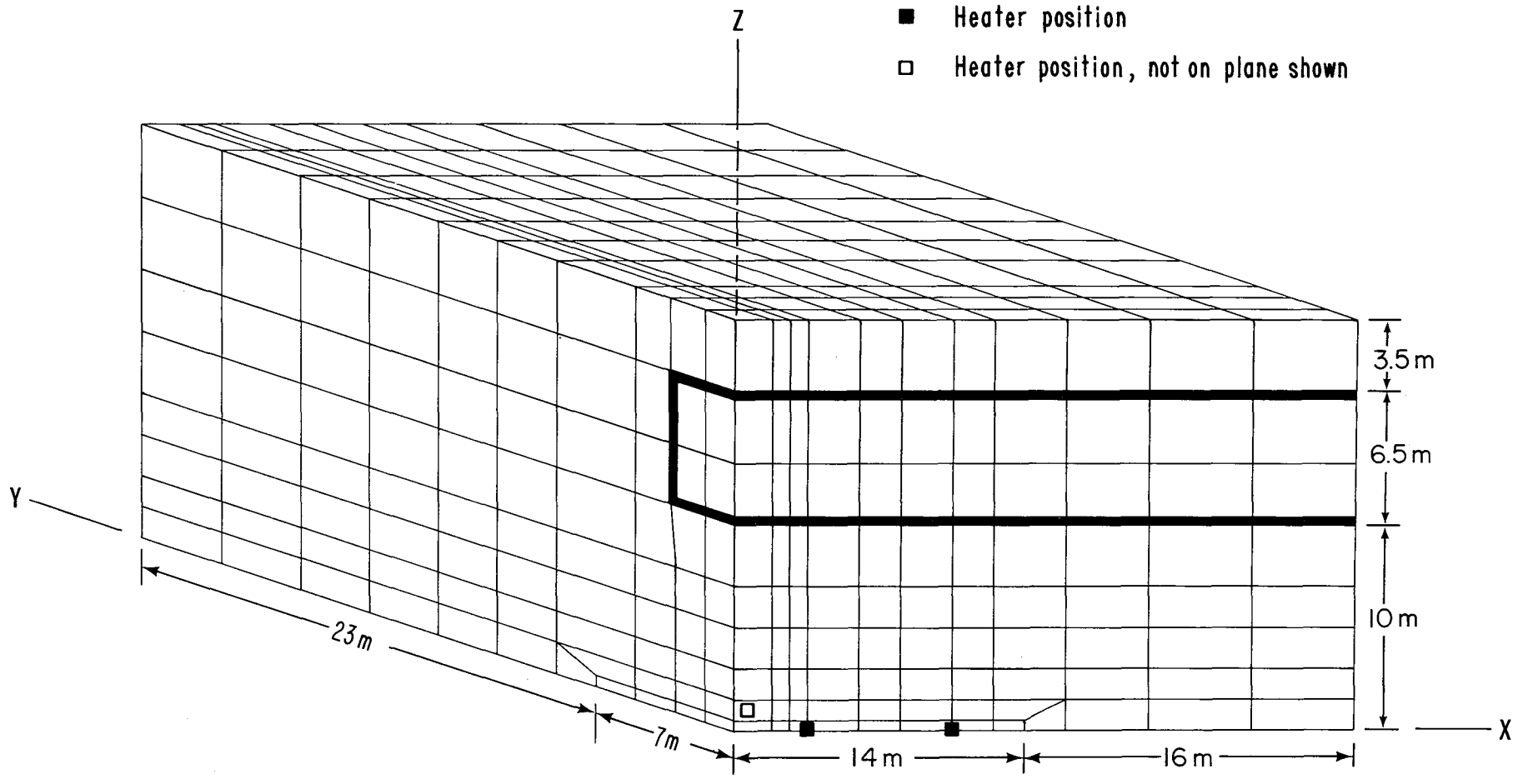

STRIPA PROJECT 3-DIMENSIONAL VIEW

Finite element mesh for thermal stresses and displacements analysis, symmetric with respect to planes X=0m., Y=0m. and Z=0m.

XBL 787-1980A

Fig. 5a. Finite element mesh for the time-scaled experiment. Heaters not drawn to scale. Heavy line represents drift boundary.

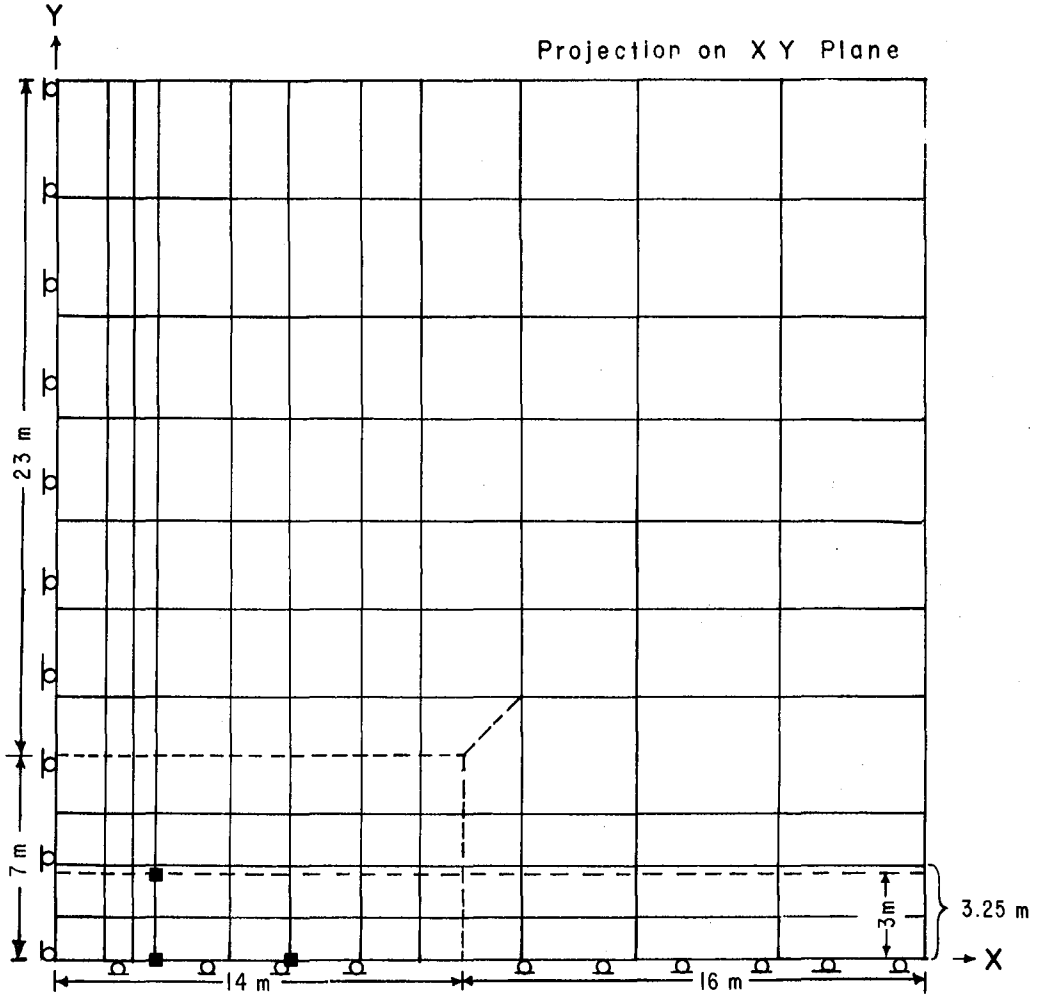

FINITE ELEMENT MESH FOR TIME SCALE HEATER EXPERIMENT.

XBL 787-1976A

Fig. 5b. Finite element mesh for the time-scaled heater experiment, projection on XY-plane.

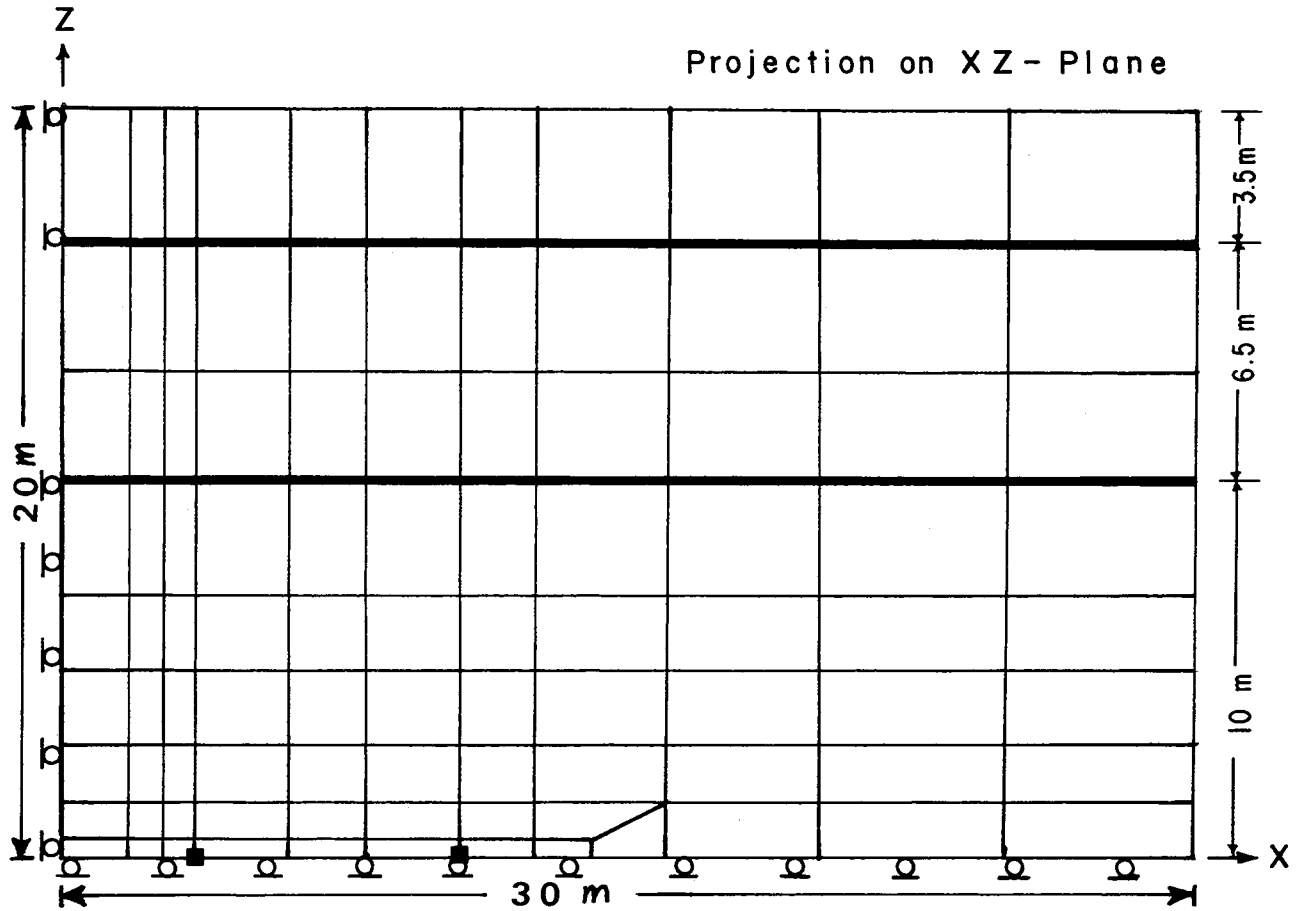

FINITE ELEMENT MESH FOR TIME SCALE HEATER EXPERIMENT.

XBL 787-1977A

Fig. 5c. Finite element mesh for the time-scaled heater experiment, projection on XZ-plane.

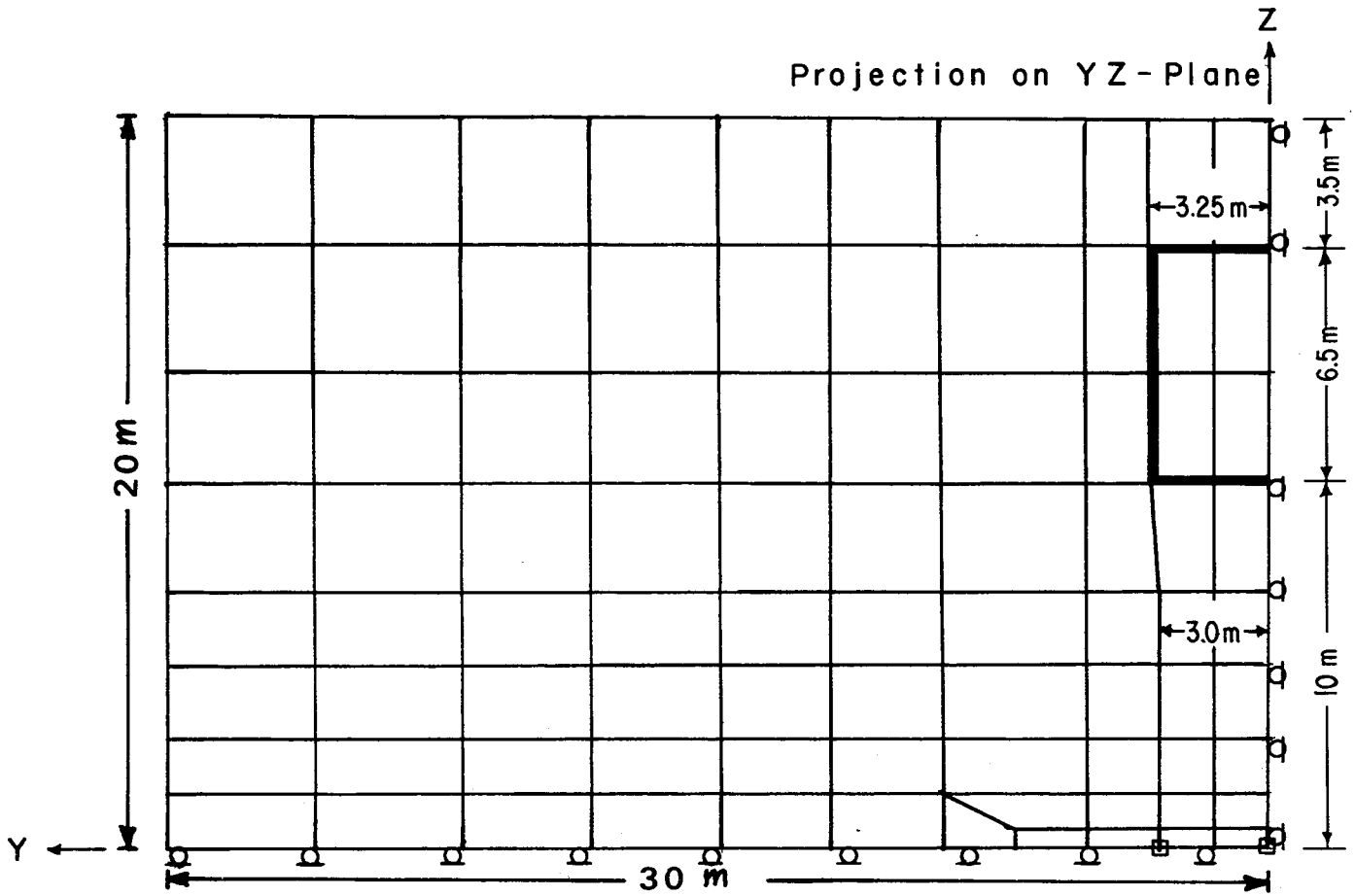

FINITE ELEMENT MESH FOR TIME SCALE HEATER EXPERIMENT.

XBL 787-1978A

Fig. 5d. Finite element mesh for the time-scaled heater experiment, projection on the YZ-plane.

A reference state of stress was also calculated with the same mechanical loads but without the thermal loads. Assuming linear elasticity, the thermally induced displacements and stresses were obtained by taking differences.

3.5. Material properties and heater powers

Three different series of the thermomechanical calculations have been carried out to date. In all three series the same finite element meshes have been used. They differ only in the choice of material properties or heater powers. These are summarized in Table 2.

3.5.1. Model Series 1. Thermomechanical Model Series 1 was undertaken in the predesign phase to guide the design of heaters, choice of heater power, and layout of instrumentation. A combination of thermal and mechanical properties were chosen to yield a conservative estimate, i.e., the highest possible thermal displacements and stresses that can be reasonably expected. From the theory of linear thermoelasticy (Timoshenko and Goodier, 1951), it is known that thermally induced displacements and stresses both vary directly with temperature and are proportional to the following combinations of material parameters

$$D = \alpha\left(\frac{1 + \nu}{1 - \nu}\right) \quad \text{for displacement} \tag{1}$$

and

$$S = \frac{\alpha E}{1 - \nu} \quad \text{for stress} \tag{2}$$

in an axisymmetric system. Here,

α = linear coefficient of thermal expansion

ν = Poisson's ratio

E = Young's modulus.

Table 2. Summary of the three series of thermoelastic models.

Model Series[a]	Material Properties	Experiment	Heaters	Heater power Time (days)	Heater power Power (kW)	Comments
1	Set 1 in Table 3	Full-Scale 1	H9	0 - 730	3.6	b
		Full-Scale 2	Central Heater H10	0 - 730	5.0	b
			Peripheral Heaters H11-H18	0 - 730	1.0	
		Time-Scaled	H1-H8	0 - 730	1.125	c
2	Set 2 in Table 3	Full-Scale 1	H9	0 - 730	3.6	d
		Full-Scale 2	Central Heater H10	0 - 730	5.0	f
			Peripheral Heaters H11-H18	0 - 180	0	
				180 - 730	1.0	
		Time-Scaled	H1-H8	0 - 730	1.125	d, e
3	Set 2 in Table 3	Full-Scale 1	H9	Same as Series 2		d
		Full-Scale 2	Central Heater H10	0 - 376	5.0	d
				376 - 730	0	
			Peripheral Heaters H11-H18	0 - 204	0	
				204 - 244	1.0	
				244 - 376	0.85	
				376 - 730	0	
		Time-Scaled	H1-H8	0 - 730	1.125 decaying to 0.414	g, h

a Temperatures used as input for Thermomechanical Model Series 1 and 2 correspond to Thermal Model Series 1 and 2 reported by Chan, Cook, and Tsang, 1978.

b Predesign calculations, drifts not modeled.

c In this series only temperatures but not displacements and stresses have been calculated for the time-scaled experiment.

d Theoretical results from this model are currently stored in the MODCOMPIV computer at Stripa. Drifts have been modeled for the full-scale experiments.

e Time-scaled drift not modeled.

f Theoretical results from this model were stored in the MODCOMPIV computer at Stripa until mid-January 1979

g See Fig. 3.

h Time-scaled drift modeled. At this writing displacements and stresses have been calculated with this model only up to 180 days.

Accordingly, average granite thermal properties, which lead to higher temperatures (Thermal Model Series 1 in Chan et al, 1978) than in Stripa granite and the maximum values of α, ν and E measured in small specimens of Stripa granite* (Pratt et al., 1977) were used. These material properties are listed as Set 1 in Table 3.

Only the full-scale experiments were modeled in this series. The peripheral heaters were assumed to be turned on concurrently with the 5 kW central heater and to be operated at a constant power of 1 kW each throughout the entire duration of the experiment.

3.5.2. Model Series 2. Mean laboratory values for the thermal and mechanical properties of Stripa granite (Pratt et al., 1977), Set 2 in Table 3 were used. The heater powers are the same as in Series 1 except that the peripheral heaters are assumed to be energized 180 days later than the 5 kW central heater in Full-Scale Experiment 2. This decision to delay the turn-on of the peripheral heaters was reached mainly on the basis of the predicted temperatures and stresses of Model Series 1. The idea was to ensure that sufficient data would have been collected before part of the rock and some instruments were driven to a point where failure is highly probable. The Time-Scaled Experiment was also modeled, assuming each heater to be operated at a constant power of 1.125 kW, i.e., a scaled down physical model of a 3.6 kW full-scale heater. In this model, the time-scaled drift has not been taken into account. The predicted displacements and stresses from Model

---

[3] It should be noted that Pratt measured each material property in only one or two specimens. However, these were the only laboratory data available at the time the calculations commenced.

Table 3. Material properties for granite used in thermal and thermo-elastic calculations.

Property	Unit	Set 1[a]	Set 2[b]
Thermal conductivity	W/m°C	2.5	3.2
Density	kg/m^3	2600	2600
Specific heat	J/kg°C	798	837
Thermal diffusivity	m^2/s	1.078×10^{-6}	1.47×10^{-6}
Young's modulus	GPa	59.6	51.3
Poisson's ratio		0.27	0.23
Coefficient of linear thermal expansion	/°C	1.11×10^{-5}	1.11×10^{-5}

[a] Used in Model Series 1. Thermal properties are average granite properties. Elastic and thermoelastic properties are highest laboratory values for Stripa granite (Pratt et al., 1977).

[b] Used in Model Series 2 and 3. Mean laboratory values for Stripa granite (Pratt et al., 1977). All the results presented in the main text of the report were obtained using material properties tabulated as set 2 here.

Series 2 have been stored in the MODCOMPIV computer at Stripa until the middle of January 1979, when a firm decision was made on the power and turn-on time for the peripheral heaters.

3.5.3. Model Series 3. The same material properties are used as in Series 2. Full-Scale Experiment 1 is the same as before. In Full-Scale Experiment 2, peripheral heaters were assumed to be turned on 204 days[4] later than the central heater and maintained at a power of 1 kW each for 40 days, after which the power per peripheral heater is reduced to 0.85 kW. This particular power scheme has been chosen so that the ambient rock temperature within a radius of approximately 1 m from the central heater axis is raised more or less uniformly by 100°C by the peripheral heaters in about 35 days but does not deviate appreciably from that level throughout the remaining heating period, as illustrated in Fig. 6. In addition, the cooling period has also been modeled assuming tentatively that all heaters are turned off 376 days[5] after start-up of the central heater. Predicted temperatures, displacements, and stresses for Full-scale Experiment 2 from Model Series 3 is the current version stored in the MODCOMPIV computer at Stripa. Incidentally, the thermal modeling of the cool-down period has been checked against field data from the Luleå University Pilot Heater Experiment (Chan, Carlsson, and Jeffry, 1979).

For the time-scaled experiment, a decaying power, as shown in Fig. 3,

---

[4] As a matter of fact, the peripheral heaters have been energized on January 23, 1979 at 9:00 a.m., Greenwich Mean Time, exactly as planned.

[5] The turn-off time for this experiment has now been revised slightly and the calculations are being updated.

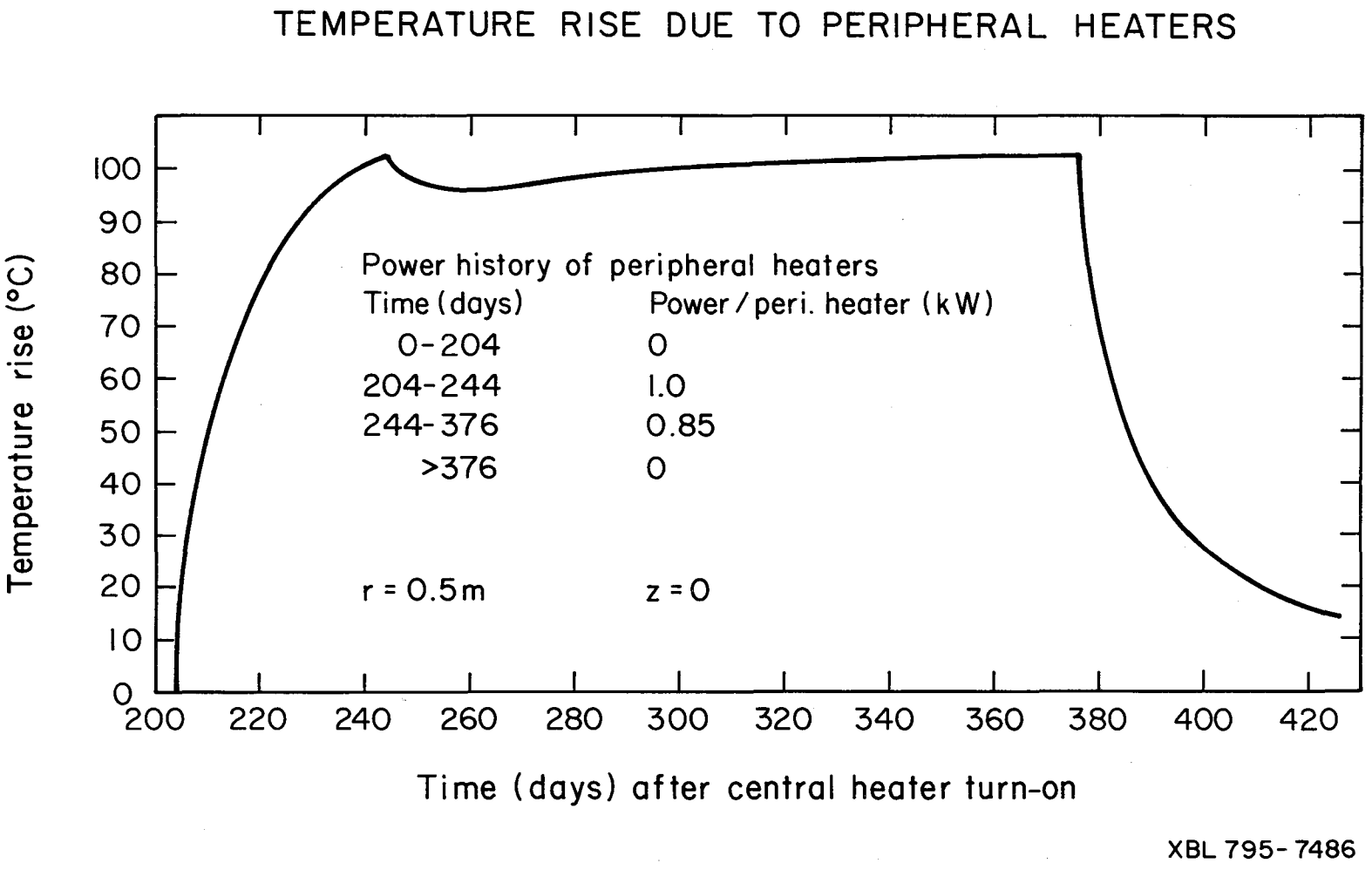

Fig. 6. Temperature rise in rock caused by the peripheral heaters in Full-Scale Experiment 2 at a point ($r = 0.5$ m, $z = 0$, $\theta = 0$ deg) in the midplane of the heater array.

was used to simulate the thermal output of a 5-year-old reprocessed PWR high-level waste canister. For the period of approximately 20 years of real time represented by this scaled-down experiment, the normalized thermal power curve for unreprocessed spent fuel will be essentially the same as that used in the present calculations, although the size of the waste canister and the actual power would be quite different. Details of predicted temperatures will be published in a separate report.

In Model Series 3 the presence of the time-scaled drift has been taken into account in the thermoelastic model for the time-scaled experiment. At this writing the thermomechanical calculations for this experiment have been carried out to day 180. In view of the enormous amount of computational efforts involved, it was decided to wait until the turn-off date has been finalized for this experiment before completing the entire time sequence of calculations and transferring the predicted results to Stripa. Currently, therefore, the predicted temperatures for the time-scaled experiment from Model Series 3 and the displacements and stresses from Model Series 2 are stored in the MODCOMPIV.

4. RESULTS AND DISCUSSIONS

Unless otherwise stated, the results presented here pertain to Model Series 3, in which the powers assumed for the heaters correspond to the actual operating conditions, except for the turn-off time.

4.1. Full-scale experiments

4.1.1. Displacements. Thermally induced radial displacements in the midplane of Full-Scale Experiment 1 (H9, 3.6 kW) calculated using two different finite element models (M1, drifts not modeled, and M7, drifts modeled) are plotted against radial distance in Fig. 7a and 7b for various elapsed time (days) since this heater was turned on.[6] In these figures, radial displacement away from the central heater is taken as positive. Vertical lines labeled A, B, C, D, mark the locations of anchor points on the horizontal extensometer E19 that runs normal to the extensometer drift at the level of the heater midplane.

It can be seen that in the first few months the radial displacement exhibits a well-defined peak at a radial distance of approximately 1 m from the axis of the central heater. This peak broadens and moves away from the central heater with increased time. Comparison of Fig. 7a and 7b shows that the presence of the extensometer drift 10 m from the central heater has only minor effects until about 150 days. Thereafter, the free surface at the wall of the drift significantly influences the radial dispacements at locations more than 3.5 m from the central heater. Radial displacements within that 3.5 m radius are affected to a much lesser extent. Thus relative horizontal displacements between extensometer anchor points at radial distances less than 3.5 m would not be strongly influenced by the extensometer drift while relative displacements between anchor points and the collar of the extensometer hole (at the wall of the extensometer drift) would be.

In Full-Scale Experiment 1 (3.6 kW), radial displacements within a radial distance of 3.5 m from the central heater change very little between

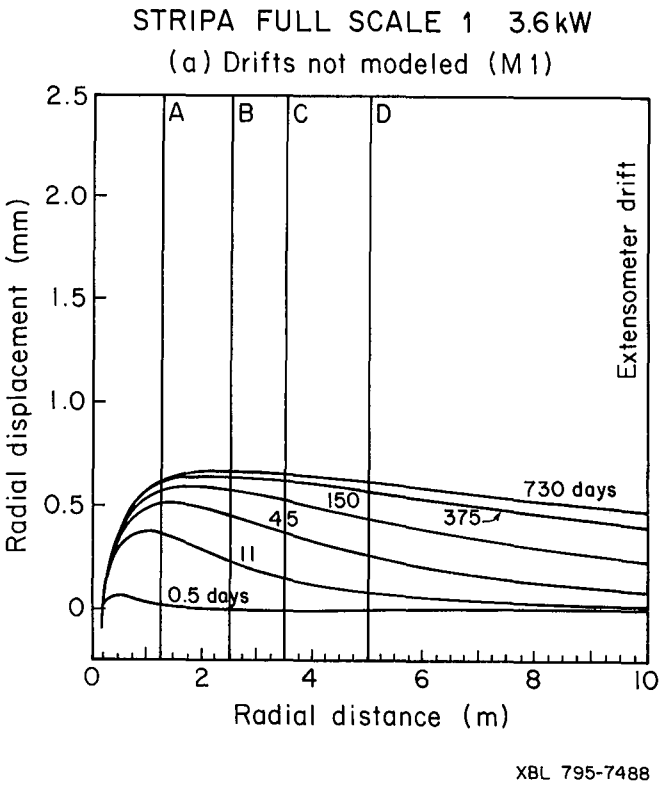

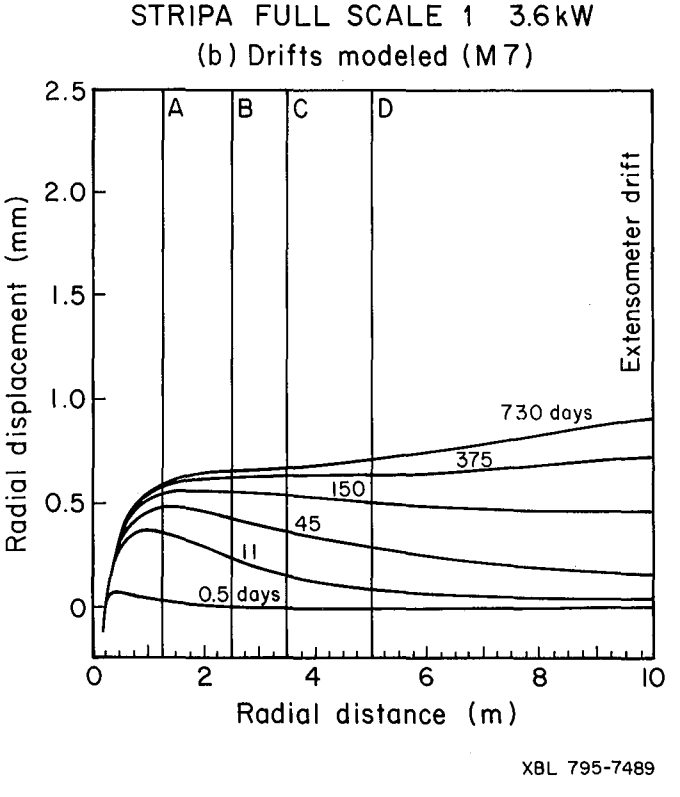

Fig. 7. Thermally induced radial displacement as a function of the radial distance at various times along the midplane of the 3.6 kW full-scale heater. Positive displacement is away from the axis of the heater.

150 and 730 days. The maximum value is predicted to be approximately 0.6 mm, whether the extensometer drift is taken into account or not. As the radial displacement curves are all quite flat beyond a radial distance of 1 m, except for the first month or so, the maximum relative displacement between any pair of adjacent anchor points on E19 is only about 0.1 mm. Maximum relative displacement between the anchor point D at 5 m radius and the wall of the extensometer drift is approximately 0.2 mm.

It should be noted that since the extensometer drift has been approximated as a torus in Mesh 7, the predicted effect of this drift may tend to be exaggerated. This exaggeration is likely to be more severe for horizontal extensometers inclined at an angle to the drift than for horizontal extensometers perpendicular to the axis of the drift.

Figure 8 depicts the radial displacement profiles for the second Full-Scale Experiment. Again the vertical lines A, B, C, D, represent the locations of the anchor points on the horizontal extensometer E28 at the level of the heater midplane. Before the peripheral heaters are turned on, the radial displacements for the two full-scale experiments are directly proportional to the heater powers, 3.6 kW and 5 kW, respectively. The temperature distribution due to the peripheral heaters (turned on 204 days after the central heater) sharpens the peak in the radial displacement profile for a short period after they have been energized (see curves labeled 207 days in Fig. 8a and 8b) so that a significant increase is expected in the relative displacement between anchor points. At longer time, as the peripheral heaters raise the temperature of a larger volume of rock, substantially larger radial displacements and stronger influences of the extensometer drift than in the

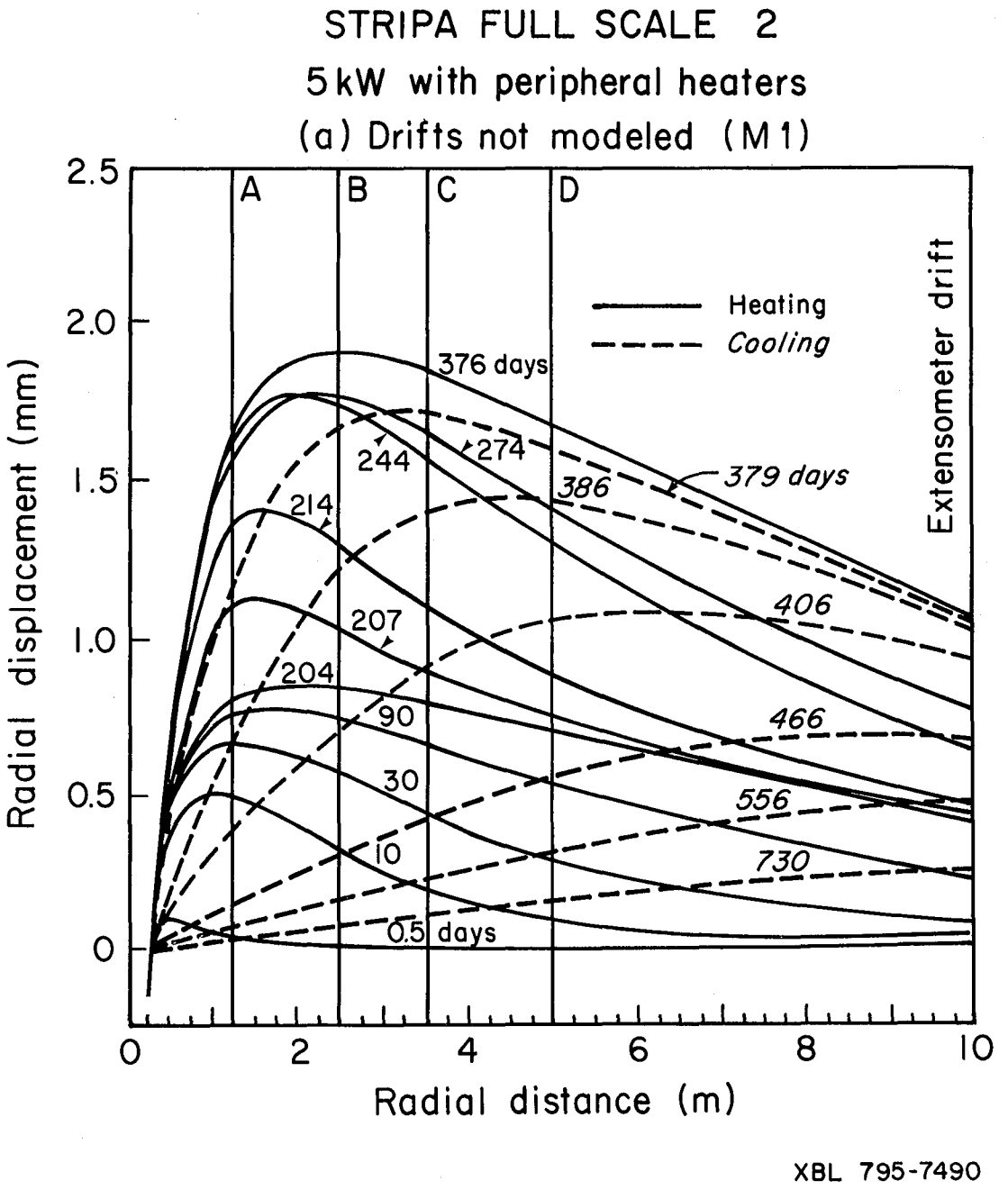

Fig. 8a. Thermally induced radial displacement at various times as a function of radial distance along the midplane of Full-Scale Experiment 2 (5 kW with peripheral heaters). Drifts not modeled. Positive displacement is away from the axis of the central heater.

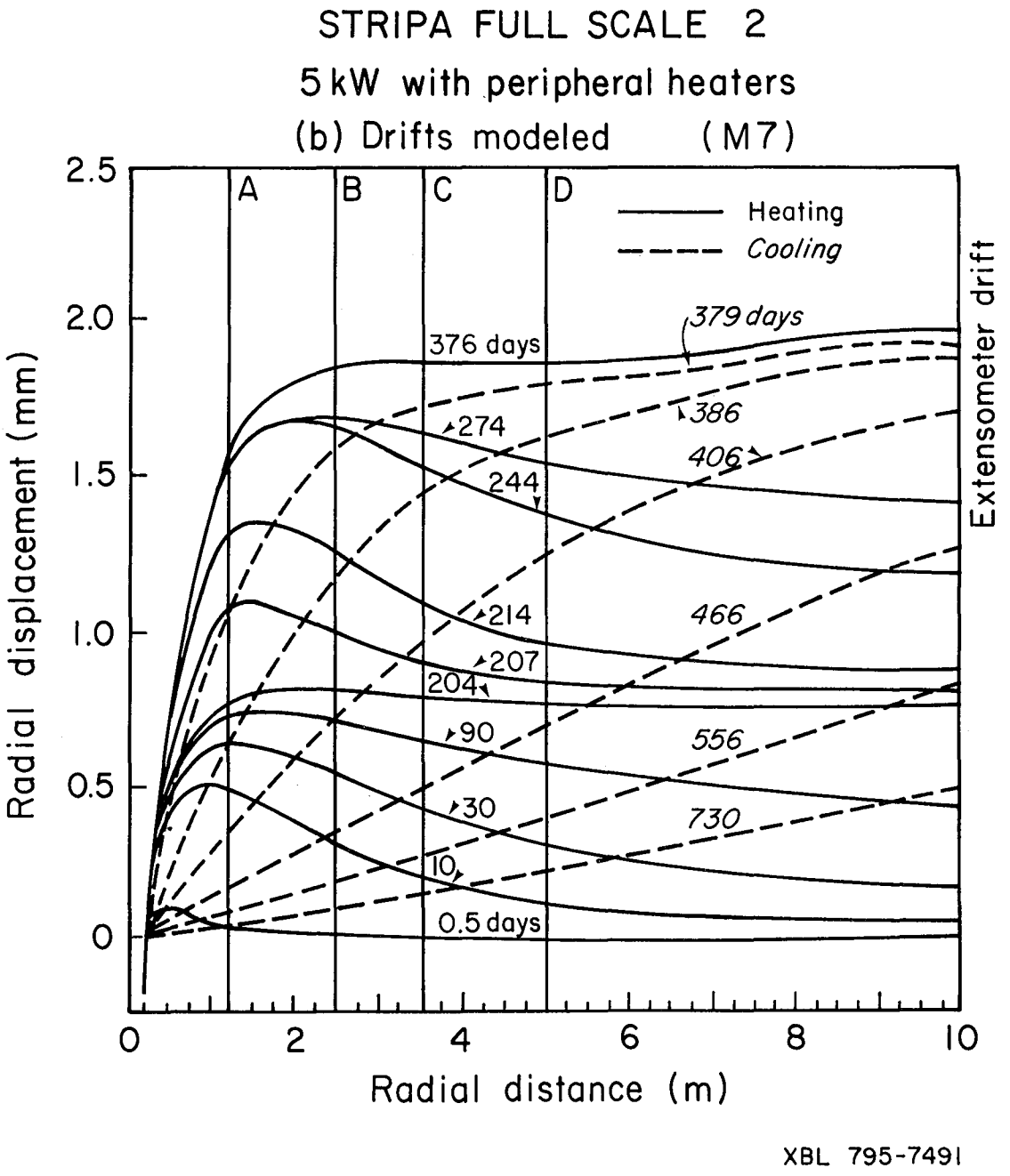

Fig. 8b. Thermally induced radial displacement at various times as a function of radial distance along the midplane of Full-Scale Experiment 2 (5 kW with peripheral heaters). Drifts modeled. Positive displacement is away from the axis of the central heater.

first experiment are expected. The peripheral heaters also cause the peak radial displacement to occur at a greater radial distance, cf. Fig. 7 and Fig. 8. Before the peripheral heaters are turned on, maximum theoretical radial displacement within a 4 m radius of the central heater has been found to be about 0.8 mm (204 days), regardless of whether the drift is modeled or not. After the peripheral heaters have been turned on, the theoretical peak value reaches about 1.9 mm, 376 days after the start of this experiment.

As soon as the heaters are shut off (after 376 days as assumed in the present calculations), the radial distribution of the radial displacement begins to change dramatically. Since there is a greater temperature drop close to the central heater, there is a correspondingly greater thermal contraction. Consequently, the peak of the radial displacement curve moves further outward so that some of the anchor points on the horizontal extensometer E28 now lie on the steep portion of the curve. Maximum relative horizontal displacement between adjacent anchor points on horizontal extensometer E28 and between anchor point D (r = 5 m) and the wall of the extensometer drift are summarized in Table 4.

Departure from linear elastic deformation behavior is very likely during the cool-down period. Both hysteresis and permanent set may occur. Again, comparison between the results of linear thermoelastic theory and field observations would reveal both the nature and degree of the departure of *in situ* rock behavior from the idealized situation.

To display both the magnitude and direction of the thermally induced displacement field, displacement vector maps have been plotted in the longi-

Table 4. Maximum predicted relative horizontal displacements between adjacent anchor points or between the wall of the extensometer drift and anchor point D (r = 5 m) on a horizontal extensometer (E28) at the level of the midplane of Full-scale Experiment 2 (5 kW with peripheral heaters).

Phase	Time (days)	Maximum relative displacement (mm) between adjacent anchor points		between D and wall of extensometer drift	
		(a)	(b)	(a)	(b)
1	0-204	0.17	0.21	0.30	0.14
2	204-376	0.28	-0.26	0.66	0.18
3	376-730	-0.51	-0.54	0.54	-0.56

Notes: (1) Phase 1 = only 5 kW central heater on;
Phase 2 = both central heater and peripheral heaters on;
Phase 3 = all heaters off.
(2) Positive relative displacement means compression;
negative relative displacement means expansion.
The displacements in this table are those with the largest magnitudes.
(3) Case (a) = drifts not modeled (M1);
Case (b) = drifts modeled (M7).

tudinal plane of the heater(s). Typical examples are given in Figs. 9 and 10 for the two full-scale experiments. In these figures, displacements above the heater midplane (z = 0) are the results of model M7 (i.e., with drifts taken into account), while displacement below the midplane are from model M1, which ignored the presence of the drifts. Displacement vector maps for Full-Scale Experiment 2 before the turn-on of the peripheral heaters are not illustrated, since the required displacements can be scaled from those plots given for the 3.6 kW experiment. Note that because of the large difference in the magnitudes of the displacements, it is necessary to represent the displacement vector on different scales for the two experiments. In each frame the top and bottom portions (above and below the heater midplane z = 0) represent the theoretical displacement fields from the model appropriate to that portion of space, i.e., Model M7 (drifts modeled) and Model M1 (drifts not modeled), respectively[7]. The left edge of each frame is an axis of symmetry. It is of interest to note that (1) the radius of the central heater hole decreases by approximately 1 mm and 2 mm, respectively, in the two experiments, as a consequence of the confinement imposed on the hot rock by the colder rock outside and (2) due to the cumulative nature of displacement and the proximity of the heater drift to the heaters, this drift has a significant effect on the vertical displacement even shortly after, (e.g., 30 days) the central heater has been turned on, as can be seen by comparing the displacements at z = 4.25 m and z = -4.25 m in Fig. 9. Maximum vertical displacements of 1.4 mm and 4.0 mm have been predicted to occur at the floor of the heater drift above the 3.6 kW and the 5 kW heaters, respectively.

---

[7]This combination of the two models has been made for all the predicted values in all plots comparing predicted and measured quantities.

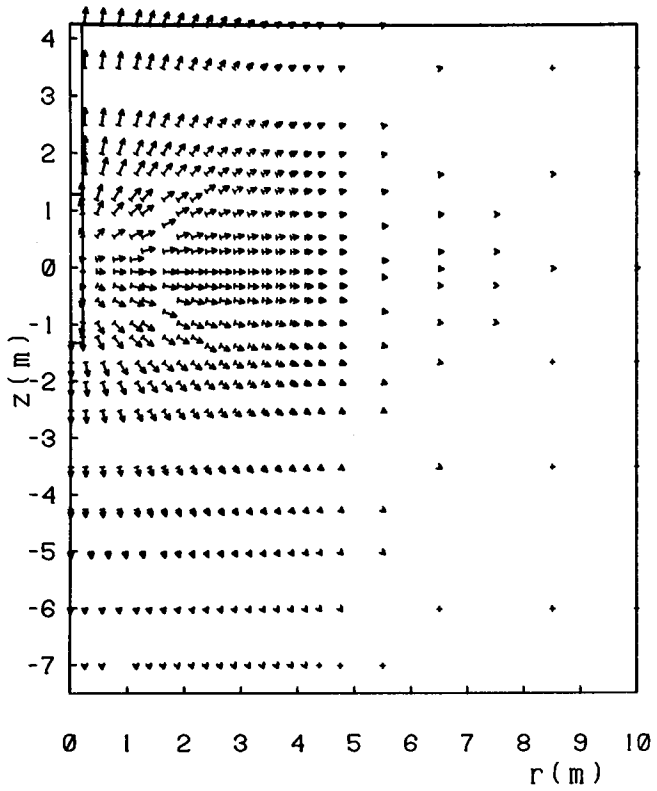

VECTOR PLOT OF DISPLACEMENT

STRIPA FULL SCALE 1 - ONE HEATER 3.6KW
time = 30.000 θ = 0.000 °
Displacement exaggerated 500. times
Values less than .940E-04 are plotted as crosses (+)

model: COMBINED SSET3 calculated 04/22/78, plotted 09/21/78 20.15.15 VECP004

XBL 7811-12223

Fig. 9a. Vector plot of thermally induced displacements in the longitudinal plane of the 3.6 kW heater after 30 days.

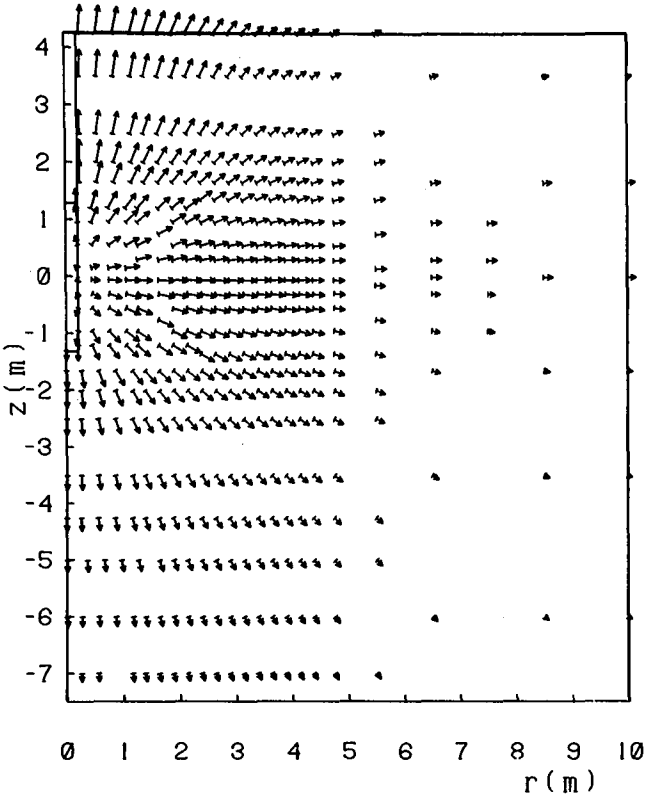

VECTOR PLOT OF DISPLACEMENT

STRIPA FULL SCALE I - ONE HEATER 3.6KW
time = 90.000 θ = 0.000 °
Displacement exaggerated 500. times
Values less than .940E-04 are plotted as crosses (+)

model: COMBINED SSET3 calculated 04/22/78, plotted 09/21/78 20.15.17 VECP004

XBL 7811-12233

Fig. 9b. Vector plot of thermally induced displacements in the longitudinal plane of the 3.6 kW heater after 90 days.

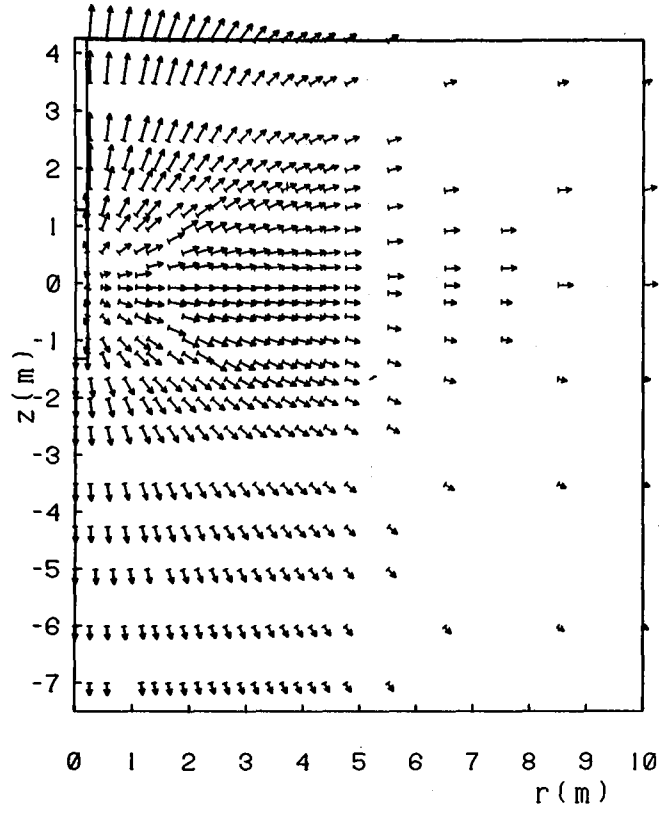

VECTOR PLOT OF DISPLACEMENT

STRIPA FULL SCALE I - ONE HEATER 3.6KW
time = 180.000 θ = 0.000 °
Displacement exaggerated 500. times
Values less than .940E-04 are plotted as crosses (+)

model: COMBINED SSET3 calculated 04/22/78, plotted 09/21/78 20.15.18 VECP004

XBL 7811-12227

Fig. 9c. Vector plot of thermally induced displacements in the longitudinal plane of the 3.6 kW heater after 180 days.

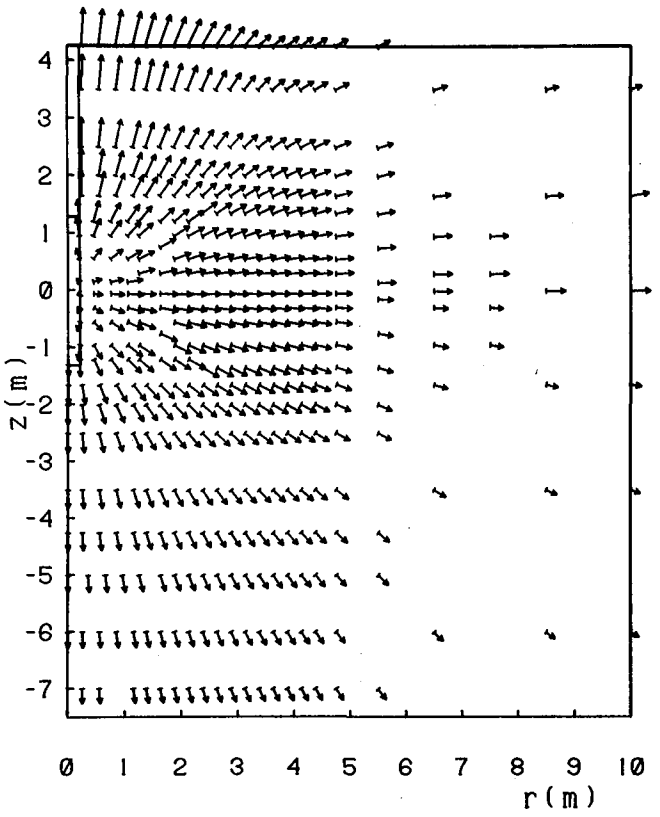

VECTOR PLOT OF DISPLACEMENT

STRIPA FULL SCALE 1 - ONE HEATER 3.6KW
time = 360.000 θ = 0.000 °
Displacement exaggerated 500. times
Values less than .940E-04 are plotted as crosses (+)

model: COMBINED SSET3 calculated 04/22/78, plotted 09/21/78 20.15.20 VECP004

XBL 7811-12225

Fig. 9d. Vector plot of thermally induced displacements in the longitudinal plane of the 3.6 kW heater after 360 days.

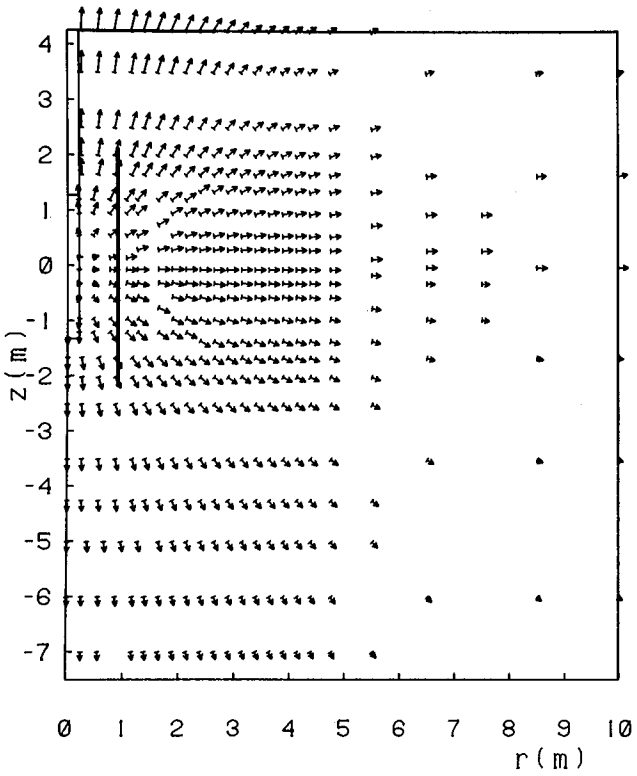

VECTOR PLOT OF DISPLACEMENT

STRIPA FULL SCALE 2 - 5KW CENTRAL HEATER + PERIPHERALS
time = 204.000 θ = 0.000 °
Displacement exaggerated 250. times
Values less than .188E-03 are plotted as crosses (+)

model: COMBINED SSET3 calculated 01/09/79, plotted 05/07/79 13.05.50 VECP001

XBL 795-9900

Fig. 10a. Vector plot of thermally induced displacements in the longitudinal plane of the 5 kW heater after 204 days.

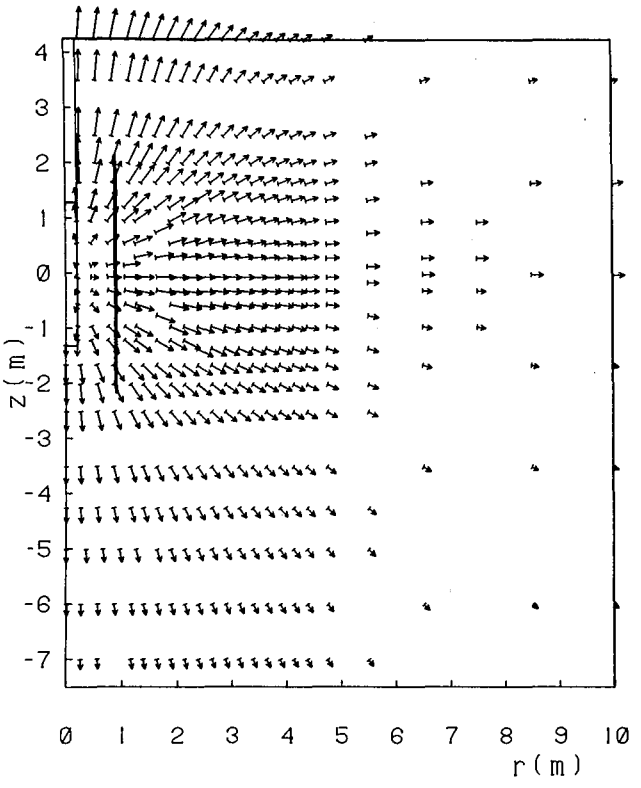

VECTOR PLOT OF DISPLACEMENT

STRIPA FULL SCALE 2 - 5KW CENTRAL HEATER + PERIPHERALS
time = 214.000 θ = 0.000 °
Displacement exaggerated 250. times
Values less than .188E-03 are plotted as crosses (+)

model: COMBINED SSET3 calculated 01/09/79, plotted 05/07/79 13.05.52 VECP001

XBL 796-9933

Fig. 10b. Vector plot of thermally induced displacements in the longitudinal plane of the 5 kW heater after 214 days.

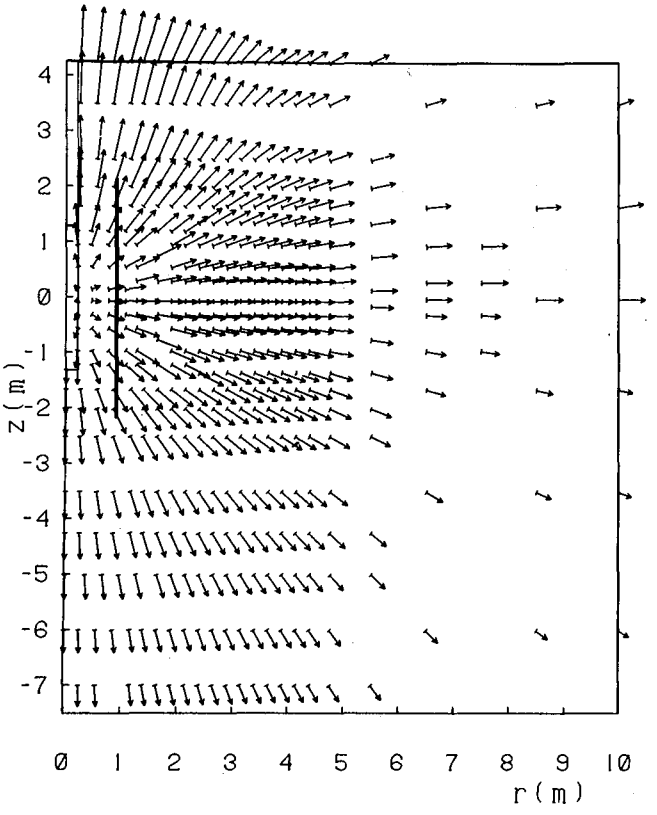

VECTOR PLOT OF DISPLACEMENT

STRIPA FULL SCALE 2 - 5KW CENTRAL HEATER + PERIPHERALS
time = 376.000 θ = 0.000 °
Displacement exaggerated 250. times
Values less than .188E-03 are plotted as crosses (+)

model: COMBINED SSET3 calculated 01/09/79, plotted 05/07/79 13.05.56 VECP001

XBL 796-9935

Fig. 10c. Vector plot of thermally induced displacements in the longitudinal plane of the 5 kW heater after 376 days.

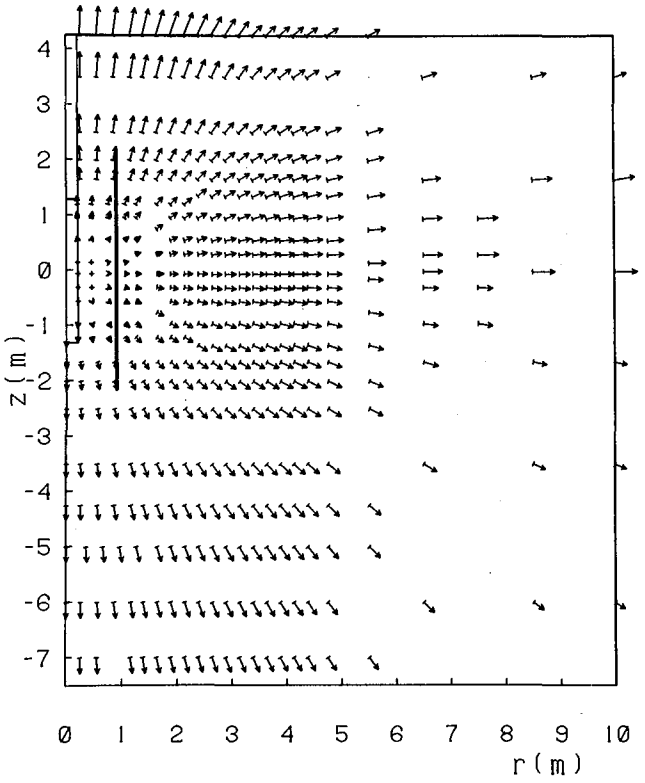

VECTOR PLOT OF DISPLACEMENT

STRIPA FULL SCALE 2 - 5KW CENTRAL HEATER + PERIPHERALS
time = 406.000 θ = 0.000 °
Displacement exaggerated 250. times
Values less than .188E-03 are plotted as crosses (+)

Mesh: COMBINED SSET3 calculated 01/09/79, plotted 05/07/79 13.05.59 VECP001

XBL 796-9941

Fig. 10d. Vector plot of thermally induced displacements in the longitudinal plane of the 5 kW heater after 406 days.

Vertical displacements are typically twice or more as large as horizontal (radial) displacements, partly because of the elongated shape of the heated zone (Chan, Cook, and Tsang, 1978) and partly because the heater drift is much closer to the heater than the extensometer drift. From Fig. 10 it can be seen that movements of the floor of the heater drift (approximately 4 mm) and the side wall of the extensometer drift (approximatelly 1 mm) are not negligible.

By taking differences between calculated displacements for appropriate pairs of spatial points, relative displacements are obtained for comparison with extensometer readings. Typical examples are shown in Figs. 11-18 for relative displacements in the two full-scale experiments plotted against time. These include predicted (dotted) and measured (solid) displacements at different anchor points of a vertical or horizontal extensometer relative to the collar of the extensometer hole as well as predicted and measured displacements between a pair of anchor points of a vertical or horizontal extensometers for the two experiments. Coordinates of individual anchor points are given in the caption of each figure. For details of instrument location, refer to the report by Schrauf et al. (1979, in preparation). Complete sets of these plots have been generated using either the CDC-7600 computer at LBL or the MODCOMPIV computer at Stripa.

Differences in the anchor point coordinates given on the plots for "theory" and "experiment" are due to one or both of the following reasons: (1) the model assumes axial symmetry whereas the actual geometry is three-dimensional; and (2) the computer file containing the coordinates of the "experimental" anchor points did not take into account the slope of the "horizontal" holes (a defect that has now been corrected) whereas this slope

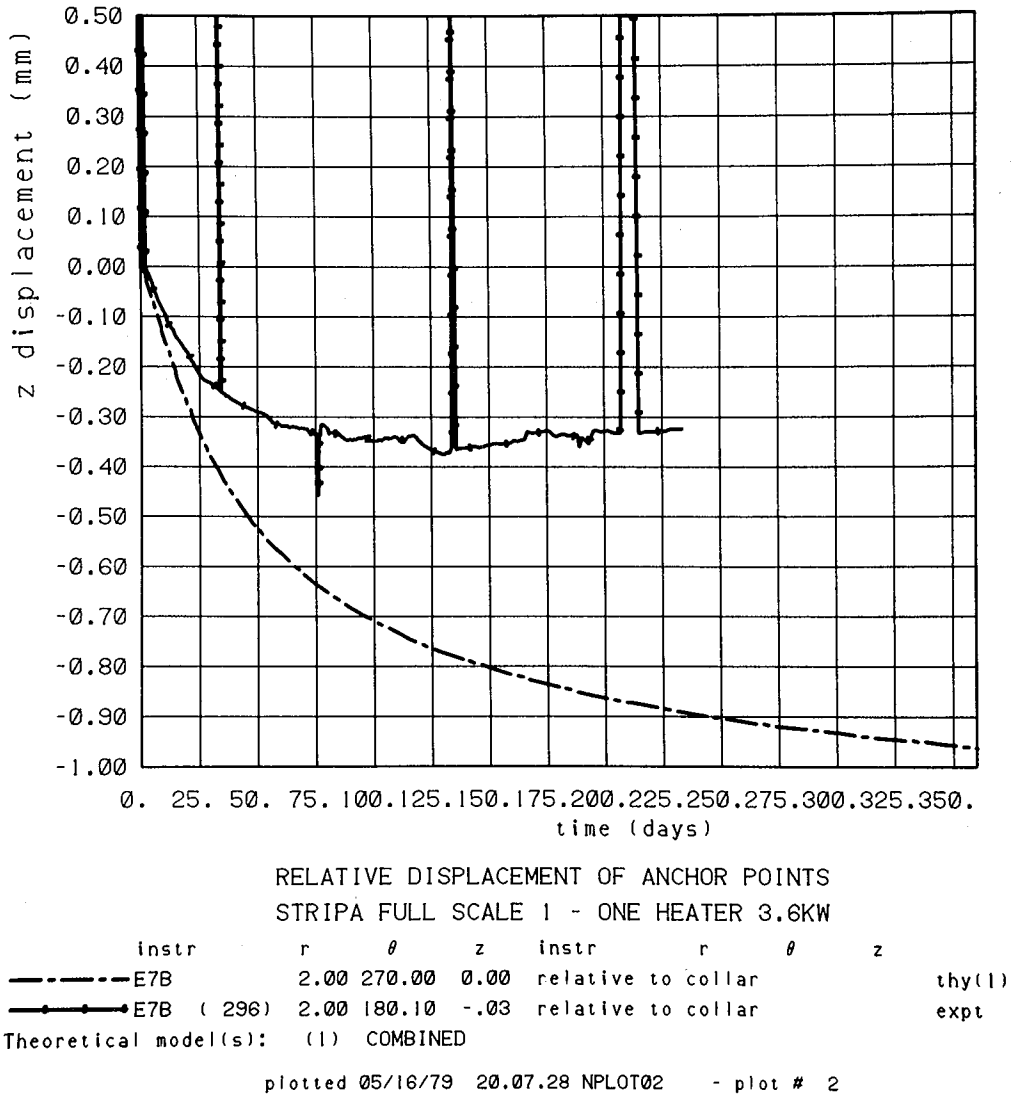

XBL 795-9909

Fig. 11a. Typical plot of predicted and measured displacement vs. time at different anchor points of a vertical extensometer in Full-Scale Experiment 1 (3.6 kW) relative to the collar of the extensometer hole. The cylindrical coordinates (see Fig. 4a) for the anchor point illustrated are r = 2 m, z = 0. The collar is at r = 2 m, z = 4.25 m.

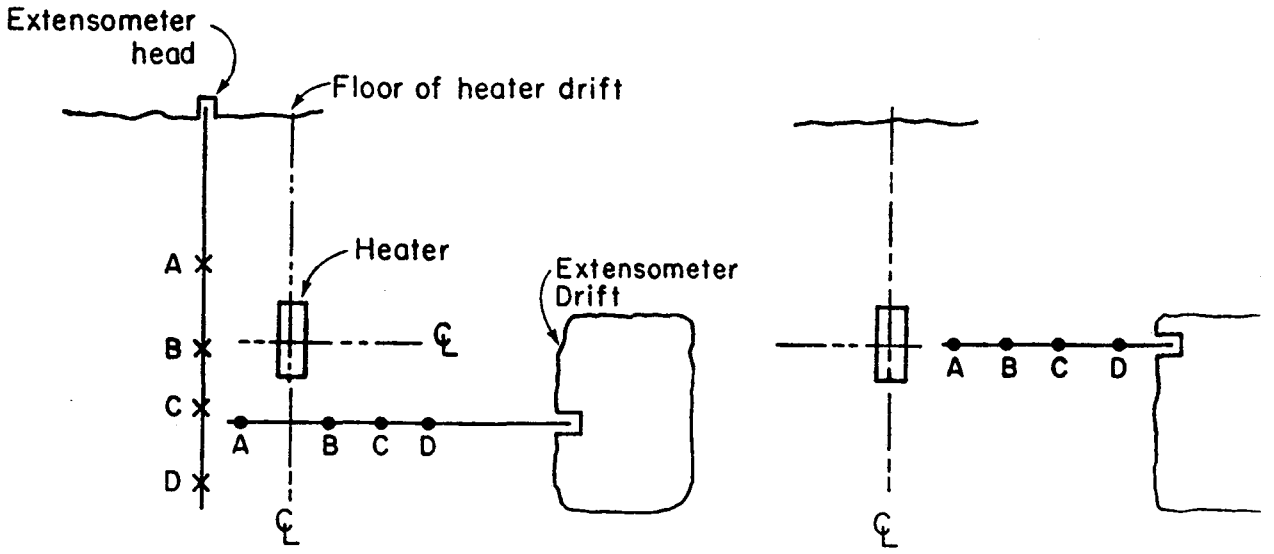

Case I
Anchors cross a heater midplane

Case II
Anchors do not cross a heater midplane

• Anchor points in horizontal hole
× Anchor points in vertical hole

XBL 798-1141

Fig. 11b. Extensometer anchor point designation.

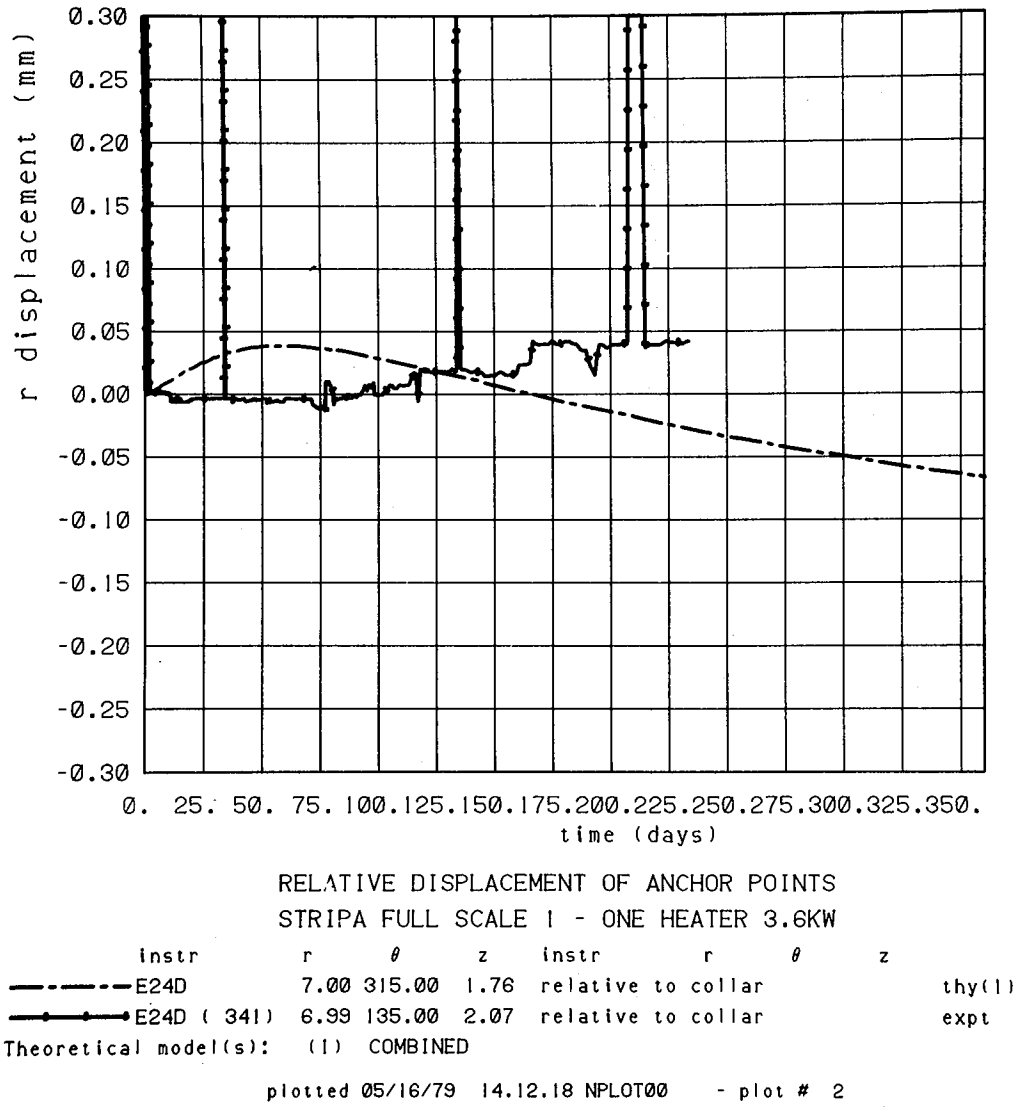

Fig. 12. Typical plot of predicted and measured displacement vs. time at an anchor point of a horizontal extensometer in Full-Scale Experiment 1 (3.6 kW) relative to the collar of the extensometer hole. The anchor point illustrated has cylindrical coordinates r = 7 m, z = 1.76 m. The collar is at r = 14 m but taken as r = 10 m in the model because of assumption of axisymmetry.

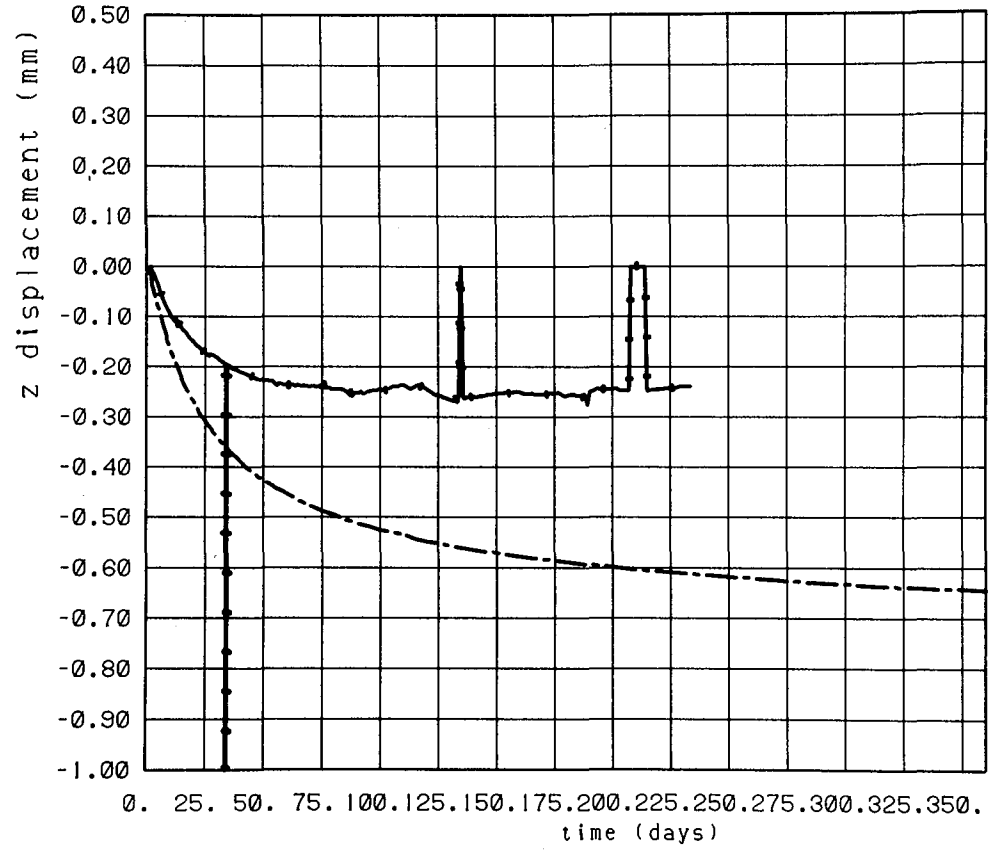

XBL 795-9911

Fig. 13. Typical plot of predicted and measured relative displacement between two anchor points of a vertical extensometer in Full-scale Experiment 1 (3.6 kW). The two anchor points are at r = 2 m and z = 0 and 2.25 m, respectively, in the cylindrical coordinate system illustrated in Fig. 4a.

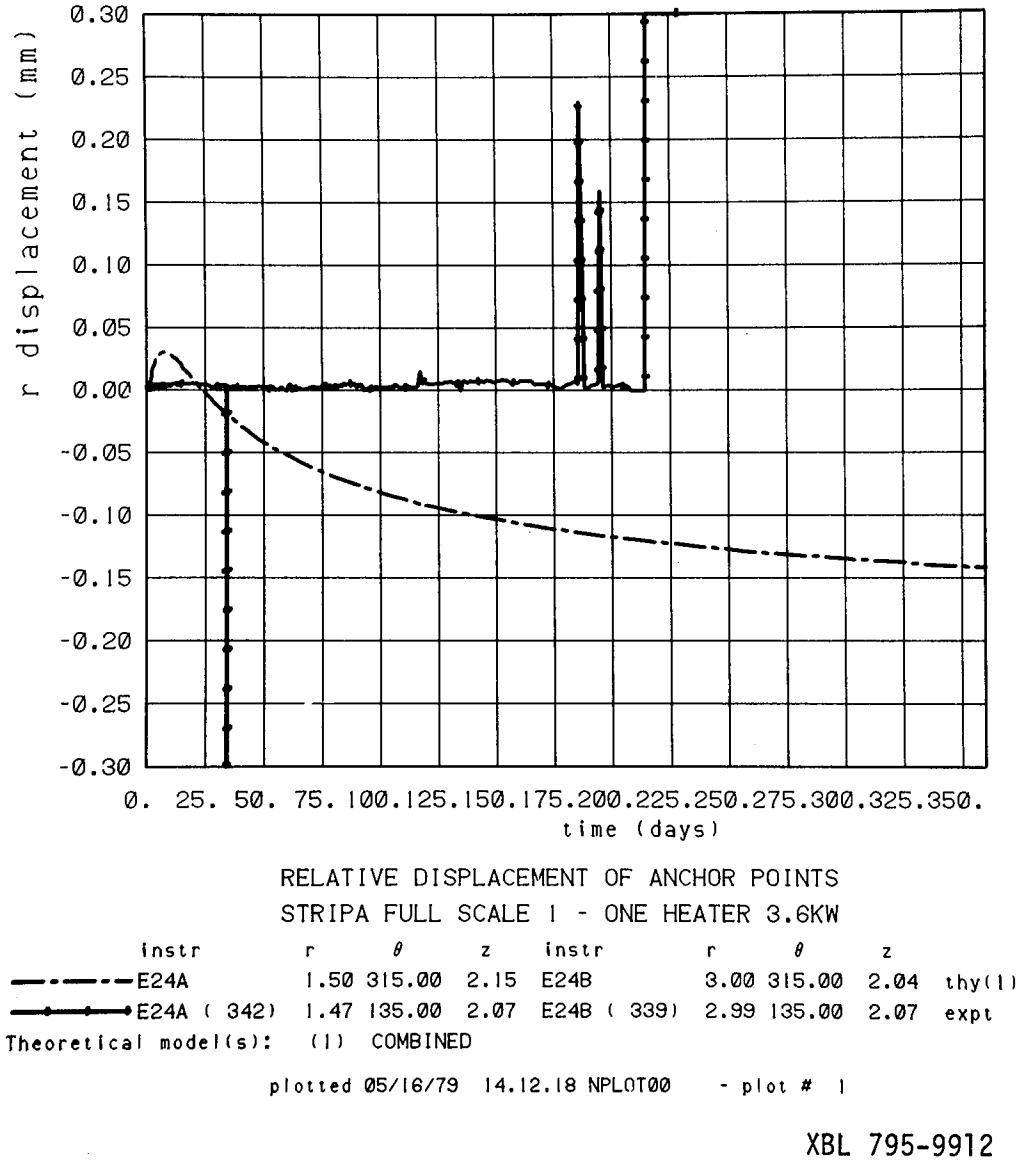

XBL 795-9912

Fig. 14. Typical plot of predicted and measured relative displacement between two anchor points of a horizontal extensometer vs. time in Full-scale Experiment 1 (3.6 kW). The two anchor points are at r = 1.5 m, z = 2.15 m and r = 3 m, z = 2.04 m, respectively, in the cylindrical coordinate system illustrated in Fig. 4a.

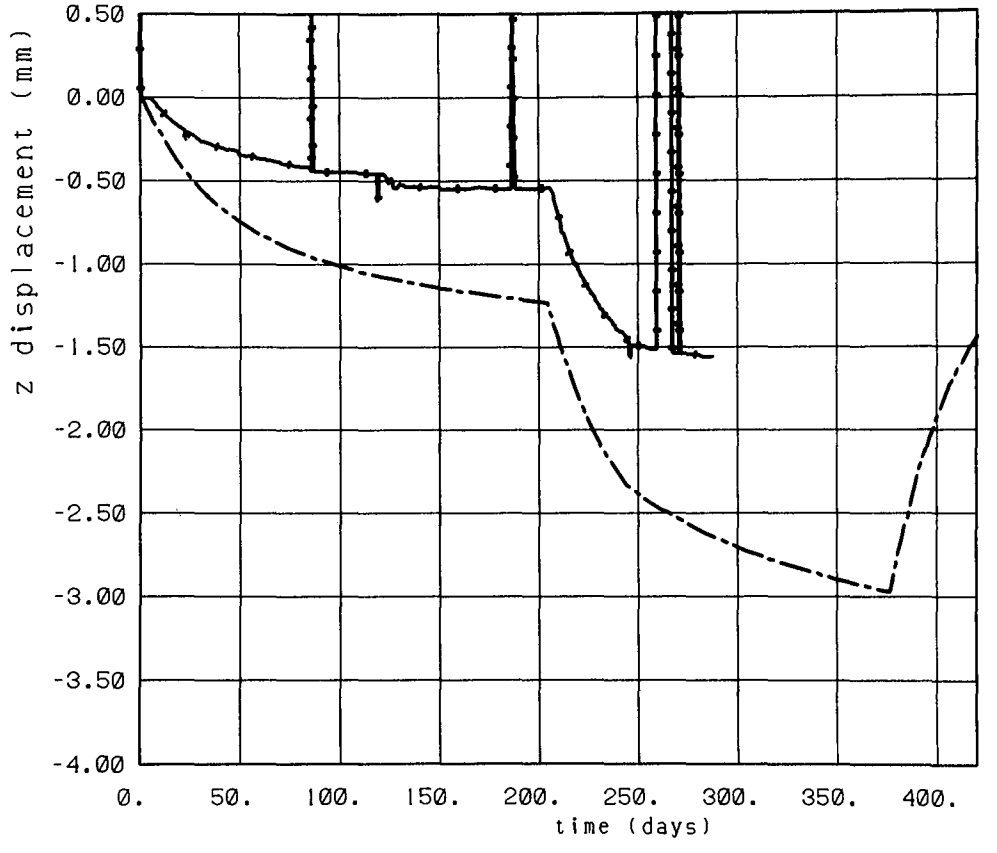

XBL 795-9913

Fig. 15. Typical plot of predicted and measured displacement vs. time at an anchor point of a vertical extensometer in Full-Scale Experiment 2 (5 kW with peripheral heaters) relative to the collar of the extensometer hole. The anchor point is at r = 1.99 m, z = -0.07 m, and the collar is at 4 = 1.99 m and z = 4.25 m in the cylindrical coordinate system illustrated in Fig. 4a.

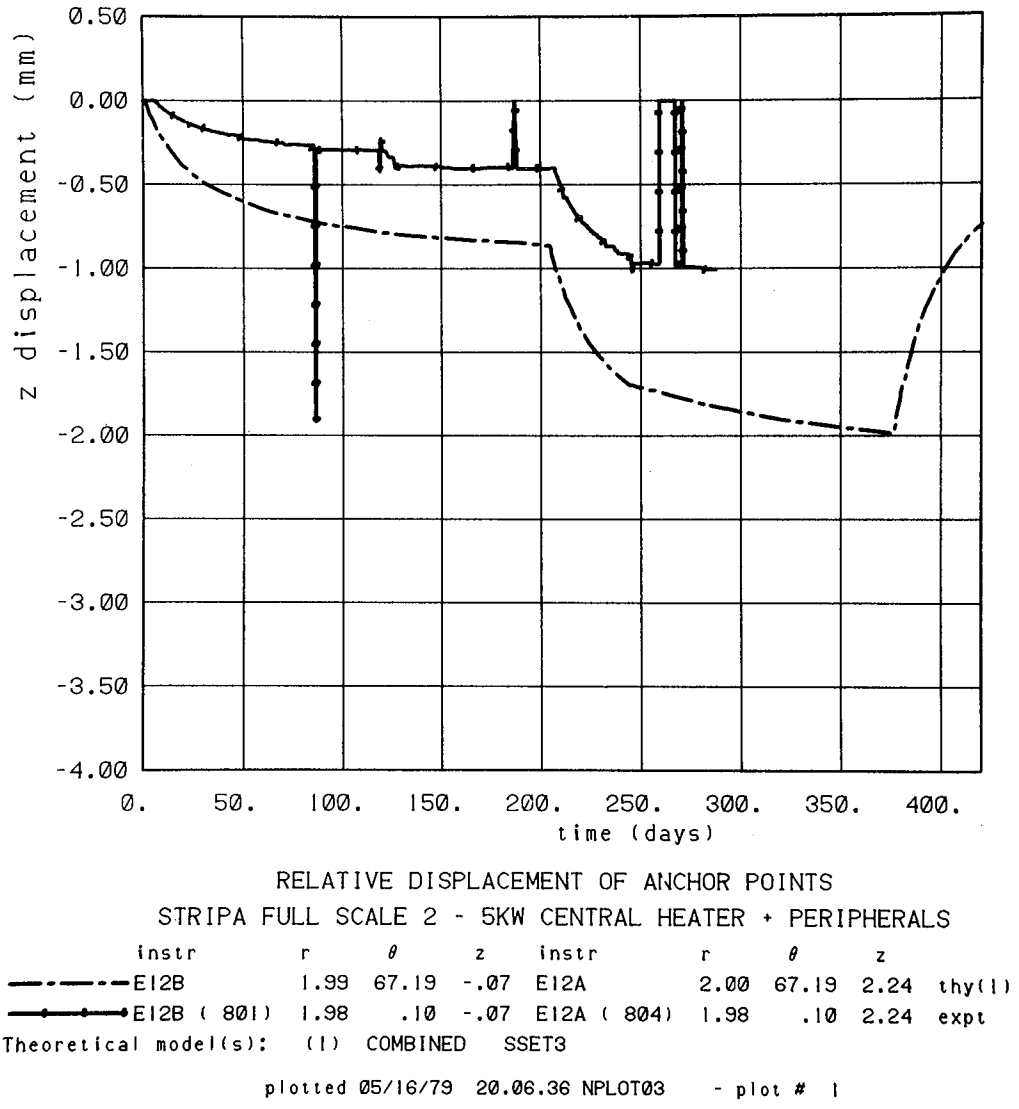

XBL 795-9914

Fig. 16. Typical plot of predicted and measured relative displacement between two anchor points of a vertical extensometer vs. time in Full-scale Experiment 2 (5 kW with peripheral heaters). The two anchor points are at r = 1.99 m, z = -0.07 m and r = 2 m, z = 2.24 m, respectively, in the cylindrical coordinate system illustrated in Fig. 4a.

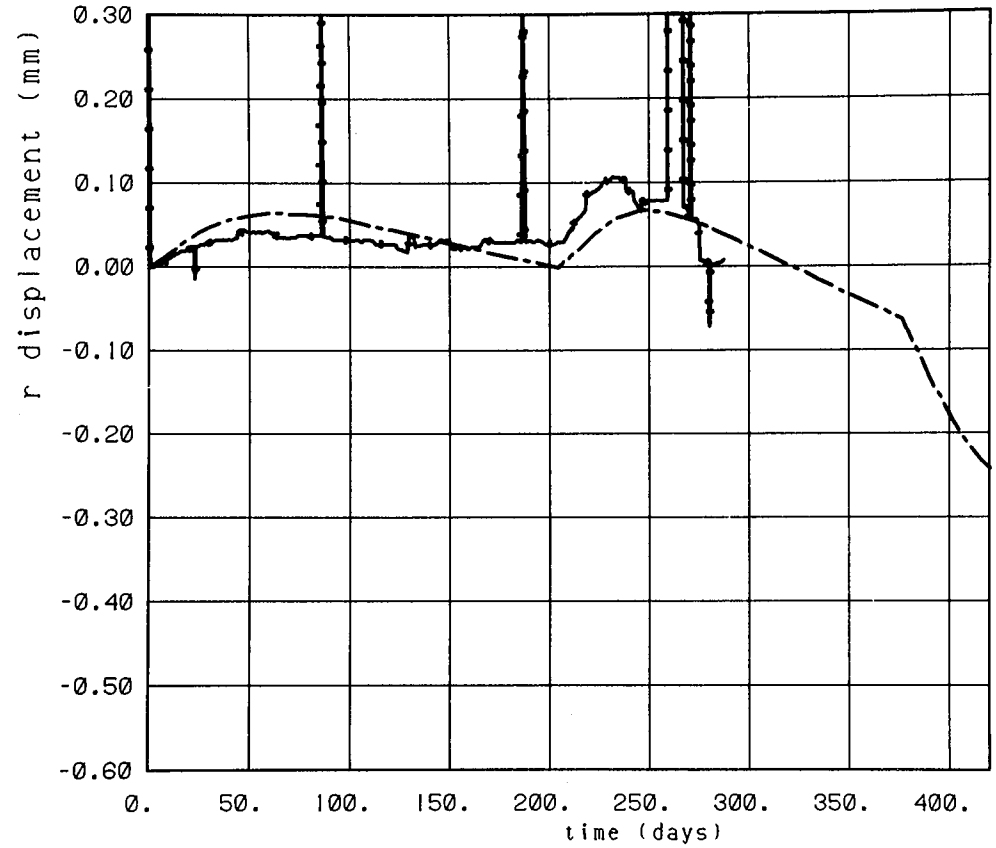

XBL 795-9908

Fig. 17. Typical plot of predicted and measured displacement vs. time at an anchor point of a horizontal extensometer in Full-Scale Experiment 2 (5 kW with peripheral heaters) relative to the collar of the extensometer hole. The anchor point is at r = 6.97 m, z = 1.41 m and the collar is at 4 = 10 m, z = 1.10 m, in the cylindrical coordinate system illustrated in Fig. 4a.

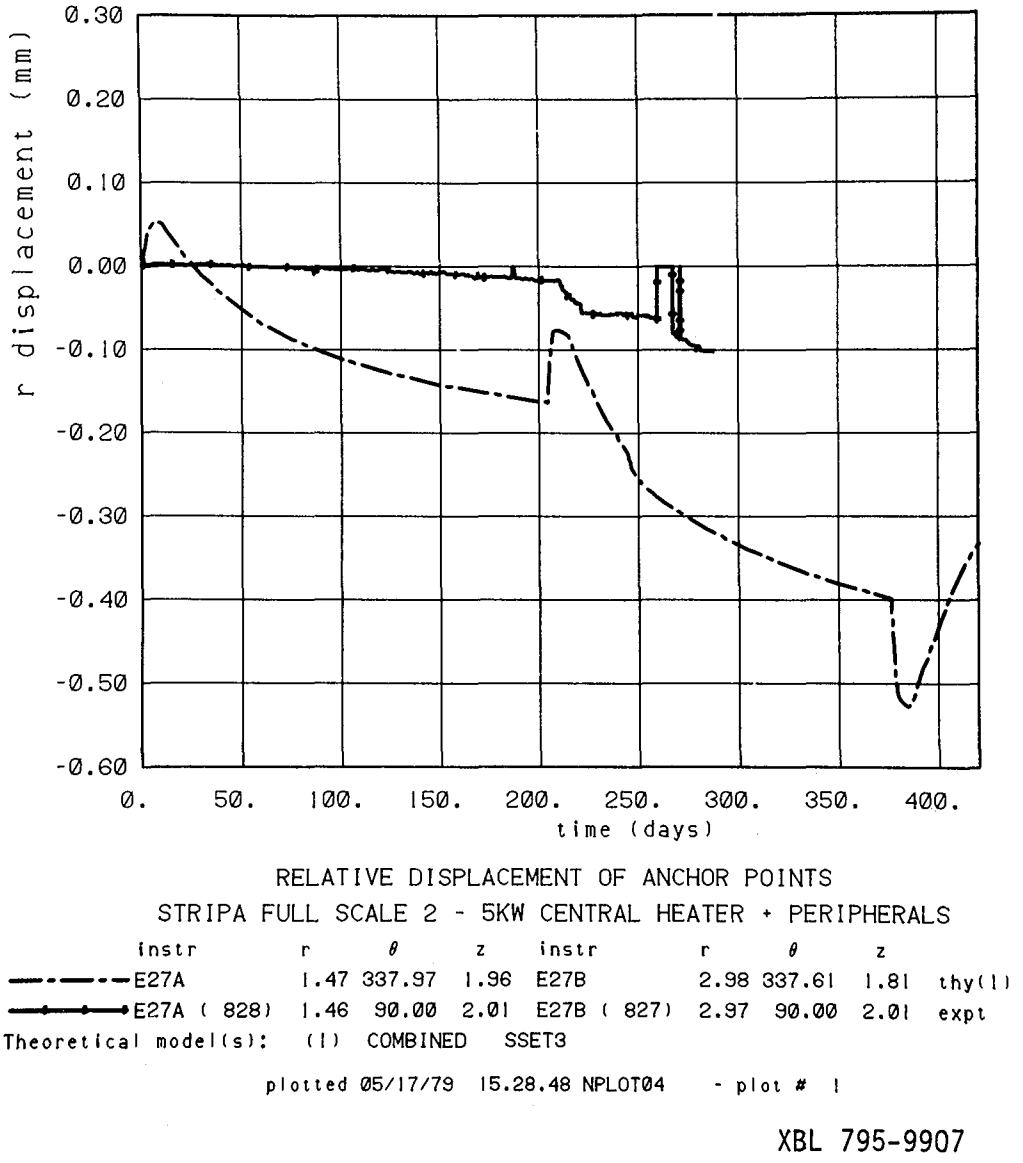

XBL 795-9907

Fig. 18. Typical plot of predicted and measured relative displacement between two anchor points of a horizontal extensometer vs. time in Full-scale Experiment 2 (5 kW with peripheral heaters). The two anchor points are at r = 1.47 m, z = 1.96 m and r = 2.98 m, z = 1.81 m, respectively, in the cylindrical coordinate system illustrated in Fig. 4a.

has been taken into consideration in calculating the displacements at the specified anchor points. The difference in the values given for the angle 0° is due to the different sign conventions and reference axes for the model and for the field system. This, however, does not affect the results since there is no angular dependence in the axisymmetric model.

Notice that in Figs. 11 - 18, positive relative displacement signifies compression of the rock between the two points concerned, while negative relative displacement indicates expansion. Thus, for example, in Fig. 14, the predictions indicate that the rock between the two points (r = 1.5 m, z = 2.14 m) and (r = 3 m, z = 2.04 m) around the 3.6 kW heater is initially compressed and later expanded. The reason for this behavior is in the temporal variation of the temperature field rather than in the time-dependent thermomechanical response of the rock, since linear thermoelasticity has been assumed in the numerical models. At first the high-temperature zone has limited radial extent so that the rock within a radius of 1.5 m expands and compresses the colder rock between 1.5 m and 3 m. Later on, when a larger volume of rock becomes hot, the rock between the 1.5 m and 3 m radii also expands. Similar behavior is illustrated for the two points (r = 2.98 m, z = 1.81 m, and r = 4.23 m, z = 1.69 m) in the area of the 5 kW experiment, Fig. 18, although in this case, the switch-over from compression to expansion occurs at a much later time than in the example quoted above, since the two points involved are further away from the central heater than in the previous case.

The effect of turning on the peripheral heaters 204 days after the 5 kW central heater can be seen in all the plots of relative displacements, Figs.

Table 5. Maximum predicted relative horizontal displacements between two diametrically opposite anchor points (A and B) at 1.0 m radius from the axis of the central heater, or between the wall of the extensometer drift and an anchor point (D) at 6 m radius on a horizontal extensometer (E29) at a level 1.9 m below the midplane of Full-scale Experiment 2 (5 kW with peripheral heaters).

Phase	Time (days)	Maximum relative displacement (mm) between opposite anchor (A and B)		Maximum relative displacement (mm) between D and wall of extensometer drift	
		(a)	(b)	(a)	(b)
1	0 - 204	-0.94	-0.84	0.20	0.11
2	204 - 376	-2.14	-1.90	0.45	0.15
3	376 - 730	-1.97	-1.74	0.42	-0.34

Notes: (1) Phase 1 = only 5 kW central heater on;
Phase 2 = both central heater and peripheral heaters on;
Phase 3 = all heaters off.
(2) Positive relative displacement means compression
negative relative displacement means expansion
The displacements in this table are those with the largest magnitudes.
(3) Case (a) = drifts not modeled (M1)
Case (b) = drifts modeled (M7).

Table 6. Maximum predicted relative vertical displacements between two anchor points (A and C) 2.25 m above and below the midplane of the 5 kW heater, on a vertical extensometer (E16) at radius 1.5 m from the heater axis, or between an anchor point (A) 2.25 m above the midplane and the floor of the heater drift.

Phase	Time (days)	Maximum relative displacement (mm) between two anchor points (A and C)		between A and floor of heater drift	
		(a)	(b)	(a)	(b)
1	0 - 204	-1.39	-1.99	0.13	-0.38
2	204 - 376	-3.16	-4.60	-0.14	-1.05
3	376 - 730	-3.06	-4.48	-0.38	-1.12

Notes: (1) Phase 1 = only 5 kW central heater on;
Phase 2 = both central heater and peripheral heaters on;
Phase 3 = all heaters off.
(2) Positive relative displacement means compression
negative relative displacement means expansion
The displacements in this table are those with the largest magnitudes.
(3) Case (a) = drifts not modeled (M1)
Case (b) = drifts modeled (M7).

15 - 18, for Full-scale Experiment 2.

Additional plots can be generated as more experimental data are collected. This rapid data reduction process has been instrumental in the interpretation of the observed thermomechanical response of the granite rock mass. We shall not go into the details of comparison between predicted and measured displacements here. Preliminary results of this comparison has been reported by Cook and Hood (1978) and Hood (1979),[8] and further interpretation is continuing.

Table 5 summarizes, for the three different phases of Full-scale Experiment 2, the maximum predicted relative displacements between two anchor points (A and B) at 1 m radius on diametrically opposite sides of the 5 kW heater axis or between the wall of the extensometer drift and an anchor point (D) at 6 m radius on a horizontal extensometer (E29) at a level 1.9 m below the midplane of the heater array. Table 6 gives similar information for a vertical extensometer (E16) at a radius of 1.5 m from the 5 kW heater. The examples given in these two tables represent the largest relative horizontal and nearly largest relative vertical displacements, respectively, between any points in the rock instrumented with extensometer anchors. Clearly the maximum predicted relative vertical displacement is a few times greater than the maximum relative horizontal displacement.

[8] Although Hood's comparison was based mainly on the predicted displacements obtained from the present authors, any possible errors in this paper, especially in the discussion of the method of calculation, were entirely his own.

4.1.2. Stresses. Most of the stress results presented here will be for Full-Scale Experiment 2 (5 kW with peripheral heaters) according to Mesh 7 (i.e., with drifts taken into account). At the location of the "stress meters" the presence of the drifts has only minor effects on the thermal stress. Prior to the turn-on of the peripheral heaters, i.e., from 0 to 204 days, the thermally induced stresses for the two full-scale experiments are simply directly proportional to the thermal outputs of the two central heaters. For Full Scale Experiment 1 (3.6 kW) there are only minor changes in the stress field from 180 to 730 days since the temperature field has more or less stabilized (Chan, Cook, and Tsang, 1978). For Full Scale Experiment 2, the extra temperature rise due to the peripheral heaters leads to significant changes in the magnitude as well as distribution of the stresses.

In Figs. 19 and 20, the thermally induced radial, axial, and tangential stresses (σ_r, σ_z, σ_θ, labeled as S_R, S_z, S_θ in some of the computer-generated graphs, because Greek alphabets are not available from the computer plotter) in the midplane have been plotted at selected times against radial distance from the axis of the central heater in the two full-scale experiments. In Fig. 19 the predicted axial and tangential stresses from the finite element model (M1) are compared with the analytic solution for an infinitely long hollow cylinder (see appendix A for details). Note that in both the numerical and analytic solutions, the same temperature distribution from a finite line source solution has been input as the thermal load. The nearly exact agreement between the finite element and analytic solutions at an early time demonstrates that the finite element mesh is fine enough. With increased time, the two solutions begin to diverge more and more. This trend

can be understood by examining the temperature distribution at various times presented by Chan, Cook, and Tsang, 1978 (see especially Fig. 51 in that report). Shortly after the heater has been turned on, the high temperature isotherms are clustered around the heater and are almost all nearly parallel to the axis of the heater, i.e., the temperature distribution is nearly independent of axial distance. Therefore, the infinitely long, hollow cylinder solution, which assumes a purely radial temperature distribution, is a valid approximation to the actual thermally induced displacements and stresses due to a finite-length cylindrical heat source. As time progresses, the isotherms spread over a larger region and become more spheroidal in shape so that it is no longer a good approximation to assume, as was done in the analytic solution, that there is no axial temperature variation.

At short times, e.g., 0.5 day (Fig. 19 and Table 7 below), there is a short range of radial distances over which both the axial and tangential thermal stresses are tensile. This is a consequence of the very steep thermal gradient. The thermal expansion of the high temperature zone of the rock is restrained by the surrounding colder rock. This, in conjunction with the stress concentration factor due to the heater-hole, gives rise to very high compressive axial and tangential stresses near the wall of the hole and tensile stresses with extremely steep gradient at the transition zone where the temperature drops abruptly to a low value, as illustrated in Fig. 21. As the heat diffuses over a larger volume of rock and the thermal gradient becomes less steep with elapsed time, e.g., 8 days since the central heater has been on (Fig. 19), the tensile stresses decrease in magnitude and spread over a wider range of distances. Static equilibrium across the midplane

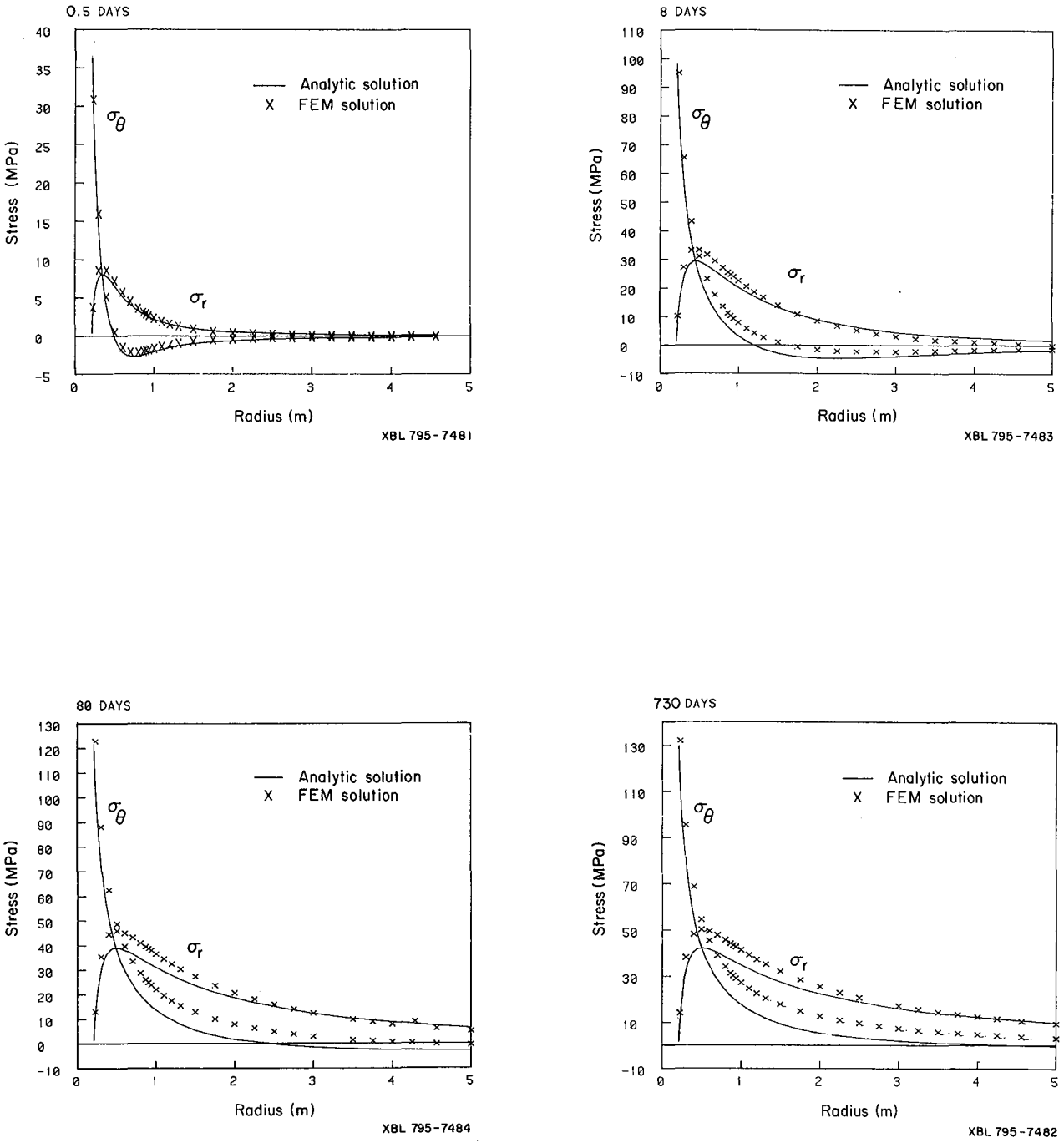

Fig. 19. Thermally induced radial (σ_r) and tangential (σ_θ) stresses along a radius from the center of a 3.6 kW cylindrical heater 2.44 m in length in a borehole 0.406 m in diameter at various times. Drifts not modeled. Compressive stress is positive .

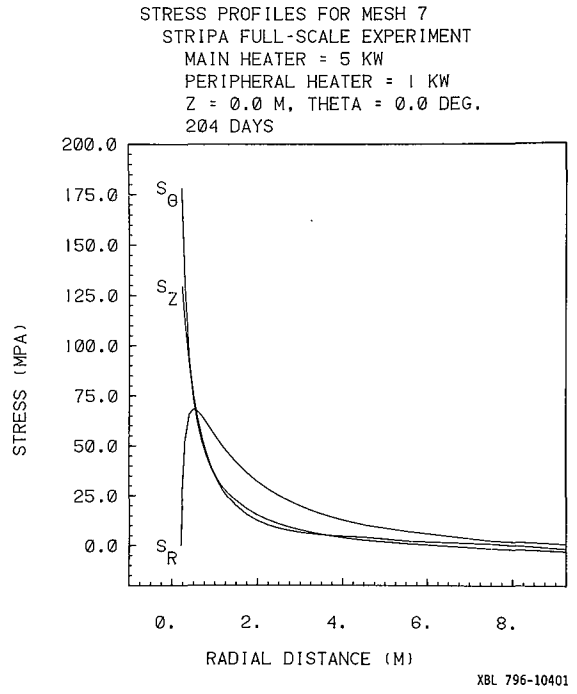

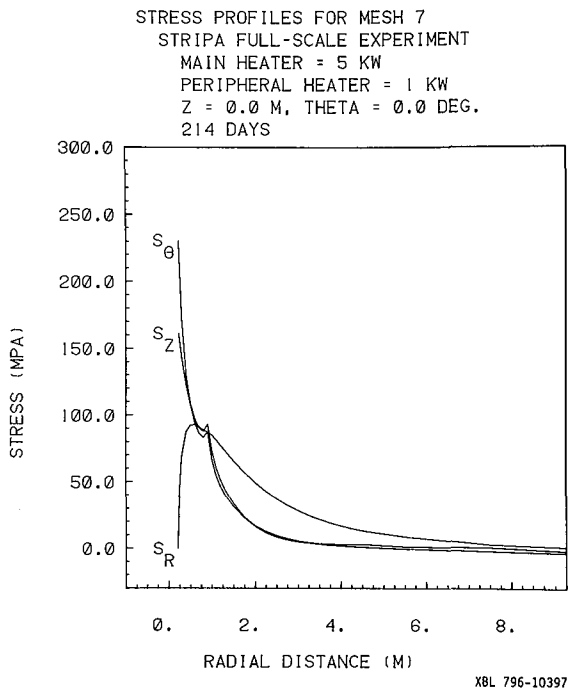

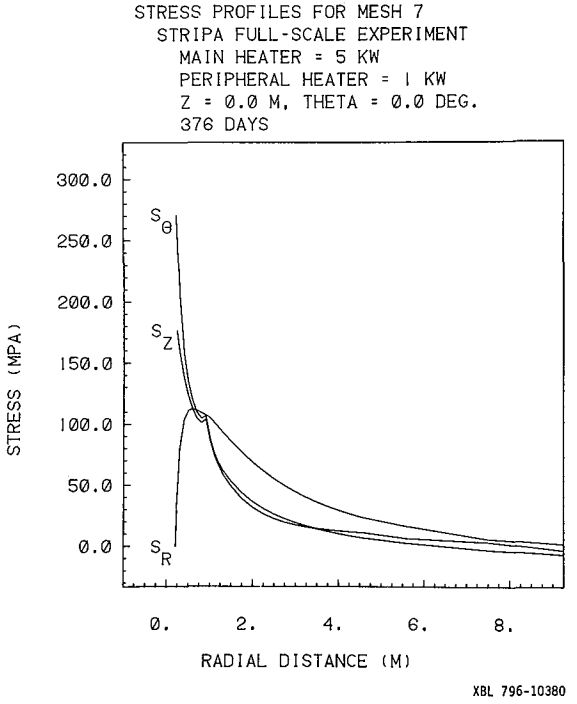

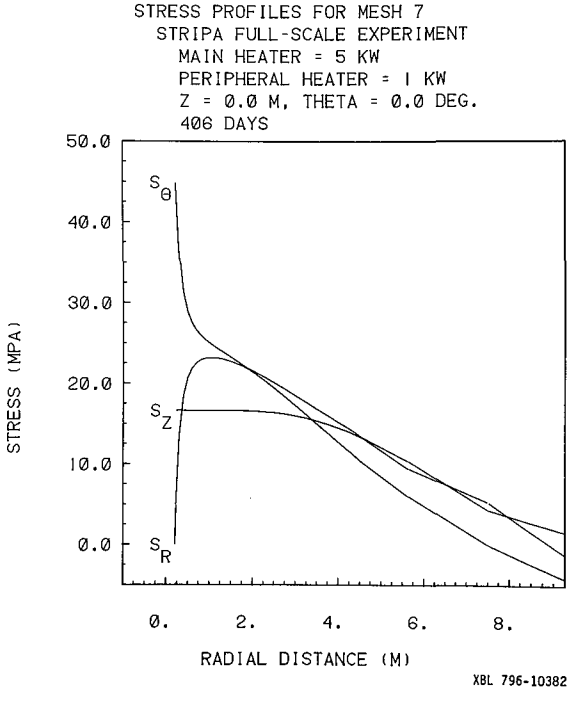

Fig. 20. Thermally induced radial (S_R), tangential (S_θ), and axial (S_z) stresses along a radius from the center of a 5 kW cylindrical heater 2.44 m in length in a borehole 0.406 m in diameter surrounded by a concentric ring of 4.27 m peripheral heaters operated at a nominal power of 1 kW, at various times. Drifts modeled. The symbols S_R, S_θ, and S_z are used in place of σ_r, σ_θ and σ_z because these plots were generated on a computer plotter that has no Greek alphabet characters.

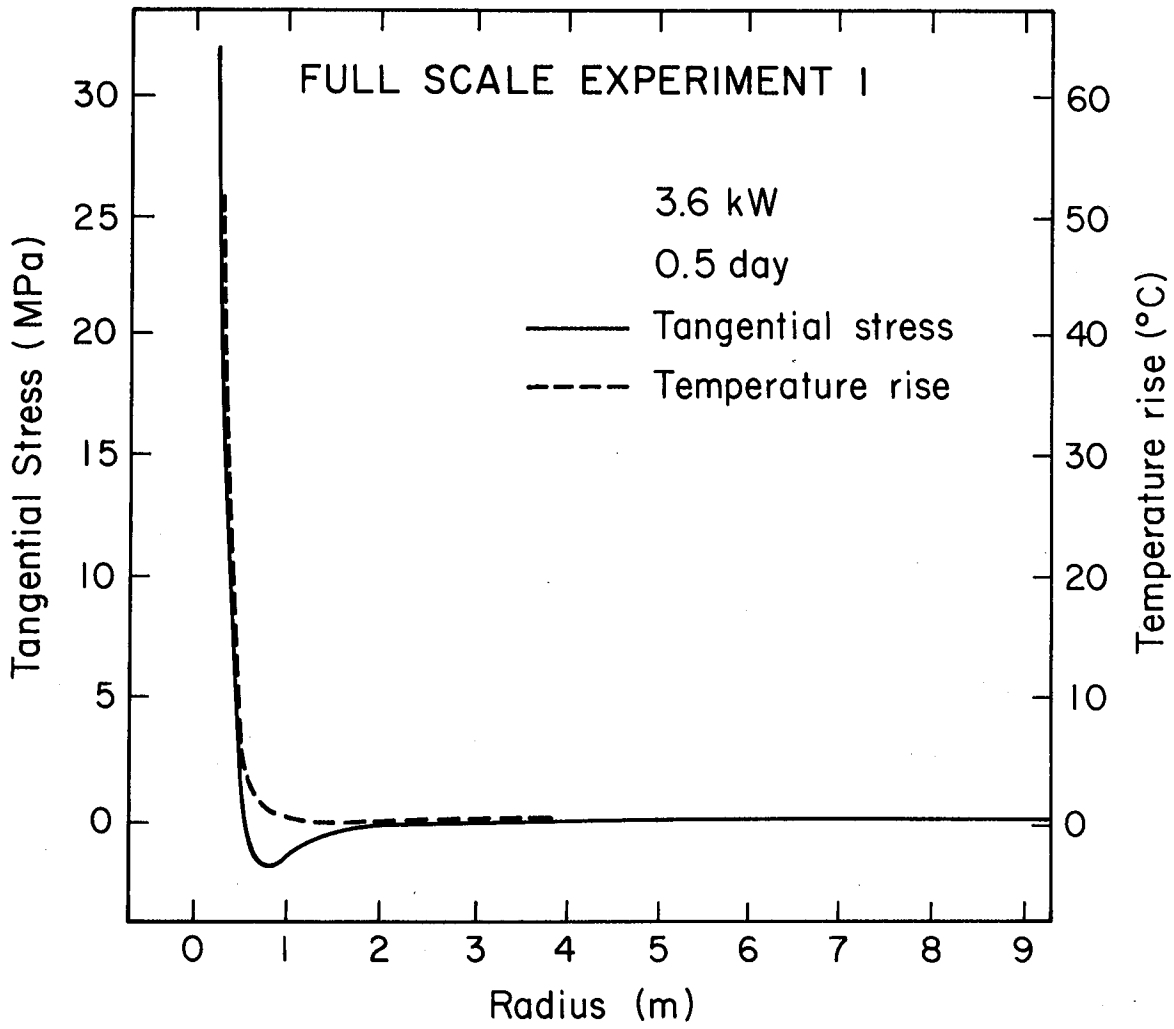

Fig. 21. Temperature (dashed) and thermally induced tangential stress (solid) along a radius from the center of a 3.6 kW cylindrical heater 2.44 m in length in a borehole 0.406 m in diameter after 0.5 days. Drifts not modeled .

requires that tensile stresses exist at any time[9]. However, beyond the first few weeks, the tensile stresses extend over such a long range that the magnitudes become insignificant.

Between 11 and 80 days, the stresses increase only slightly. At a particular instant, the tangential stress may be either greater or less than the axial stress, depending on spatial location. Similarly, at any particular point in space, either the tangential or axial stress may be greater depending on time. This has an important implication for the comparison of theoretical stresses with those measured by the United States Bureau of Mines (USBM) gauges, as further discussed in Appendix C.

In Full-Scale Experiment 2, the additional temperature rise in the rock due to the peripheral heaters, turned on 204 days after the 5 kW central heater, not only enhances the general level of the thermal stresses but also introduces a subsidiary peak at a radius of 0.9 m, as illustrated in Fig. 20 (214 and 376 days since the start of this experiment). After the heaters are turned off, the rapid cooling of the rock leads to radical changes in the magnitude as well as spatial distribution of stresses. An example of the radial distribution of the three normal components of thermal stress is shown in Fig. 20, 30 days after the heaters have been turned off, i.e., 406 days after the start of the experiment.

---

[9] For the benefit of those readers whose education has not included an elementary course in mechanics, this statement means that, if the midplane were a plane of symmetry, there would be no net load across it and therefore, $2\pi \int \sigma_z r dr = 2\pi \int \sigma_\theta r dr = 0$. Since the stresses are not identically zero everywhere, they must be positive over some range of r and negative elsewhere.

The relationship of the thermal stresses to the power history of the heaters can be seen more clearly in Fig. 22, where the thermal stresses are plotted as a function of time since the start of Full-Scale Experiment 2 at the wall of the 5 kW heater hole at midplane (Fig. 22a), and at a point in the rock 0.53 m below midplane at 1.59 m radius (Fig. 22b). For a period of about 30 days, both the tangential and axial stresses (σ_θ and σ_z) at the borehole increase very rapidly. Thereafter, the rise becomes more gradual, reaching a plateau after approximately 40 days for σ_z and 80 days for σ_θ. On day 204, just before the peripheral heaters are turned on, σ_θ and σ_z attained values of 215 MPa and 147 MPa, respectively. The rapid climb in stress immediately after the peripheral heaters are activated raises the values of σ_θ and σ_z to over 300 MPa and 200 MPa, respectively, at the end of the 40-day period during which each peripheral heater is operated at a power of 1 kW. The slight drop in stress after 244 days reflects the reduction of peripheral heater power from 1 kW to 0.85 kW each. Finally, the abrupt drop immediately after the heaters are turned off (at the end of 376 days) is essentially a reversal of the initial rapid rise associated with the turn-on.

Both the tangential and axial stresses reach values either falling within or exceeding the experimental range (208 $\pm$ 31 MPa) for the uniaxial compressive strength of small intact samples of Stripa granite (Swan, 1978). Since the rock mass is permeated by numerous discontinuities, it is expected to have a lower Young's modulus so that thermally induced stresses will be proportionally lower. However, the strength of the rock mass will also be correspondingly lower. Therefore, thermal decrepitation of the central

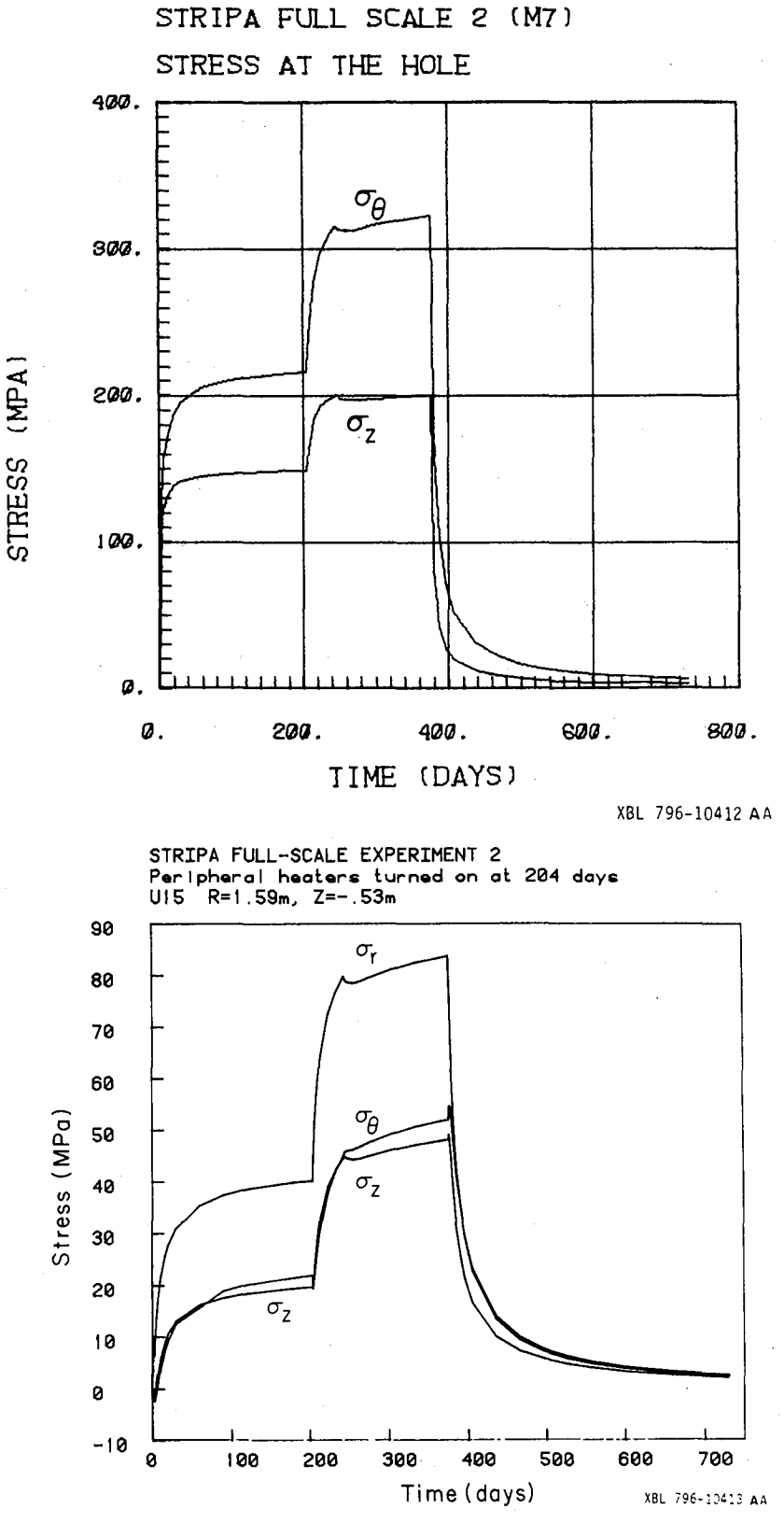

Fig. 22. Thermally induced radial (σ_r), axial (σ_z), and tangential (σ_θ) stresses as a function of time at (a) the wall of the central heater hole in the midplane and (b) at 1.59 m radius 0.53 m below midplane of Full-Scale Experiment 2 (5 kW with peripheral heaters). Note that for (a) the radial stress vanishes at the hole. Note also the correspondence between the stress histories and the power history given in Table 2. Drifts modeled.

heater hole is very likely, especially after the peripheral heaters have been on.

In a repository situation, borehole decrepitation would have two deleterious effects. First, it would make retrievability much more difficult. Second, the reduced thermal conductivity of the annulus of damaged rock may cause the waste to heat to unacceptable temperatures. In the Stripa experiment under consideration, the damaged zone around the heater hole is not expected to be very thick since the very high compressive stress (>200 MPa) penetrates only about 10 cm into the rock (see Fig. 20 above and Table 7 below). Under such circumstances, a crude estimate indicates that the extra temperature rise on the heater resulting from decrepitation would be less than 100°C.

The stress history for a point at radius 1.59 m (Fig. 22b), outside the ring of peripheral heaters, is similar in gross features to that at the wall of the central heater hole (Fig. 22a). There are, however, several differences in fine structure: (1) the radial stress, which vanishes at the heater hole, now exceeds either the tangential (σ_θ) or the axial (σ_z) stress; (2) there is an initial period after the central heater is turned on when steep thermal gradients give rise to tensile σ_θ and σ_z; (3) similarly, the thermal gradients that exist outside the ring of the peripheral heaters cause σ_θ and σ_z to decrease slightly over a short period of time after these heaters have been turned on; (4) finally, after all the heaters have been turned off, both σ_θ and σ_z exhibit a small compressive "blip" corresponding to the initial tensile blip when the heaters were turned on.

For a better illustration of the initial tensile period for the tangential and axial stresses, see Fig. C1 of Appendix C where the comparison between the predicted stresses and the quantities measured by the USBM gauges is discussed.

Table 7 gives a comprehensive summary of the three normal components of thermomechanical stresses obtained from the two different models (M1 and M7) at representative times and radial distances in the midplane of Full-Scale Experiment 2 (5 kW with peripheral heaters). This table should be self-explanatory. Salient features of the stress field have been (or will be) discussed in connection with the stress profiles and contours. One point that shows up more clearly in Table 7 is that tensile stresses of a few MPa also occur at the wall of the extensometer drift.

Samples of stress contours are given in Figs. 23-25 for Full-Scale Experiment 2. It is apparent that both at short- and long-time high compressive (axial and tangential) stresses, for example, over 100 MPa, occur in a prolate ellipsoidal shell of rock that roughly envelopes the central heater. The minor axis of the 100 MPa contour increases with time to approximately 0.75 m towards the end of the heating period. After the peripheral heaters have been turned on, a very high stress zone with $\sigma_\theta > 200$ MPa and $\sigma_z > 150$ MPa develops around the edge of the central heater hole. This zone extends about half way along the vertical length of the central heater and penetrates about 10 cm radially into the rock.

Table 7. Thermally induced radial, axial, and tangential stresses at representative time and radial distances in the midplane of Full-scale Experiment 2 (5 kW with peripheral heaters).

(a) Radial stress (MPa), Model M1 (drifts not modeled).

TIME (DAYS)	R=0.203 (M)	0.2265	0.3	0.6	1.0	2.0	3.0	4.0	7.5
.5	.0	5.3	12.0	8.0	3.3	.7	.2	.1	.0
3.0	.0	12.0	30.0	31.4	19.6	5.7	2.0	.9	.1
10.0	.0	15.8	40.5	47.7	35.1	14.9	6.6	3.2	.5
30.0	.0	18.1	46.9	58.0	45.7	23.9	13.2	7.7	1.6
90.0	.0	19.5	50.8	64.4	52.5	30.4	19.1	12.7	4.2
204.0	.0	20.2	52.6	67.4	55.7	33.7	22.2	15.7	6.5
207.0	.0	22.5	59.0	78.4	71.2	41.2	25.5	17.3	6.8
214.0	.0	25.8	68.2	93.1	85.8	51.5	31.5	20.7	7.5
244.0	.0	29.5	78.4	109.5	102.9	66.8	43.5	29.5	10.4
247.0	.0	29.3	77.9	108.5	101.4	66.4	43.6	29.8	10.6
376.0	.0	30.4	80.8	113.3	106.8	72.6	50.5	36.7	16.1
376.5	.0	24.9	68.3	104.1	98.8	70.2	49.5	36.2	16.0
379.0	.0	16.5	45.5	72.6	74.1	60.7	45.8	34.5	15.8
386.0	.0	9.9	27.2	44.1	46.6	43.0	36.4	29.6	15.0
406.0	.0	5.1	14.2	23.1	24.8	24.4	22.6	20.2	12.9
466.0	.0	2.2	6.1	10.0	10.7	10.9	10.6	10.1	8.1
600.0	.0	.9	2.5	4.1	4.5	4.6	4.5	4.4	4.0
730.0	.0	.6	1.5	2.5	2.7	2.8	2.8	2.7	2.5

(b) Axial stress (MPa), Model M1 (drifts not modeled).

TIME (DAYS)	R=0.203 (M)	0.2265	0.3	0.6	1.0	2.0	3.0	4.0	7.5
.5	55.6	44.6	29.5	3.0	-.8	-.3	-.1	-.1	-.0
3.0	108.1	92.8	74.1	29.2	7.2	-1.7	-.9	-.4	-.1
10.0	131.7	114.7	95.7	48.4	21.5	1.6	-1.4	-1.2	-.3
30.0	144.9	127.0	108.0	60.3	32.3	8.5	1.7	-.4	-.8
90.0	152.7	134.2	115.3	67.5	39.3	14.5	6.4	2.8	-.5
204.0	156.2	137.5	118.6	70.8	42.6	17.6	9.2	5.3	.8
207.0	171.0	151.5	133.1	89.3	67.8	17.6	8.0	4.7	.6
214.0	193.2	172.3	153.7	108.5	83.7	23.6	8.5	3.9	.3
244.0	214.7	192.3	173.8	128.0	101.9	36.4	15.7	7.0	-.2
247.0	213.4	191.0	172.4	126.0	98.9	37.1	16.3	7.4	-.2
376.0	218.3	195.5	177.0	130.9	104.3	43.9	23.6	14.0	2.7
376.5	163.2	151.4	147.7	125.2	94.6	44.8	24.0	14.2	2.8
379.0	97.9	91.0	90.7	86.0	75.8	45.7	25.6	15.1	3.0
386.0	55.7	51.7	51.8	50.8	48.3	37.7	26.0	16.8	3.7
406.0	28.2	26.2	26.3	26.1	25.6	23.0	19.2	15.1	5.1
466.0	11.9	11.0	11.1	11.1	11.0	10.5	9.7	8.7	5.1
600.0	4.9	4.5	4.5	4.5	4.5	4.5	4.3	4.1	3.1
730.0	2.9	2.7	2.7	2.7	2.7	2.7	2.6	2.6	2.2

(c) Tangential stress (MPa), Model M1 (drift not modeled).

TIME (DAYS)	R=0.203 (M)	0.2265	0.3	0.6	1.0	2.0	3.0	4.0	7.5
.5	58.2	42.8	22.2	-1.9	-2.2	-.4	-.1	-.1	-.0
3.0	129.2	103.3	68.2	17.5	1.4	-2.5	-1.1	-.5	-.1
10.0	169.7	138.5	96.5	36.5	14.5	.0	-1.8	-1.4	-.3
30.0	194.1	159.8	113.8	49.2	25.3	6.7	1.1	-.7	-.8
90.0	209.1	172.8	124.4	57.1	32.5	12.7	5.8	2.6	-.4
204.0	216.0	178.8	129.3	60.9	35.9	15.9	8.7	5.1	.9
207.0	240.0	199.9	146.9	77.3	54.0	13.4	6.9	4.3	.7
214.0	275.5	230.8	171.9	94.8	67.3	17.7	6.6	3.2	.4
244.0	314.3	264.6	199.4	115.1	84.9	29.7	13.2	5.9	-.1
247.0	312.4	262.9	197.9	113.6	83.0	30.7	13.9	6.4	-.1
376.0	323.3	272.4	205.7	119.7	89.2	38.0	21.5	13.1	2.9
376.5	263.5	228.1	182.0	118.3	83.7	39.6	22.0	13.4	3.0
379.0	174.0	151.4	122.7	88.4	72.6	42.8	24.2	14.4	3.2
386.0	103.9	90.6	73.6	54.8	48.5	36.9	25.5	16.5	3.9
406.0	54.1	47.1	38.4	28.9	26.4	23.1	19.3	15.2	5.3
466.0	23.2	20.2	16.5	12.5	11.6	10.8	9.9	8.9	5.2
600.0	9.7	8.4	6.9	5.2	4.8	4.6	4.4	4.2	3.2
730.0	5.8	5.1	4.1	3.1	2.9	2.8	2.7	2.6	2.2

(d) Radial stress (MPa), Model M7 (drift not modeled).

TIME (DAYS)	R=0.203 (M)	0.2265	0.3	0.6	1.0	2.0	3.0	4.0	7.5
.5	.0	5.3	12.0	8.1	3.3	.7	.2	.1	.0
3.0	.0	12.0	30.0	31.5	19.6	5.6	1.9	.8	.1
10.0	.0	15.8	40.6	47.9	35.1	14.6	6.2	2.8	.3
30.0	.0	18.2	47.0	58.2	45.7	23.3	12.3	6.7	.8
90.0	.0	19.6	50.9	64.4	52.3	29.4	17.4	10.7	2.1
204.0	.0	20.2	52.5	67.1	55.1	32.1	19.8	12.8	3.0
207.0	.0	22.5	58.9	78.2	70.6	39.5	22.9	14.2	3.1
214.0	.0	25.8	68.3	92.9	85.2	49.6	28.5	17.0	3.4
244.0	.0	29.5	78.4	109.3	102.2	64.1	39.3	24.5	4.9
247.0	.0	29.3	77.9	108.4	100.6	63.7	39.4	24.7	5.0
376.0	.0	30.2	80.4	112.5	105.2	68.8	44.6	29.6	7.1
376.5	.0	24.8	68.0	103.3	97.3	66.4	43.7	29.2	7.1
379.0	.0	16.3	45.1	71.7	72.6	57.0	40.2	27.7	7.0
386.0	.0	9.7	26.7	43.1	45.0	39.6	31.3	23.5	6.6
406.0	.0	4.9	13.5	21.9	23.2	21.6	18.5	15.2	5.4
466.0	.0	2.0	5.5	8.9	9.5	9.0	8.0	6.9	2.8
600.0	.0	.8	2.2	3.6	3.8	3.6	3.2	2.8	1.1
730.0	.0	.5	1.3	2.1	2.2	2.1	1.9	1.7	.6

(e) Axial stress (MPa), Model M7 (drift modeled).

TIME (DAYS)	R=0.203 (M)	0.2265	0.3	0.6	1.0	2.0	3.0	4.0	7.5
.5	55.5	44.5	29.4	2.9	-.9	-.3	-.1	-.1	-.0
3.0	107.5	92.2	73.5	28.6	6.7	-2.0	-1.1	-.4	-.1
10.0	129.9	112.9	94.0	46.6	19.9	.6	-1.9	-1.3	-.2
30.0	140.8	122.9	103.9	56.2	28.5	5.9	.5	-.7	-.6
90.0	146.1	127.7	108.7	60.9	33.2	10.3	4.3	2.3	-.0
204.0	148.4	129.7	110.7	62.9	35.3	12.5	6.7	4.8	1.5
207.0	162.1	142.6	124.2	80.4	59.4	11.9	5.2	4.1	1.4
214.0	182.3	161.4	142.8	97.6	73.4	16.6	5.1	3.2	1.2
244.0	199.2	176.7	158.1	112.4	87.2	26.4	10.7	5.9	1.0
247.0	197.7	175.3	156.7	110.3	84.1	27.0	11.3	6.3	1.1
376.0	199.5	176.8	158.2	112.1	86.6	31.8	17.6	12.8	4.6
376.5	144.6	132.9	129.1	106.8	77.3	32.8	18.0	13.0	4.6
379.0	80.5	73.6	73.3	68.7	59.5	34.4	20.0	13.9	4.8
386.0	41.1	37.1	37.2	36.3	34.6	28.0	21.2	15.8	5.3
406.0	18.6	16.6	16.7	16.6	16.7	16.6	16.0	14.5	6.5
466.0	7.5	6.7	6.7	6.8	7.0	7.7	8.5	8.8	6.3
600.0	3.1	2.8	2.8	2.8	2.9	3.4	3.9	4.3	4.0
730.0	1.9	1.7	1.7	1.7	1.8	2.1	2.5	2.8	2.8

(f) Tangential stress (MPa), Model M7 (drifts modeled).

TIME (DAYS)	R=0.203 (M)	0.2265	0.3	0.6	1.0	2.0	3.0	4.0	7.5
.5	58.3	42.9	22.3	-1.9	-2.2	-.4	-.1	-.1	-.0
3.0	129.4	103.5	68.4	17.6	1.5	-2.5	-1.1	-.5	-.1
10.0	170.1	138.8	96.8	36.7	14.6	.1	-1.9	-1.4	-.5
30.0	194.7	160.2	114.2	49.4	25.4	6.7	1.0	-.9	-1.3
90.0	209.3	173.0	124.5	57.2	32.5	12.5	5.4	2.0	-1.6
204.0	215.7	178.6	129.1	60.6	35.6	15.4	7.9	4.1	-1.2
207.0	239.8	199.8	146.8	77.2	53.7	12.9	6.1	3.2	-1.4
214.0	275.6	230.9	171.9	94.8	67.2	17.2	5.7	2.0	-1.9
244.0	314.5	264.8	199.5	115.1	84.8	29.1	12.1	4.4	-3.3
247.0	312.5	263.0	198.0	113.5	82.9	30.1	12.8	4.8	-3.3
376.0	322.1	271.3	204.8	118.9	88.4	36.6	19.4	10.4	-2.3
376.5	262.2	226.9	181.1	117.5	82.8	38.2	20.0	10.7	-2.3
379.0	172.4	150.0	121.5	87.5	71.6	41.3	22.1	11.7	-1.9
386.0	101.9	88.7	72.2	53.6	47.3	35.4	23.4	13.9	-1.1
406.0	51.6	45.0	36.6	27.6	25.1	21.5	17.3	12.8	.8
466.0	21.0	18.3	14.9	11.3	10.4	9.5	8.4	7.1	2.1
600.0	8.3	7.3	5.9	4.5	4.2	3.9	3.6	3.2	1.5
730.0	5.0	4.3	3.5	2.7	2.5	2.3	2.2	2.0	1.1

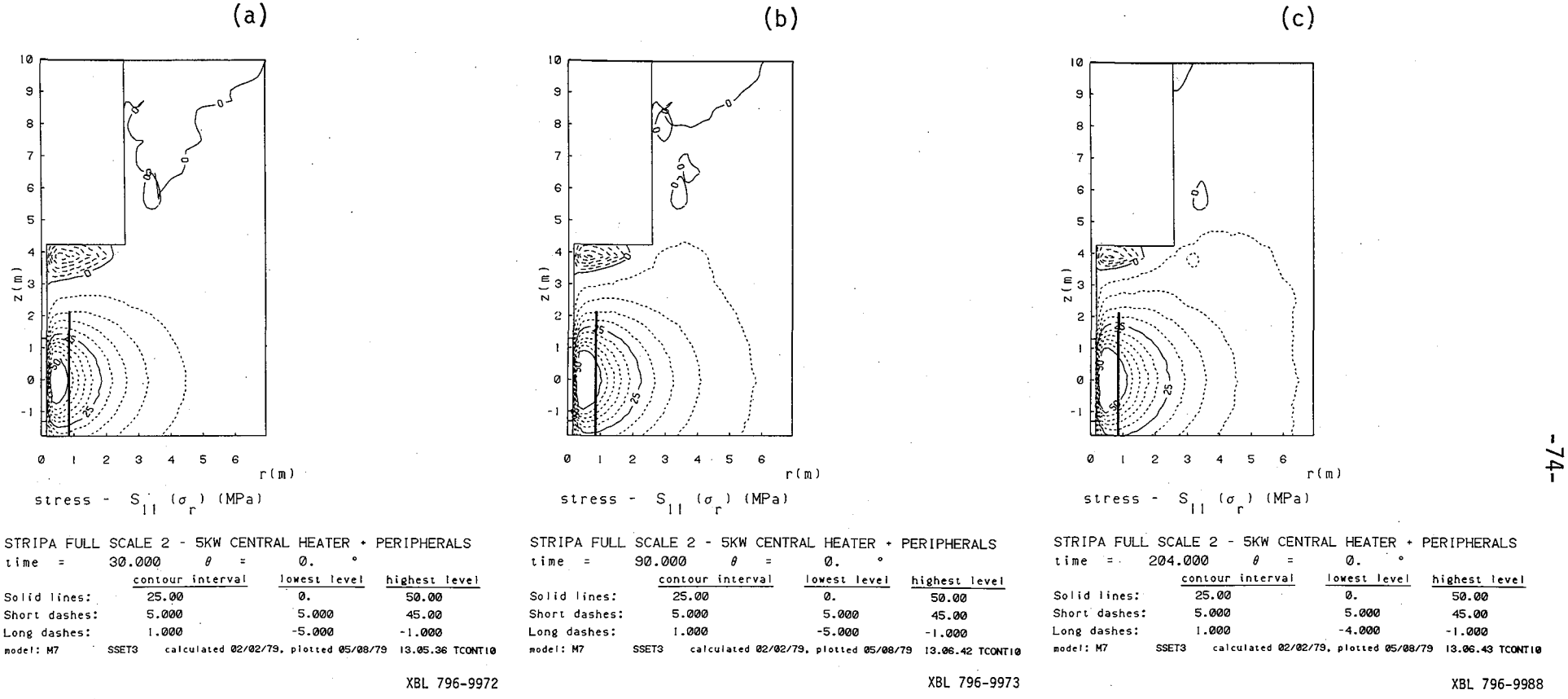

Fig. 23a-c. Contour plots of thermally induced radial stress in the axial (r - z) plane of Full-Scale Experiment 2 (5 kW with peripheral heaters) at various times: (a) 30 days, (b) 90 days, (c) 204 days. Contour interval: solid = 25 MPa, short dashes = 5 MPa, long dashes = 1 MPa. Drifts modeled.

(d)

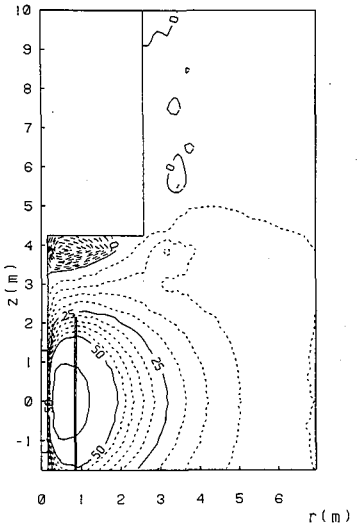

STRIPA FULL SCALE 2 - 5KW CENTRAL HEATER + PERIPHERALS
time = 214.000 θ = 0. °

	contour interval	lowest level	highest level
Solid lines:	25.00	0.	75.00
Short dashes:	5.000	5.000	45.00
Long dashes:	1.000	-10.00	-1.000

model: M7 SSET3 calculated 02/02/79, plotted 05/08/79 13.06.46 TCONTI0

XBL 796-9916

(e)

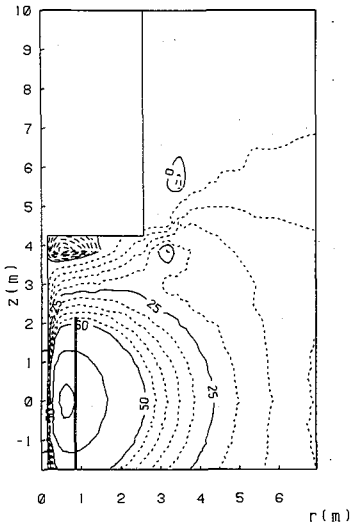

STRIPA FULL SCALE 2 - 5KW CENTRAL HEATER + PERIPHERALS
time = 376.500 θ = 0. °

	contour interval	lowest level	highest level
Solid lines:	25.00	0.	100.0
Short dashes:	5.000	5.000	45.00
Long dashes:	1.000	-7.000	-1.000

model: M7 SSET3 calculated 02/02/79, plotted 05/08/79 13.08.01 TCONTI0

XBL 796-9978

(f)

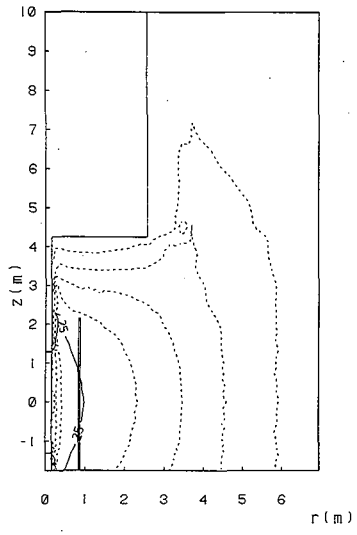

STRIPA FULL SCALE 2 - 5KW CENTRAL HEATER + PERIPHERALS
time = 406.000 θ = 0. °

	contour interval	lowest level	highest level
Solid lines:	25.00	25.00	25.00
Short dashes:	5.000	5.000	40.00

model: M7 SSET3 calculated 02/02/79, plotted 05/08/79 13.04.31 TCONTI1

XBL 796-9921

Fig. 23d-f. Contour plots of thermally induced radial stress in the axial (r - z) plane of Full-Scale Experiment 2 (5 kW with peripheral heaters) at various times: (d) 214 days, (e) 376 days, (f) 406 days. Contour interval: solid = 25 MPa, short dashes = 5 MPa, long dashes = 1 MPa. Drifts modeled.

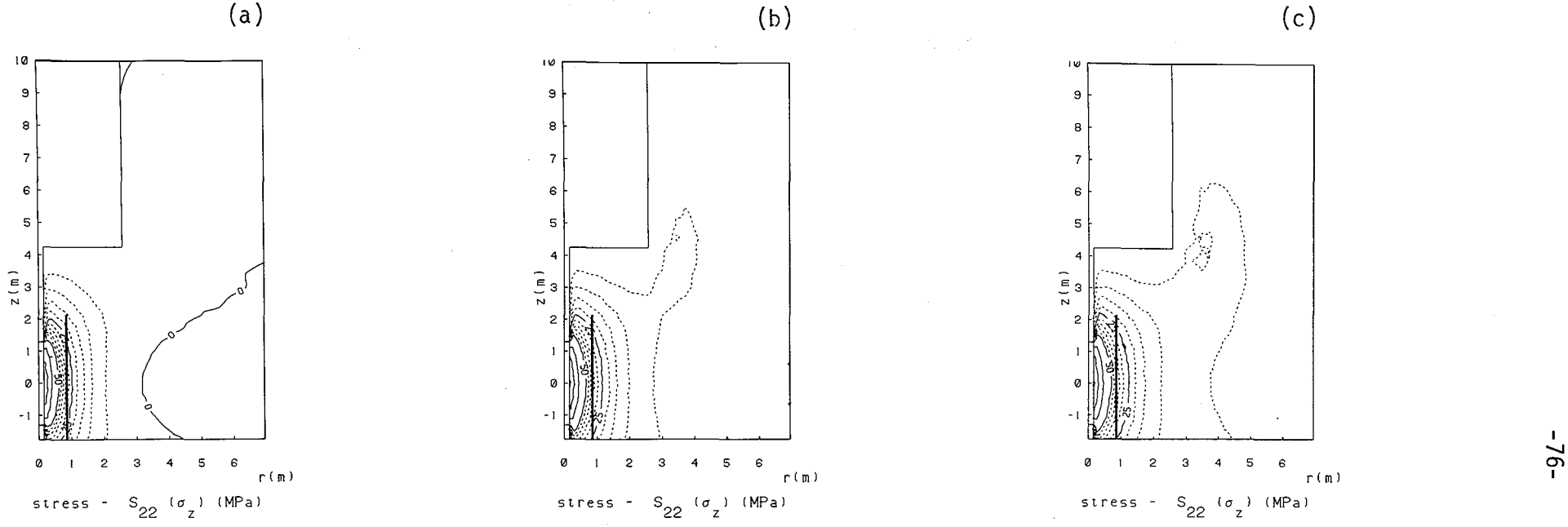

Fig. 24a-c. Contour plots of thermally induced axial stress in the axial (r - z) plane of Full-Scale Experiment 2 (5 kW with peripheral heatrs) at various times: (a) 30 days, (b) 90 days, (c) 204 days. Contour interval: solid = 25 MPa, short dashes = 5 MPa, long dashes = 1 MPa. Drifts modeled.

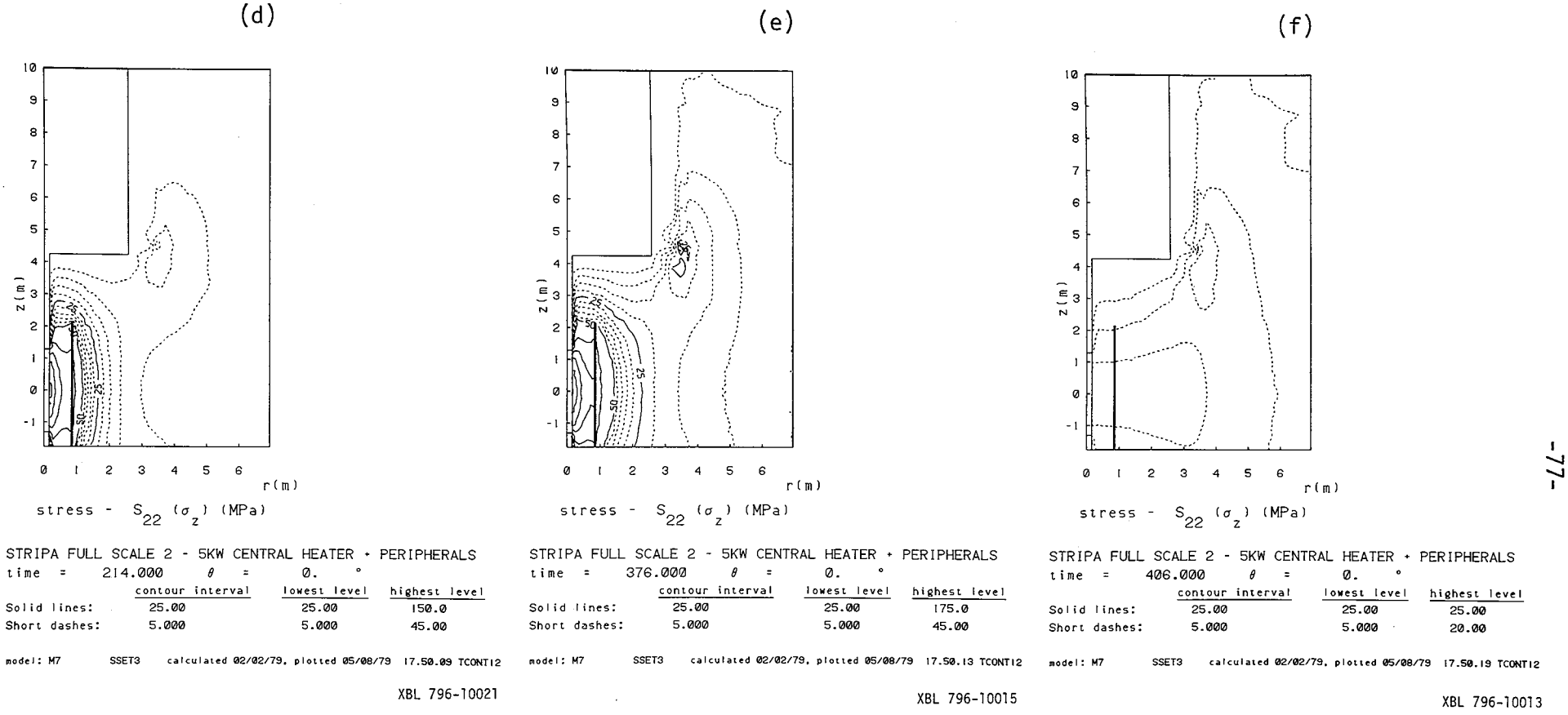

Fig. 24d-f. Contour plots of thermally induced radial stress in the axial (r - z) plane of Full-Scale Experiment 2 (5 kW with peripheral heaters) at various times: (d) 214 days, (e) 376 days, (f) 406 days. Contour interval: solid = 25 MPa, short dashes = 5 MPa, long dashes = 1 MPa. Drifts modeled.

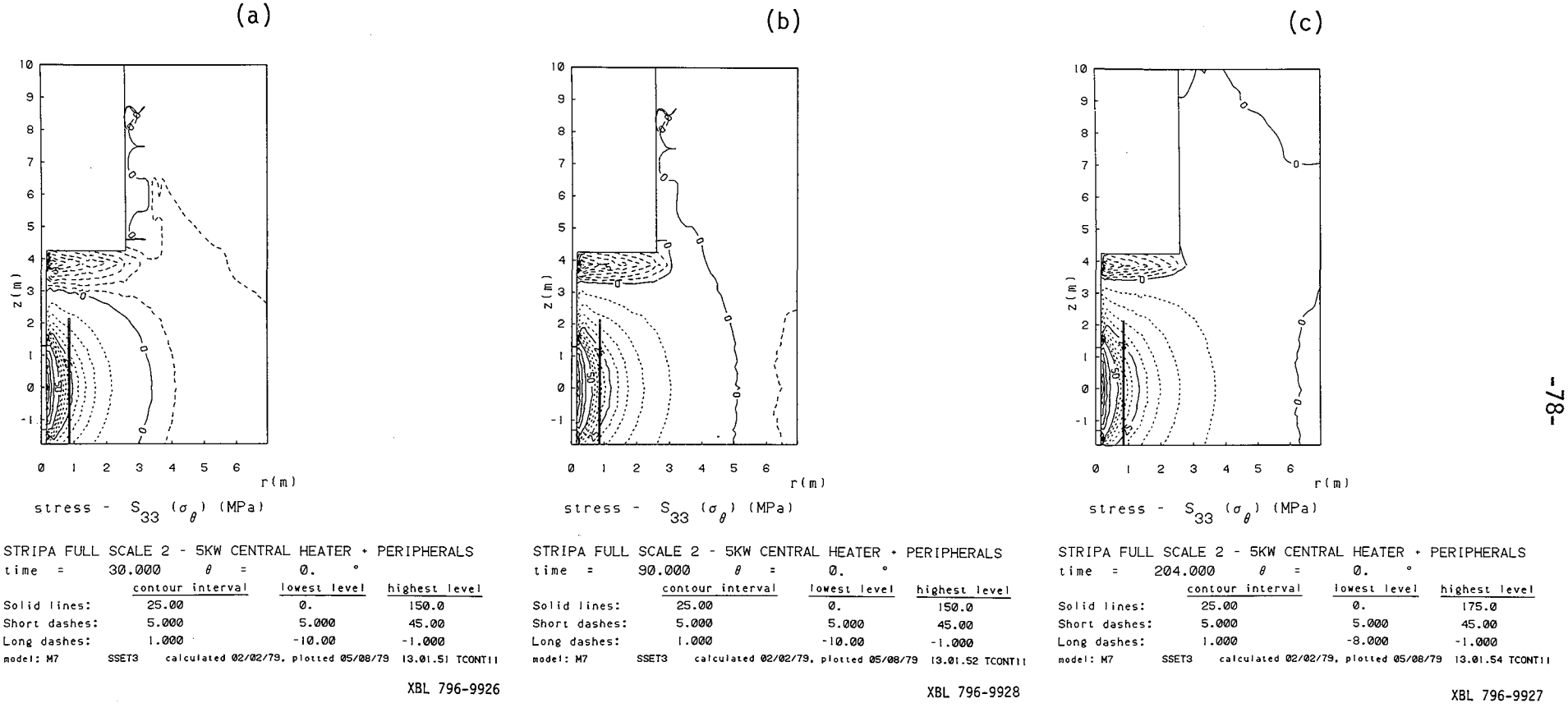

Fig. 25a-c. Contour plots of thermally induced tangential stress in the axial (r - z) plane of Full-Scale Experiment 2 (5 kW with peripheral heaters) at various times: (a) 30 days, (b) 90 days, (c) 204 days. Contour interval: solid = 25 MPa, short dashes = 5 MPa, long dashes = 1 MPa. Drifts modeled.

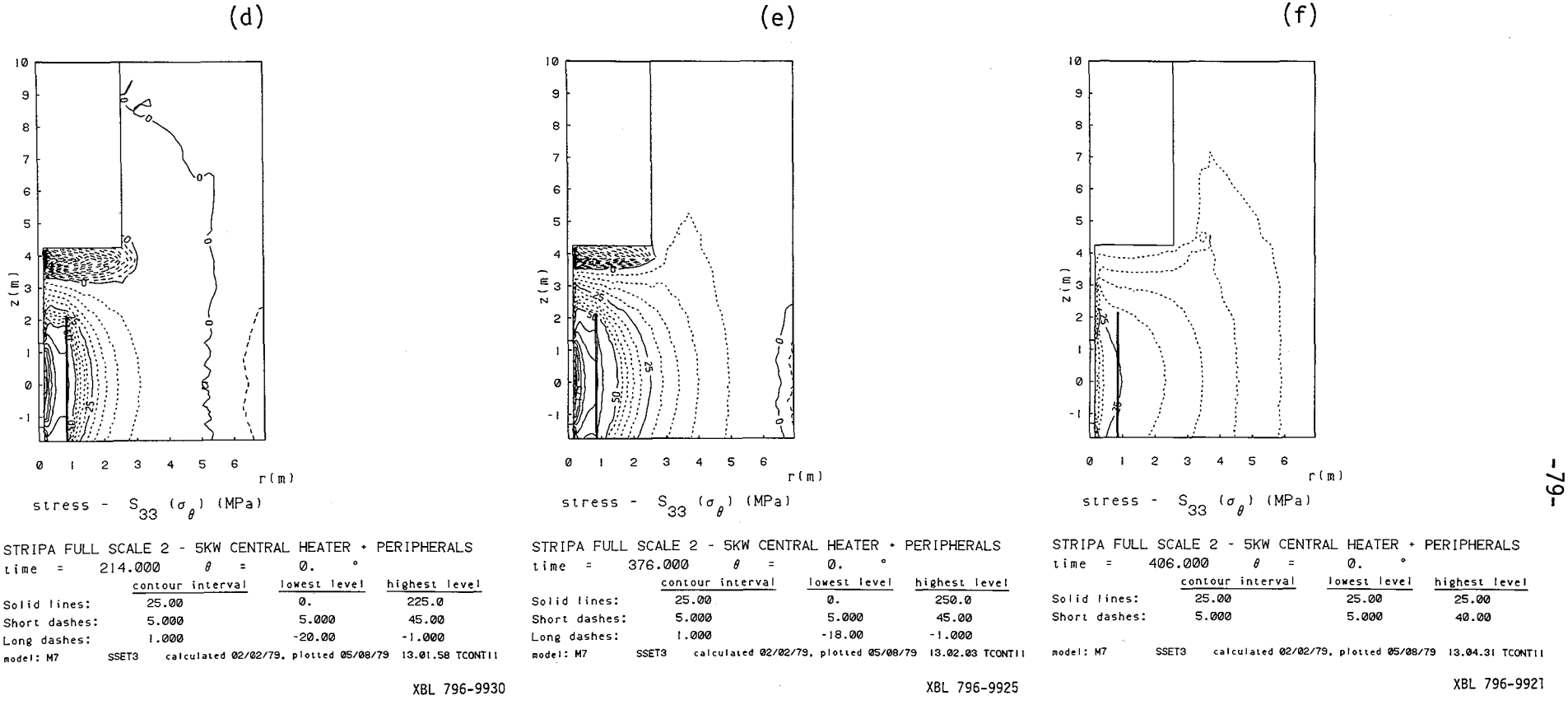

Fig. 25d-f. Contour plots of thermally induced tangential stress in the axial (r - z) plane of Full Scale Experiment 2 (5 kW with peripheral heaters) at various times: (d) 214 days, (e) 376 days, (f) 406 days. Contour interval: solid = 25 MPa, short dashes = 5 MPa, long dashes = 1 MPa. Drifts modeled.

High compressive radial stress occurs in a region with a D-shaped meridional (i.e., r-z) section. The 50 MPa contour begins to appear 30 days after the central heater is turned on and grows with time, reaching a vertical extent of 1 m above and below the midplane and a radial extent of 0.25 m to 1.25 m just before the peripheral heaters are turned on. After the peripheral heaters have been turned on, the 50 MPa σ_r-contour expands rapidly, and a small zone of $\sigma_r > 100$ MPa appears towards the end of the heating period.

Two zones of tensile thermal stresses can be identified, one along the midplane of the heaters (for σ_z and σ_θ) and another beneath the floor of the heater drift (for σ_r and σ_θ). The first zone which results from steep thermal gradients practically disappears for time periods longer than a few weeks and never exceeds 3 MPa in magnitude, while the second zone, which results from the combined effects of a vertical gradient and the existence of a free surface, persists. During the period when only the 5 kW heater is operating the largest magnitude of tensile stresses beneath the floor of the drift are 5 MPa and 10 MPa for σ_r and σ_θ, respectively. Thirty days after the turn-on of the peripheral heaters, the tensile radial and tangential stress beneath the floor of the drift reach maximum magnitudes of 10 MPa and 20 MPa,[10] respectively. These values are comparable to the mean <u>in situ</u> secondary horizontal principal stresses of 16 MPa and 9 MPa measured by

---

[10]The numerical values require further confirmation since the temperature distribution was calculated using an infinite medium approximation to avoid discontinuity at the periphery of the heater drift. Nonetheless, there is little question that tensile stresses are induced beneath the floor since these occur even shortly after turn-on of the central heater, when the boundary condition nardly plays any role at all.

Carlsson (1978b). Although the rock mass may not be able to sustain and transmit such high tensile stresses, the net compressive stress will certainly be drastically reduced. It is, therefore, likely that the aperture of preexisting cracks may increase, thereby increasing the permeability of the rock mass. Measurements of displacement across a fracture on the floor of the drift (Carlsson, 1978a) should be attempted. Furthermore, it would also be useful to look for possible correlation between the evolution of the stress field and water flow data.

4.1.3. Interference between the two full-scale experiments. In a previous report (Chan, Cook, and Tsang, 1978), it was concluded that the temperature fields in the heater experiments are localized so that the two full-scale experiments separated by a distance of 22 m are virtually thermally independent. Thermally induced displacements, however, are cumulative and persist over much longer distances than temperatures. Consequently, the displacement fields of the two experiments interfere quite strongly, especially during the latter part of the test duration. In Fig. 26 the radial displacements of the individual experiments after 730 days, as well as the superimposed displacement, are plotted along the center-to-center line in the midplane, with displacement away from the 5 kW heater taken as positive. The predicted data used for this interference plot is from Model Series 2 (see Table 2). Here it has been assumed that the two experiments are turned on simultaneously. Clearly, both the magnitude and spatial variation of the superimposed displacement differ substantially from those due to either experiment alone. Thus, for example, at a radial distance of 2 m from the 3.6 kW heater, the radial displacement due to this heater, which is about

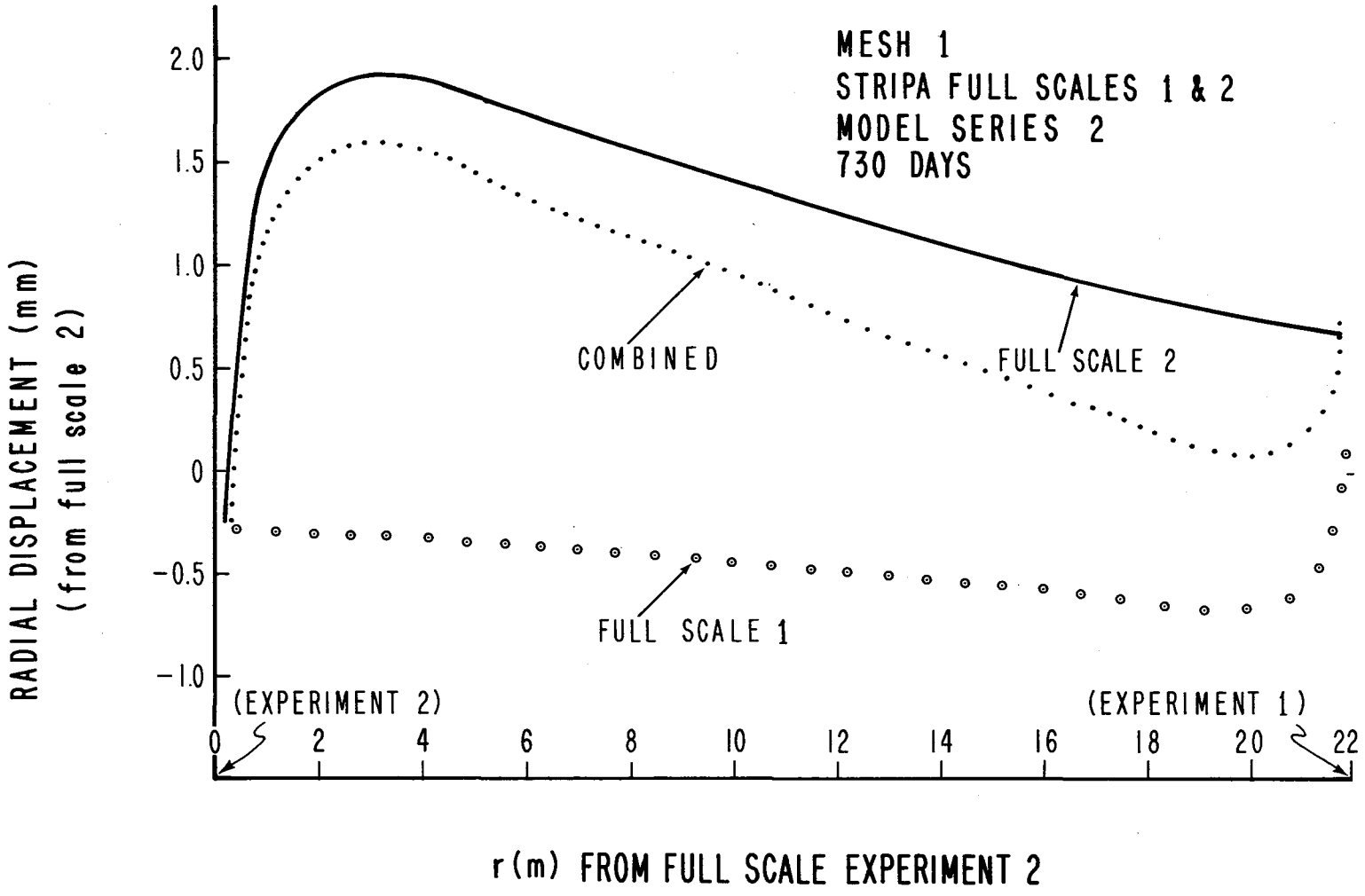

XBL 788-2002AA

Fig. 26. Interference plot for radial displacement for the two full-scale heater experiments at the end of 730 days. Displacement is plotted as a function of distance from the 5 kW heater in Full-Scale Experiment 2 along the line joining the midpoints of the two main heaters. Radial displacement away from the 5 kW heater is taken as positive. All heaters assumed turned on simultaneously. Drifts not modeled.

0.6 mm had this heater been operated by itself, is completely nullified by that of the other full-scale experiment after 730 days. In other words, the two experiments are "running into each other." Similar interaction occurs also in the vertical displacements, as shown in Fig. 27, for a point midway between the two central heaters at the level of the heater drift. Notice that the displacements illustrated here are obtained using Mesh 1 which does not take into account the existence of the drifts. Because of the assumption of axisymmetry (see Section 3), neither Mesh 1 nor Mesh 7 is strictly valid for this spatial location. The main purpose of Figs. 26 and 27 is just to illustrate the degree of interaction. The interference between the two displacement fields is maximum along the center-to-center line but less serious along other directions. Fortunately, since the horizontal extensometers are either normal to or inclined at 45° to the extensometer drift while the vertical extensometers all lie within a radius of less than 5 m from either full-scale heater, the measured displacements will be affected to a much lesser extent than the examples shown in Figs. 26 and 27. The interference is further reduced if we consider the fact that because of a revision of the test plan, the two full-scale experiments will be turned off after approximately one year of operation.

At the present state of knowledge, it is necessary to compare the measured displacements with the superposed theoretical displacements only if significant discrepancy is found between the displacement measured by corresponding pairs of extensometers in the region between the two full-scale heaters and outside of that region.

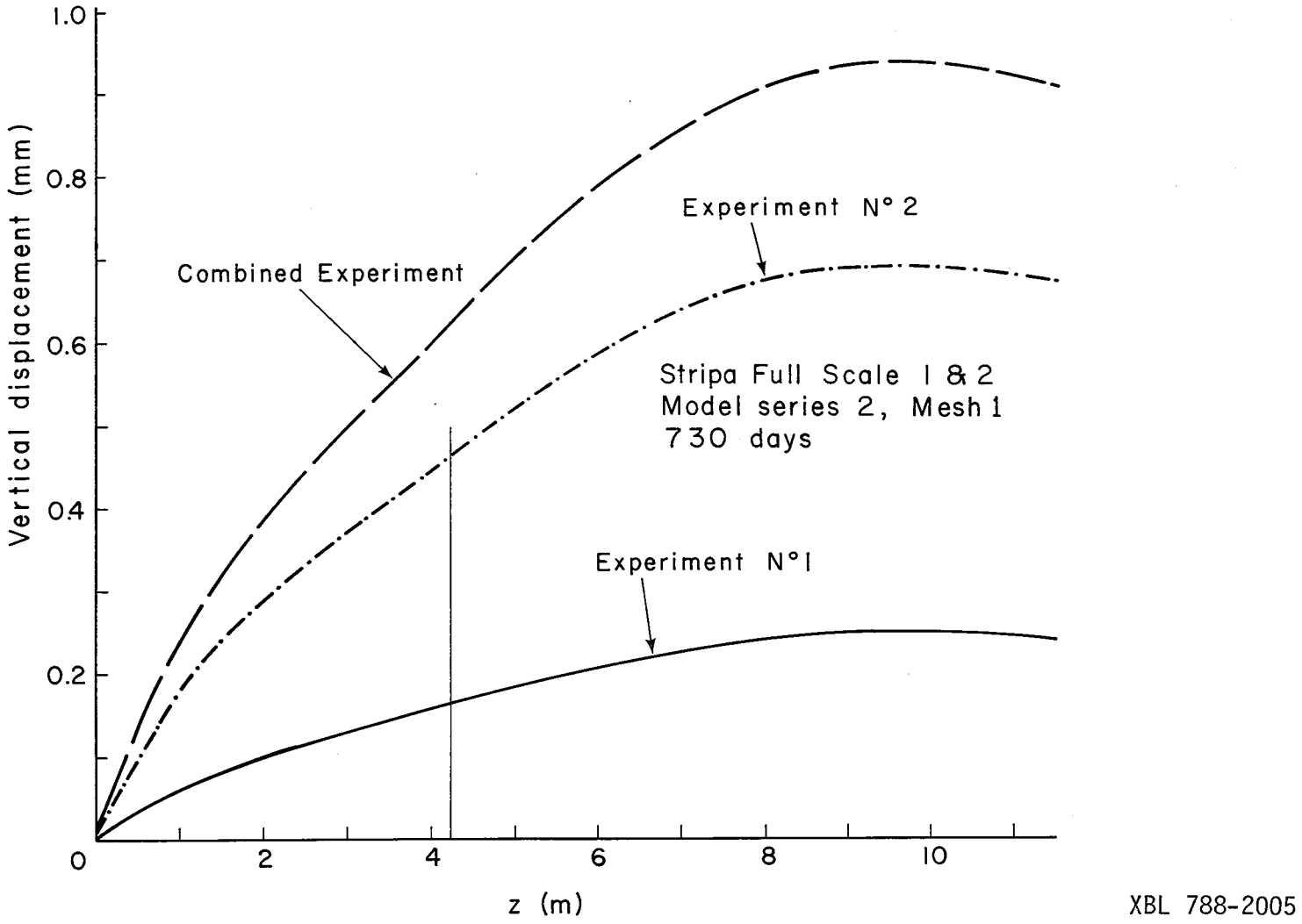

Fig. 27. Interference plot for vertical displacement at the end of 730 days for the two full-scale heater experiments at a point midway along the center-to-center line of the two heaters, i.e., 11 m from each main heater. All heaters assumed turned on simultaneously. Drifts not modeled.

The interaction between the stress fields of the two full-scale experiments, illustrated in Fig. 28 for the radial component, is weaker than in the case of the displacement fields, although it is still not entirely negligible. Again the interaction displayed here is along a line joining the centers of heaters and represents the extreme case. Also, the interaction between the two experiments is weaker for the other two normal stresses.

4.2. Time-scaled Experiment

In the Time-Scaled Experiment, there are five vertical extensometers to measure the displacement, but no stress-measuring devices. Hence only the displacement results will be given here.

In Fig. 29 the relative displacements between various pairs of extensometer anchor points are plotted against time up to 180 days for all five extensometers. The locations of the extensometer holes can be seen in Fig. 30, whereas the designations of the anchors are indicated in the inset of Fig. 29. A preliminary comparison between measured and predicted displacements has been given by Cook and Hood (1978) and will not be repeated here.

The following features may be noted for the predicted relative displacements: (1) except for the pair B-A, the relative displacements for all the pairs of points illustrated are negative, i.e., the rock expands between these points; (2) between two points 3 m (B) and 7 m (A) above the midplane of the heater array, for every extensometer, the rock first undergoes expansion and then compression reflecting the finite amount of time required for heat diffusion as previously explained with reference to the full-scale experiments; (3) the relative displacement between pairs of anchor points

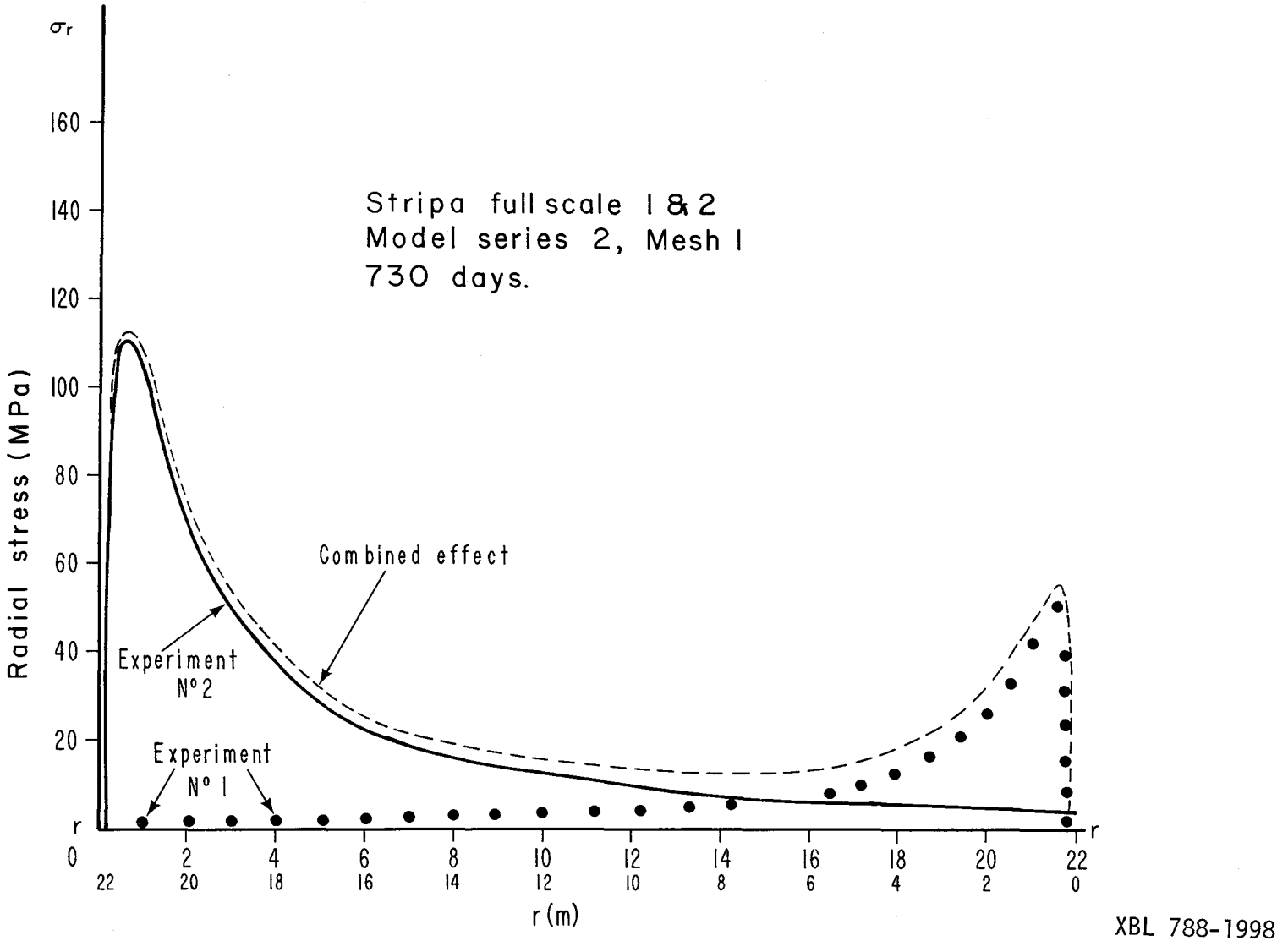

Fig. 28. Interference plot for thermally induced radial stress for the two full-scale heater experiments at the end of 730 days. Numbers above horizontal axis show distances from the 5 kW heater in Full-Scale Experiment 2. All heaters assumed turned on simultaneously. Drifts not modeled.

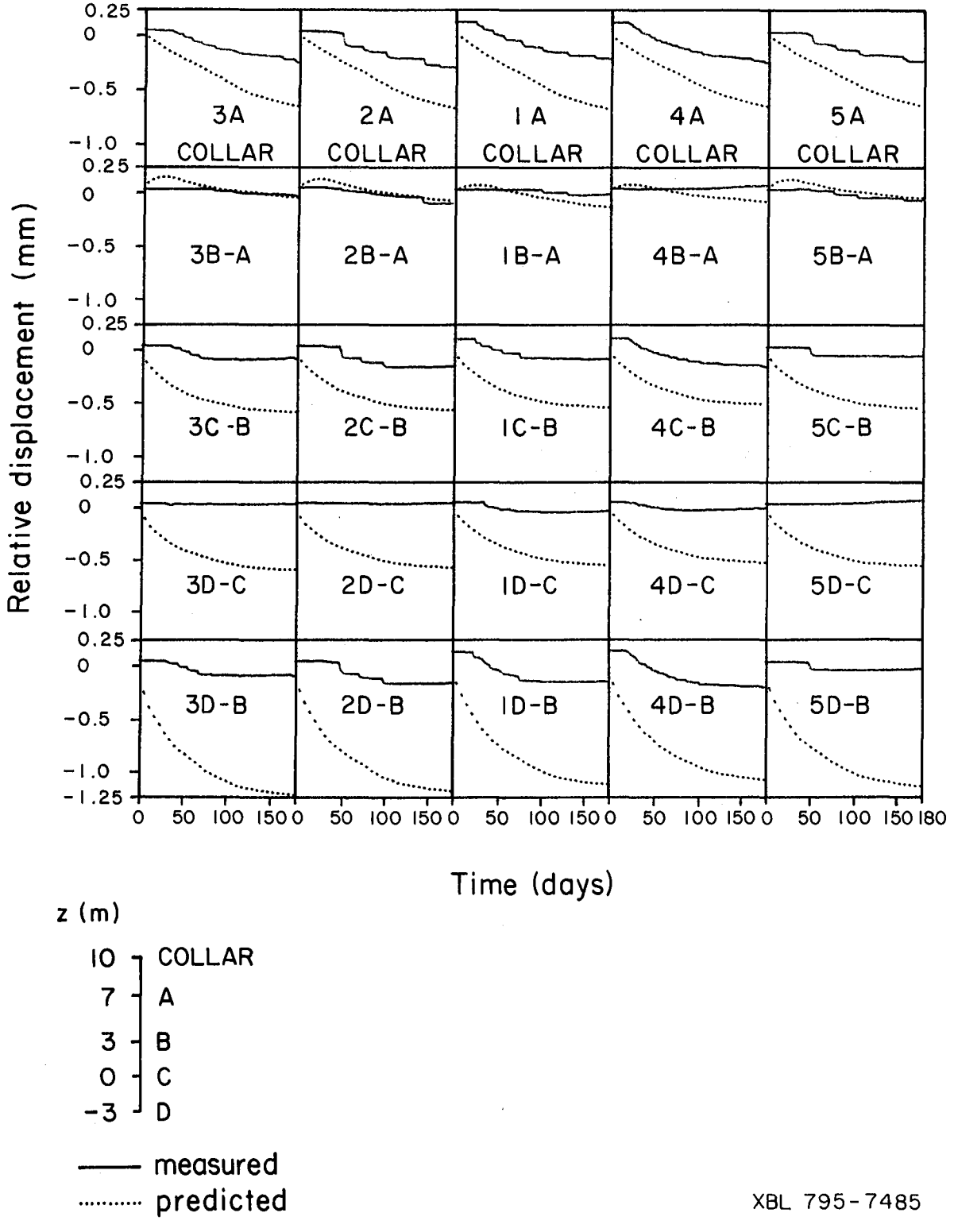

Fig. 29. Measured (solid) and predicted (dotted) relative displacement between various pairs of anchor points on each vertical extensometer in the time-scaled experiment, as a function of time. The time-scaled drift has been taken into account in this model. Inset shows the designation of the different anchor points. See Fig. 30 for layout of the extensometers.

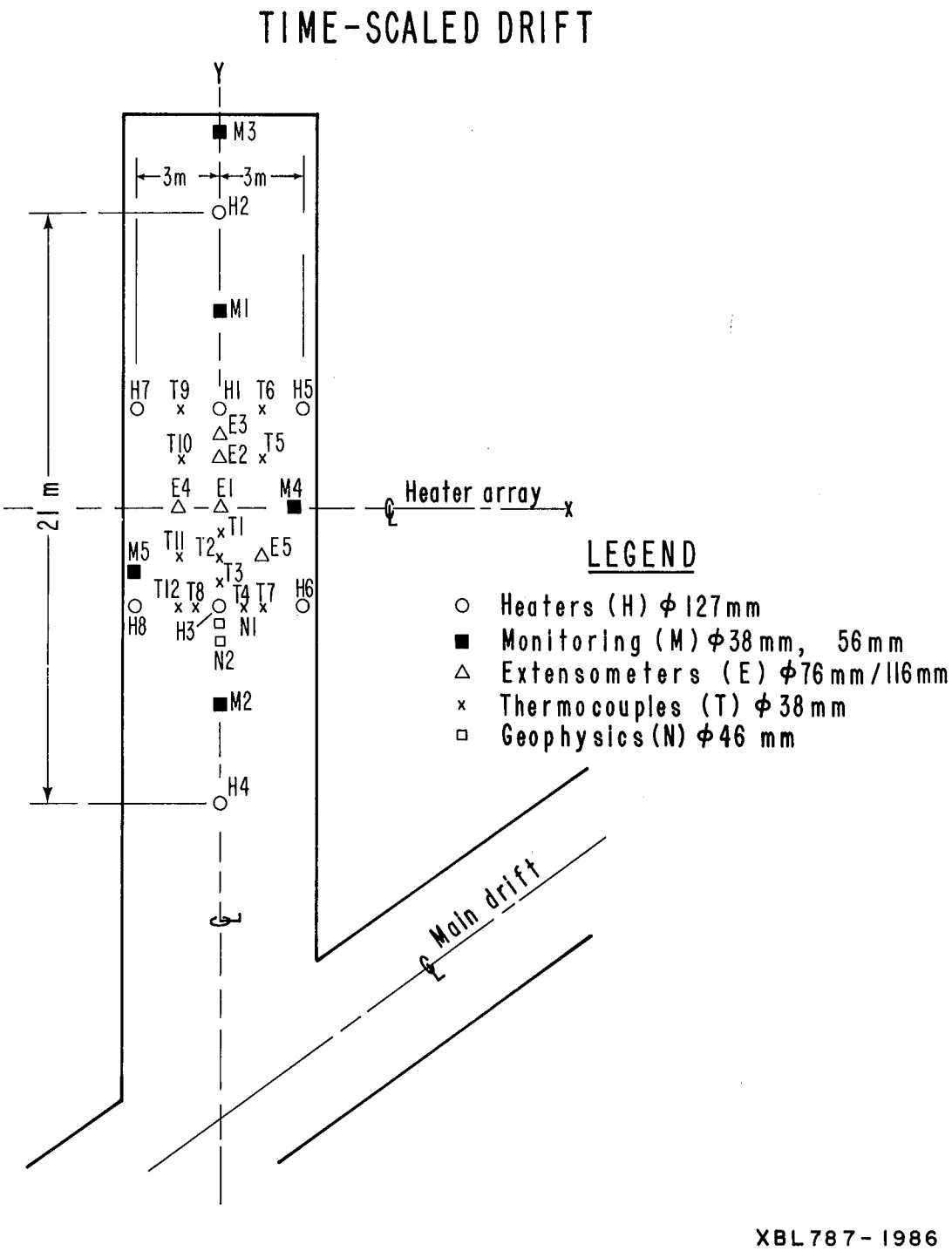

Fig. 30. Borehole layout in the time-scale drift (after Kurfurst et al., 1978).

are on the order of 0.5 mm except between the pair 3 m above and below the midplane (B and D) where values on the order of 1 mm are predicted. Because the power of the time-scaled heaters decays with time, whereas the full-scale heaters remain at constant power, it is no longer possible to compare the results of the Time-Scaled Experiment with those of the 3.6 kW Full-scale Experiment by scaling.

The model which takes into account the existence of the heater drift predicts a displacement at the floor of the drift (90 days after the heater is turned on) nearly 50% greater than the model that ignores the drift.

Another point to note is that since we have ignored the time-scaled heater holes by using a coarse mesh, the maximum compressive stresses which are expected to occur at the wall of the holes cannot be predicted by this model. As there are no stress measurements in this experiment, this is not too serious a drawback.

5. FURTHER MODELING WORK

As previously stated, the main purpose of the foregoing calculations is to provide a relatively simple framework for interpretation of field data. Preliminary comparisons with measured displacements and stresses (Cook and Hood, 1978) have already indicated that the actual thermomechanical response of the granite rock mass is more complicated than that assumed in the linear thermoelastic models presented in the preceding sections.

The approximations made in the present work fall into two categories:

1. Those related to the geometry of the model and the discretization of the model domain;

2. those related to the properties of the rock, i.e., treating the rock mass as a homogeneous, isotropic, linear elastic continuum with constant material properties.

5.1. Better approximation of geometry

The approximations in category (1) can be improved upon without introducing any basic difference in the analysis. In the full-scale experiments, the presence of the heater drift means that the midplane of the heater array is not strictly a plane of symmetry. Similarly, the presence of the extensometer drift on one side of the heaters makes the validity of the axisymmetric model questionable. A first step in refining the model is to discretize the half-plane (i.e., both the $z > 0$ and the $z < 0$ portions of the r - z plane) instead of just the quarter-plane. Proper inclusion of the geometry of the extensometer drift requires a three-dimensional model. Due to practical limitations, the use of a three-dimensional mesh would, in turn, require the introduction of other approximations, such as a coarser mesh and an outer boundary closer to the heaters than what we have hitherto been assuming. As a preliminary measure, the significance of the asymmetry due to the extensometer drift can be investigated, at least qualitatively, by means of plane-strain models in the midplane of the heaters.

Judging from the comparatively small discrepancies between the thermal stresses and relative radial displacements between close-in extensometer anchor points and the rather large disparities between the relative vertical displacements obtained by utilizing the two models M1 and M7, as presented in Section 4 (Tables 5 through 7), one can conclude that the influence of the heater drift is definitely more significant than the extensometer drift.

This is expected intuitively from a mere consideration of the distances of the drifts from the heaters. Accordingly, priority will be given to an investigation with an axisymmetric model that does not assume the heater midplane to be a plane of symmetry.

For the Time-Scaled Experiment, the thermal stress in the midplane can be calculated reasonably accurately by means of a fine mesh plane-strain model. Obviously this does not yield the vertical displacement which is the only quantity, other other than temperature, measured in this experiment. As an alternative, the analytic solution for a point source in a semi-infinite medium (Nowacki, 1962) can be superimposed to obtain an approximate solution in a manner similar to what St. John (1977) did for repository studies. Although this solution would necessarily leave out the effects of the heater holes and also cannot model the geometry of the time-scaled heater drift accurately, it may still provide a reasonable approximation for the vertical displacements at the location of the extensometers, since the latter are not very close to the heater holes.

A refined three-dimensional model, utilizing substructuring techniques to more fully discretize the region around each heater, can also be attempted. Alternatively, the axisymmetric model for the full-scale experiments can be scaled down to model one time-scaled heater, from which the total displacement and stress fields can be obtained by superposition, assuming linear thermoelasticity. Again, the geometry of the heater drift cannot be modeled very accurately.

5.2. Modeling for variable rock properties and discontinuities

The thermally induced displacements and stresses depend on the thermal, thermomechanical, and mechanical properties of the rock. Rocks, by virtue of their complex compositions and structures, are often heterogeneous, anisotropic, and nonlinear. Their properties are, in general, functions of temperature and time. Furthermore, in the case of hard rock sites, the in situ rock mass behavior is strongly influenced by the omnipresence of discontinuities. We shall consider the problems of (1) properly incorporating into the numerical models the nonideal behavior of rock as determined in conventional laboratory samples and (2) modeling for discontinuities.

5.2.1. Laboratory rock properties. We first address the issue of temperature dependence of rock properties. Tsui (1979) has recently made a rather comprehensive survey of published laboratory data on the thermal, thermomechanical, and mechanical properties of nonsaline rocks as a function of temperature. As expected, the degree of temperature dependence of rock properties varies from rock type to rock type and even within the same rock type. For granites in general, thermal conductivity and diffusivity, as well as Young's modulus, Poisson's ratio, and compressive strength, decrease with increasing temperature, whereas the thermal expansion coefficient increases at elevated temperatures.

Granite core samples taken from the Stripa site have been tested to a limited extent by Pratt et al. (1977) and Swan (1978). Except for the thermal expansion coefficient, the variation of Stripa granite properties with temperature follows the same general trend as for other granites, as mentioned above. The thermal expansion coefficient of Stripa granite has

been measured on only two core samples (Pratt et al, 1977). The laboratory data have been interpreted as implying a constant linear coefficient of thermal expansion in the 20-200°C temperature range. However, an examination of the data appears to indicate a slightly higher coefficient above 150°C than below this temperature. Evidently, additional laboratory measurements are badly needed.

A linear coefficient of thermal expansion that increases with tempera ture is qualitatively consistent with several observations concerning the ratio between the relative displacement measured in the in situ heater experiments at Stripa and the value predicted by linear thermoelastisc analysis using constant rock properties. For example, this ratio increases in the Full-Scale Experiment 2 after the peripheral heaters are turned on, which substantially increases the temperature in a rather large volume of rock. The accompanying increase in thermal expansion coefficient will lead to more rapid increase in displacement than that expected for a rock body with constant thermal expansion coefficient. Conversely, the ratio of displacements is smaller in the Time-Scaled Experiment in which the rock temperatures are generally lower. Of course, this remark is not meant to preclude other explanations, especially in the latter case where the tempera- ture dependence of the thermal expansion coefficient alone is unlikely to be able to account quantitatively for the large disparity between experiments.

When the thermal parameters vary with temperature, the heat transfer problem becomes nonlinear and must be solved numerically. Preliminary numerical results obtained using either the integrated finite difference code CCC (Lippmann et al., 1977) or the finite element code DOT (Polivka and

Wilson, 1976) indicated that the temperature dependence of 1% increase per 10°C in thermal conductivity and diffusivity as ,measured by Pratt et al. (1977) leads to about a 10-15% difference in the predicted temperatures around the 3.6 kW heater.

Temperature-dependent thermoelastic parameters present no basic difficulty in the finite element thermomechanical analysis. In essence, elements at different temperatures are assigned different material properties, as if they were composed of different materials. This capability already exists in the version of SAPIV that we have been using. Preliminary results show that using the temperature-dependent Young's modulus and Poisson's ratio, similar to those determined by Swan (1978) reduces the general level of displacements and stresses by approximately 20%, compared with the constant-property case. At the edge of the 5 kW heater, however, the stresses are reduced by a factor greater than two. A temperature-dependent thermal expansion coefficient would partially compensate for the effects of temperature-dependent elastic properties.

Based on the limited amount of tests conducted by Swan (1978), whatever nonlinearity or anisotropy that exists in Stripa granite appears to be insignificant, as far as intact samples are concerned. Likewise, time-dependent creep is not expected to be an issue in granites at temperatures up to 400°C and stress differences of a few hundred MPa. This conclusion can be inferred from the review by Heard (1976) of creep data on rocks ranging from marble through quartzite to dunite.

5.2.2. Discontinuities and heterogeneities. Four distinct sets of discontinuities (fractures) have been identified at the Stripa site (Thorpe, 1979). Mean fracture spacing is on the order of a fraction of a meter. Witherspoon et al. (1977) measured the stress-deformation characteristics of a diamond saw-cut and an artifically induced tension fracture across a granite specimen about 1 m in diameter and found them to be highly nonlinear. From this it can be inferred that the stress-deformation characteristics of a jointed rock mass are likely to be nonlinear and significantly more compliant than those of solid rock (Cook and Witherspoon, 1978). The bulk thermal expansion coefficient is is also expected to depart from the intact rock behavior in a similar manner.

The in situ Young's modulus measured at Stripa by Schrauf et al. (1979) using the CSM (Colorado School of Mines) gauge varies markedly from point to point and is positively correlated with fracture frequency. The Young's modulus has a mean value of 37 MPa, about two-thirds of the laboratory value used in the calculations presented in this report. However, one should bear in mind that each CSM gauge measurement only samples the elastic modulus of the rock within a few diameters of the 38 mm hole into which the gauge is inserted. Consequently, it it is not certain to what extent the measured values represent the rock mass property.

Closely spaced discontinuities can be modeled by the approach of an equivalent anisotropic continuum (Goodman, 1976). In fact, the combined effects of several joint sets with different orientations may result in a rock mass that is not too highly anisotropic. A laboratory test program is under way to determine the thermomechanical properties of specimens of core

taken from the "stress meter" or extensometer holes at Stripa. These tests will be done over a range of hydrostatic and deviatoric stresses and temperatures covering and exceeding those to which the rock has been subjected in the field. They will include specimens of intact and jointed rock. From these measurements, the equivalent rock mass properties will be deduced using the method of Goodman (1976) or other theories for effective elastic constants (Jaegar and Cook, 1976). The thermomechanical calculations will be repeated using these properties as input into a nonlinear finite element model utilizing codes, such as ADINA (Bathe, 1975).

For nonlinear modeling, it is also necessary to know the virgin state of stress. Hydrofracturing and other tests for the in situ state of stress should be performed at Stripa to obtain this vital information.

Recalculations using temperature-dependent and nonlinear material properties are expected to yield lower predicted displacements and stresses as well as nonlinear, time-dependent responses, in closer agreement with the field observations.

The reduction of thermal expansion coefficient and Young's modulus as well as the nonlinearity expected in a fractured rock mass has previously been observed to occur in highly cracked laboratory-size rock specimens, though on a much smaller scale. For example, Barbish and Gardner (1969) measured the Young's modulus of heated and unheated rock specimens and found that the specimen previously heat-treated to 750°C, and hence presumably containing numerous microcracks produced by differential thermal expansion of the various minerals of the rock, show a marked increase in Young's

modulus with axial stress--from 30% at zero stress to 70% of the value for the unheated specimen at 40 MPa. They have attributed the nonlinearity to crack closure. Likewise, Richter and Simmons (1974) observed that the thermal expansion of an igneous rock depends inversely on the microcrack porosity.

A limited number of fractures may have much wider apertures and/or weaker in-filling material so that they dominate the thermomechanical response and consequently the groundwater flow of the rock mass. In that case it is necessary to model discrete fractures. Finite element techniques are available for simulating the mechanical response of discrete fractures (Goodman et al., 1968; Goodman and DuBois, 1972) as well as the coupled effects of stress and fluid flow through fractures (Noorishad et al., 1971; Gale et al., 1974; Ayatollahi, 1978). Work is in progress to incorporate into an existing model the capability to simulate the thermomechanical response of rocks with deformable fractures (Ayatollahi et al., 1979, Noorishad, Witherspoon and Chan, work in progress).

As a first step, only one-way interactions will be modeled, i.e., the heat transfer determines the temperature distribution which gives rise to thermal stress and deformation, thereby changing the fracture aperture. Gale (1975), Iwai (1976), and Witherspoon, et al. (1977) observed experimentally that the permeability is proportioned to the square of the fracture aperture. If the field data indicate that thermal convection is not entirely negligible and/or that although the pressures generated by piezometric flow are small compared with the in situ stress at depth, the pressures generated by the restrained thermal expansion of water are high enough to deform the fractures

or cause hydrofracturing, then some degree of coupling will be introduced into the model. It is important to utilize the Stripa data to gain some fundamental understanding of how the thermomechanical perturbation impacts groundwater flow, since that is the major long-term issue in high-level (reprocessed or unreprocessed) nuclear waste disposal.

Due to the short duration of the Stripa heating experiments there may not be adequate data to facilitate a definitive assessment of the long-term thermal and thermomechanical effects on groundwater flow. This means that it is necessary to conduct heating experiments of longer duration specially designed to simultaneously observe both the thermomechanical and thermohydraulic responses in fractured rock. For the purpose of simulating long-term groundwater flow under the thermal and mechanical perturbations of a nuclear waste repository, it is essential to have a discrete joint model available. The main reason is that, although an equivalent continuum model may yield the correct flow rate it will definitely underestimate the velocity, i.e., overestimate the travel time for the radioactive nuclides. Accordingly, development of a discrete joint model for at least partially coupled thermohydraulic-thermomechanical analysis should be pursued with vigor.

In addition to the fracture sets, there are three pegmatite dikes in the heater test site. One of these traverses the area around the 3.6 kW heater.

In principle, heterogeneities in the form of spatially varying elastic moduli or pegmatites (provided their properties are known) present little difficulty in numerical modeling. In practice, of course, it is necessary

to examine the geological data very closely to delineate zones of differing properties. A high degree of heterogeneity may destroy whatever geometric symmetry there is in the system, thereby making three-dimensional models mandatory.

6. SUMMARY AND CONCLUSIONS

Thermomechanical analysis has been performed to predict in advance the displacement and stress fields associated with the two full-scale and one time-scaled heating experiments currently under way in granite 340 m below the surface at Stripa, Sweden. Temperatures calculated by means of the Green's function method were applied as thermal loads to a linear thermo-elastic finite element program SAPIV to calculate the displacements and stresses as functions of space and time. In order to provide a simple framework for interpreting field data, material properties for Stripa granite measured in conventional small-scale laboratory tests under room conditions were used. The predicted results have been stored in an on-site computer for real-time comparison with field data as they are collected.

Two-dimensional axisymmetric models were utilized for the full-scale experiments, and three-dimensional models for the time-scaled experiment. A total of three series of analyses were undertaken. Among these the latest series (Model Series 3), which is reported in this volume, assumes power histories closest to the actual situation.

The more important results can be summarized as follows:

Full-scale experiments

- Both thermally induced displacements and stresses rise very rapidly for the first 30 days after the heaters are turned on. Thereafter, the rate of increase becomes more gradual, so that after about 100 days, depending on location, nearly asymptotic values are approached.

- Maximum radial displacements are predicted to be 0.6 mm for the 3.6 kW experiment, 0.8 mm for the 5 kW experiment without the peripheral heaters and about 2.0 mm after the latter have been turned on.

- Maximum vertical displacements are predicted to be 1.4 mm and 2.0 mm, respectively, for the full-scale heaters. After the peripheral heaters have been turned on in the 5 kW experiment, vertical displacement at the floor of the heater drift reaches a maximum value of 4 mm.

- Maximum relative displacements between extensometer anchor points are also expected to have values comparable to those quoted above.

- The heater drift, which is 4.25 m above the midplane of the heaters has significant influence on both the displacements and stresses even relatively early in the experiment, e.g., 30 days after the central heater has been turned on, whereas the extensometer drift, a horizontal distance 10 m from the axis of the central heater, has an effect only at longer times.

- Highest compressive axial and tangential thermomechanical stresses occur at the rock edge of the central heater hole. For the 3.6 kW heater, the

maximum compressive tangential stress is 150 MPa. For the 5 kW experiment, the maximum values are 215 MPa and 320 MPa, respectively, with and without the peripheral heaters. These stresses are, respectively, slightly below, approximately equal to, and greater than the unconfined compressive strength of Stripa granite. Consequently, thermomechanical failure of the heater hole is expected in the higher-power experiment, but not in the other.

Three zones of tensile stresses can be identified. In the first few days after turn-on, there is a shell of tensile tangential and axial stresses just outside the high-temperature zone around the heater hole extending from about 0.5 m to 2 m. The largest magnitude of the tensile tangential stress is around 2 MPa. This zone spreads out with increasing time and becomes insignificant in magnitude. The second zone is beneath the floor of the heater drift where the tangential and radial stresses are tensile shortly after the central heater is turned on and persists throughout the heating period, reaching values of -10 MPa and -20 MPa before and after the peripheral heaters are turned on in the 5 kW experiment. These stresses are comparable in magnitude to the preliminary values of in situ stresses as well as to the unconfined tensile strength of intact Stripa granite. It is suggested that an attempt be made to measure the change of aperture of one or more fractures along the floor of the heater drift. A third tensile zone occurs near the wall of the extensometer drift at later times. A maximum magnitude of around 3 MPa is obtained.

Time-scaled Experiment

- Predicted maximum relative displacements between anchor points are mostly around 0.5 mm.

- Analysis based on an idealized closed form solution (Appendix B) reveals that although temperature, stress, and strain all scale according to the same law of similitude, displacement scales differently.

- Consideration of physical properties of granite indicates that the thermal and thermomechanical properties of a jointed granite rock mass are likely to be nonlinear and temperature-dependent.

The numerical results of limited thermomechanical modeling indicate that the temperature dependence of the elastic properties affects the predicted displacements and stresses appreciably, especially near the heater hole. It is, therefore, recommended that the thermal and thermomechanical properties be measured in the laboratory for both intact and jointed core specimens taken from the instrument holes at the Stripa site over the range of temperatures and stresses encountered during the heating experiments. The resulting nonlinear and temperature-dependent properties should then be used in refined nonlinear thermomechanical models utilizing:

1) existing nonlinear continuum finite element code(s), and
2) an existing discrete finite element joint model currently being modified to incorporate the capability for handling thermomechanical response.

In view of the possibility that a limited number of singular fractures may dominate the thermomechanical and thereby the thermohydraulic response of

a low permeability rock mass in which the radioactive waste repository is situated, it is necessary to extend an existing coupled stress-fluid flow finite element code with discrete joint element to model coupled thermal, stress, and fluid flow in a jointed rock mass. Considering the inability of equivalent-medium continuum models to predict, within reasonable error bounds, the travel time of radionuclides in dominant fractures and the enormous impact of this on the ultimate question of long-term safety in nuclear waste disposal, it is recommended that research and development of a discrete joint model for coupled thermal, stress, and fluid flow should proceed in parallel with the in situ heating experiments and application of existing continuum models alluded to in the preceding paragraph. Part of this development work is already in progress.

7. ACKNOWLEDGEMENTS

The authors would like to thank N. Littlestone, J. S. Remer, and O. Wan for their assistance in programming. They are also indebted to J. Kuo for his meticulous construction of the finite element meshes, and J. A. Jeffry and S. Peterson for programming and verifying some of the equations in the appendices.

8. REFERENCES

American Physical Society, 1978. "Report to the A.P.S. by the Study Group on Nuclear Fuel Cycles and Waste Management." Rev. Mod. Phys., 50, 55-5185.

Ayatollahi, M. S.. 1978. Stress and flow in fractured porous media. Ph.D. Thesis, Department of Materials Science and Mineral Engineering, University of California, Berkeley.

Ayatollahi, M. S., Chan, T., and Witherspoon, P. A. 1979. A numerical method for analysis of the thermoelastic behavior of saturated fractured rocks (abst.). Second International Confernce on Computational Methods in Nonlinear Mechanics (TICOM) Abstract Proceedings, p. 241. Austin, Texas, March 26-3, 1979.

Barbish, A. B. and Gardner, G. H. F. 1969. "The effect of heat on some mechanical properties of igneous rocks." Proc. 4th Drilling and Rock Mech. Conf., Austin, Texas.

Bathe, K. J., Wilson, E. L., and Peterson, F. E. 1974. SAPIV, a structural analysis program for static and dynamic response of linear system. College of Engineering, University of California, Berkeley, Report EERC 73-11, June, 1973, Rev. April.

Bathe, K. J. 1975. "ADINA - a finite element program for automatic dynamic incremental nonlinear analysis." Report 82448-1, Acoustics and Vibration Laboratory, Department of Mechanical Engineering, Massachusetts Institute of Technology, Cambridge, Mass.

Carlsson, H. 1978. "A pilot heater test in the Stripa granite." Lawrence Berkeley Laboratory report LBL-7086, SAC-06. Berkeley, California.

Carlsson, H. 1978b. Stress measurement in the Stripa granite. Lawrence Berkeley Laboratory report LBL-7078. Berkeley, California.

Chan, T., Cook, N. G. W., and Tsang, C. F. 1977. "Modeling of underground heater experiments simulating high-level radioactive waste repositories in hard rock." pp. 159-163, Earth Sciences Division Annual Report, Lawrence Berkeley Laboratory report LBL-7028. Berkeley, California.

Chan, T., Cook, N. G. W., and Tsang, C. F., 1978. Theoretical temperature field for the Stripa heater project. Lawrence Berkeley Laboratory report LBL-7082. University of California, Berkeley.

Chan, T., Carlsson, H., and Jeffry, J. A. 1979. Comparison between theoretical and experimental cool-down temperatures for the Stripa pilot heater test. Lawrence Berkeley Laboratory report LBL-9944 (in preparation). University of California, Berkeley, California.

Cook, N. G. W. and Hood, M. 1978. Full-scale and time-scale heating experiments at Stripa: preliminary results." Lawrence Berkeley Laboratory report LBL-7072, SAC-22. University of California, Berkeley, California.

Cook, N.G.W. and Witherspoon, P. A. 1978. "In situ heating experiments in hard rock: their objectives and design." Presented at seminar on in situ heating experiments in geological formations. Stripa, Sweden, September 12-15. Lasrence Berkeley Laboratory report LBL-7073, SAC-10, Part II.

Gale, J. E. 1975. A numerical, field and laboratory study of flow in rocks with deformable fractures. Ph.D. Thesis University of California at Berkeley, 250 pp. (Also published as Scientific Series No. 72, Inland Waters Directorate, Environment Canada, Ottawa, Canada, 1977.)

Gale, J. E., Taylor, R. L. Witherspoon, P. A., and Ayatollahi, M. S., 1974. "Flow in rocks with deformable fractures." In Proc. Int. symposium on finite element methods in flow problems. Swansea, United Kingdom, Huntsville, Alabama: University of Alabama at Huntsville Press.

Goodman, R. E., 1976. Methods of Geological Engineering in Discontinuous Rocks. St. Paul, Minnesota: West Publishing Co.

Goodman, R. E., Taylor, R. L., and Brekke, T. L. 1968. "A model for the mechanics of jointed rocks." J. Soil Mech. and Found. Division, ASCE, 94, N.S.M.3.

Goodman, R. E. and Dubois, J. 1972. "Duplication of dilatancy in analysis of jointed rocks." Soil Mech. and Found. Division, ASCE, 93, 399.

Heard, H. C. 1976. "Comparison of the flow properties of rocks at crustal conditions." Phil. Trans. R. Soc. London. A 283, 173-186.

Hood, M. 1979. "Some results from a field investigation of thermomechanical loading of a rock mass when heater canisters are emplaced in the rock." Proc. 20th U. S. Symposium on Rock Mechanics, Austin, Texas. June, pp. 429-437.

Iwai, K. 1976. "Fundamental studies of fluid flow through a single fracture." Ph.D. Thesis, Dept. of Civil Eng., University of California, Berkeley.

Jaeger, J. C. and Cook, N. G. W. 1976. Fundamentals of Rock Mechanics. 2nd ed., London: Chapman and Hall; New York: John Wiley and Sons, Inc.

Kisner, R. A., Marshall, J. R., Turner, D. W., and Vath, J. E. 1977. Nuclear waste projections and source-term data for FY 1977. Y/OWI/TM-34, Office of Waste Isolation, Oak Ridge, Tennessee. April.

Kurfurst, P. J., Hugo-Persson, T., and Rudolph, G. 1978. "Borehole drilling and related activities at the Stripa mine." Lawrence Berkeley Laboratory report LBL-7080, SAC-05. Berkeley, California.

Lippmann, J. M., Tsang, C. F., and Witherspoon, P. A. 1977. "Analysis of the response of geothermal reservoirs under injection and production procedures." Paper SPE 6537, 47th annual California regional meeting, Soc. of Pet. Eng. of AIME. Bakersfield, California. April 13-15.

Llewellyn, G. H. 1978. Prediction of temperature increases in a salt repository expected from the storage of spent fuel or high-level waste. ORNL/ENG/TM-7, Oak Ridge, April.

McElroy, M. B., 1979. Data acquisition, handling and display for the heater experiments at Stripa. Lawrence Berkeley Laboratory report LBL-7062, SAC-14. Berkeley, California.

Noorishad, J., Witherspoon, P. A., and Brekke, T. L. 1971. "A method of coupled stress and flow analysis of fractured rock mass." Publication No. 71-6, Dept. of Civil Eng., University of California, Berkeley.

Nowacki, W. 1962. Thermoelasticity. Pergammon Press, Oxford.

Paulsson, B. 1979. "Characterization of discontinuities in the Stripa granite--full-scale heater expriment." Lawrence Berkeley Laboratory report LBL-9063 (in preparation). University of California, Berkeley.

Polivka, R. M. and Wilson, E. L. 1976. Finite element analysis of nonlinear heat transfer problems. UCSESM 76-2, Dept. of Civil Eng., Univ. of California, Berkeley. June.

Pratt, H. R., Schrauf, T. A., Bills, L. A., and Hustrulid, W. A. 1977. Thermal and mechanical properties of granite: Stripa, Sweden. Summary report TR-77-92, TerraTek. Salt Lake City, Utah.

Richter, D. and Simmons, G. 1974. "Thermal expansion behavior of igneous rocks." IJRMMS, vol. 11, 403-411.

Sackett, S. 1978. "New version of SAPIV." Unpublished memorandum, MDG 78-14. Lawrence Livermore Laboratory, Livermore. February.

Schrauf, T. W., Pratt, H. R., Hustrulid, W. A., and Simonson, E. R. 1979. Instrumentation evaluation, calibration and installation for heater tests simulating nuclear waste in crystalline rock, Sweden. Lawrence Berkeley Laboratory report LBL-8313 (in preparation.)

St. John, C. M. 1977. Thermoelastic analysis of spent fuel high-level radioactive waste repositories in salt--a semi-analytical solution. ORNL-SUB-7118. Oak Ridge, Tennessee.

Swan, G., 1978. "The mechanical properties of Stripa granite." Lawrence Berkeley Laboratory report LBL-7074, SAC-03. Berkeley, California.

Thorpe, R. 1979. Characterization of discontinuities in the Stripa granite time-scaled heater experiment. Lawrence Berkeley Laboratory report LBL-7083, SAC-20. Berkeley, California.

Timoshenko, S. P. and Goodier, J. N. 1951. Theory of Elasticity. 2nd ed. New York: McGraw Hill.

Tsui, K. K. 1979. A study of the thermomechanical stability of rock caverns Ontario Hydro Design and Development Division report no. 78239. Toronto, Ontario, Canada.

Witherspoon, P. A., Amick, C. H., and Gale, J. E. 1977. Stress-flow behavior of a fault zone with fluid injection and withdrawal. Univ. of California Berkeley Mineral Engineering Report 77-1, 159 pp.

Witherspoon, P. A. and Degerman, O. 1978. Swedish-American Cooperative Program on radioactive waste storage in mined caverns - program summary. Lawrence Berkeley Laboratory report LBL 7049, SAC-01, Berkeley, California.

Additional laboratory results for material properties of Stripa granite have now become available and the calculations have been updated. The interested reader is referred to the following papers:

Chan, T., Hood, M., and Board, M. 1980. "Rock Properties and Their Effect on Thermally Induced Displacements and Stresses," presented at the 1980 ASME Energy Technology Conference and Exhibition, New Orleans, Louisiana, February; and submitted for publication to ASME J. Energy Resources Tech.

Chan, T., Littlestone, N., and Wan, O. 1980. "Thermomechanical Modeling and Data Analysis for Heating Experiments at Stripa, Sweden," to be presented at 21st U.S. Rock Mechanics Symp., Rolla, Missouri, May.

Witherspoon, P.A., Chan, T., and Hood, M. 1980. "Predicted and Measured Temperatures, Displacement and Stresses from the Stripa Heater Experiments," to be presented at ROCKSTORE 80, Interm. Symp. on Subsurface Space for Envir. Prot., Low-Cost Storage and Energy Savings, Stockholm, Sweden, June.

APPENDIX A

MODEL TESTING

Before the finite-element model for the full-scale experiments was used for production runs, it was tested to ensure that (1) the discretization scheme (mesh) was sufficiently fine and (2) the external boundaries were sufficiently remote that they would not lead to spurious results. Testing for mesh fineness was accomplished by comparison with the analytic solution for an infinitely long hollow cylinder subjected to the same thermal load as that imposed by the heater on the surrounding rock. Boundary condition checking was done by comparing the thermally induced displacements and stresses obtained by applying two different boundary conditions to the same finite-element mesh.

A.1. COMPARISON WITH ANALYTIC SOLUTION

The purpose of this comparison is not to verify the finite-element code by showing that the finite-element solution for an infinite cylinder agrees with the analytic solution. While the correctness of the computer code is certainly a necessary condition for its meaningful application to model the physical problem, that by itself is not sufficient to ensure that the finite-element model, which takes into account the finite lengths of the heaters in the Stripa experiments, would be a good approximation. Instead, we want to see whether the finite-element model to be used for the full-scale experiments (Fig. 4, Section 3) agrees with the analytic solution for the infinite hollow cylinder in the regime where the latter is expected to be a reasonable approximation to the geometry of the heater experiment.

Formulae for the radial displacement u_r and the radial, tangential, and axial stresses, σ_r, σ_θ, and σ_z may be derived from those quoted by Timoshenko and Goodier (1951) for an infinitely long hollow cylinder with an internal radius, a, and an external radius b subjected to a radial temperature distribution T(r):

$$u_r = \frac{1+\nu}{1-\nu}\left[\frac{\alpha}{r}\,\frac{(1-2\nu)r^2+a^2}{b^2-a^2}\int_a^b T(r)rdr + \int_a^r T(r)rdr\right] \qquad (A1)$$

with displacement away from the axis being treated as positive.

$$\sigma_r = \frac{\alpha E}{1-\nu}\,\frac{1}{r^2}\left[\int_a^r T(r)rdr - \frac{r^2-a^2}{b^2-a^2}\int_a^b T(r)rdr\right] \qquad (A2)$$

$$\sigma_\theta = \frac{\alpha E}{1-\nu}\,\frac{1}{r^2}\left[T(r)r^2 - \int_a^r T(r)rdr - \frac{r^2+a^2}{b^2-a^2}\int_a^b T(r)rdr\right] \qquad (A3)$$

$$\sigma_z = \frac{\alpha E}{1-\nu}\left[T(r) - \frac{2\nu}{b^2-a^2}\int_a^b T(r)rdr\right], \qquad (A4)$$

with compressive stress being taken as positive. In the above equations the symbols α, ν, and E have their usual meaning as defined in Section 3.

For the case of a borehole in an infinite medium, take limits of the expressions in (A1) to (A4) as $b \to \infty$. Since T is a decreasing function of r,

$$\lim_{b\to\infty} \frac{1}{b^2-a^2}\int_a^b T(r)rdr = 0$$

so that equations (A1) to (A4) reduce to

$$u_r = \frac{1+\nu}{1-\nu}\,\alpha\bar{T}r \qquad (A5)$$

$$\sigma_r = \frac{\alpha E}{1-\nu}\,\bar{T} \qquad (A6)$$

$$\sigma_\theta = \frac{\alpha E}{1 - \nu} (T - \overline{T}) \tag{A7}$$

$$\sigma_z = \frac{\alpha E T}{1 - \nu} \tag{A8}$$

where

$$\overline{T}(r) = \frac{1}{r^2} \int_a^r T(r) r dr. \tag{A9}$$

Equation (A1) to (A4) or (A5) to (A8) have been utilized by various authors in their studies of nuclear waste storage (Cook, 1978; Leijon, 1978) or compressed air storage (Howells, 1977).

For the present application we are interested in the change in displacements and stresses induced by the temperature rise ΔT in the rock due to a constant power cylindrical heater of finite length. It has been shown (Chan Cook, and Tsang, 1978)[11] that an excellent approximation to the actual problem is given by the solution for a finite line source.

$$\Delta T(r, z, t) = \frac{Q_\ell}{4\pi k} \int_{-b}^{b} \frac{\operatorname{erfc}\left[\left(\frac{r2 + (z - z')2}{4\kappa t}\right)\right]^{1/2}}{\left[r^2 + (z - z')^2\right]^{1/2}} dz' \tag{A10}$$

where

Q_ℓ = thermal power per unit length of the heater

k = thermal conductivity

κ = thermal diffusivity

r, z = coordinates in a cylindrical system with origin at the center of the heater

t = time.

---

[11]There is a typographical error in equation 13 of that reference. The correct expression is given by (A10) here.

The temperature rise $_{\Delta}T$ given by (A10) is a function of both r and z because of the finite length of the heat source. However, for a short period after the heater is activated, the high-temperature isotherms all lie within small radial distances from the axis of the heater (see Fig. 51, Chan, Cook, and Tsang, 1978). When both r and t are small, it can be shown that the solutions for the finite and infinite line sources coincide (Chan and Remer, 1978; Jeffry et al., 1979).

The expressions (A5) to (A9) have been evaluated by substituting $_{\Delta}T(r, o, t)$ from (A10) in place of T(r) in (A9). This gives the curves labeled analytic solution for σ_θ and σ_z in Fig. 10, Section 4. For the finite element solution $_{\Delta}T$ from equation (A10) is evaluated and input as nodal point temperatures, to the mesh M1 illustrated in Fig. 4, Section 3.

As discussed in Section 4, there is excellent agreement between the finite element and analytic solutions at short time, as expected. Since the temperature gradient and hence the stress gradient is steepest at short time, it can be concluded that the mesh is fine enough. Incidentally, the agreement also validates (in a restricted sense) the finite-element program.

A.2. Boundary condition checking

In the finite-element models used to obtain the displacements and stresses presented in this report for the full-scale experiments, zero normal-displacement (roller) boundary conditions were applied to the outer horizontal and vertical boundaries of the model block. To confirm that these outer boundaries (at distances of 100 m from the center of the main heater) were sufficiently remote from the high-temperature region, we carried out a separate analysis using alternate boundary-loading conditions.

The alternative analysis for comparison was carried out in the following manner. First, a finite element analysis was performed by applying assumed horizontal and vertical virgin stresses (both taken as equal to the overburden weight) to the appropriate outer boundaries of the model with the drifts excavated (i.e., Mesh 7). In addition, gravity was applied as a body force to each element. This yielded the mechanical displacements, u_i^{mech}, and stresses, σ_{ij}^{mech},

$$u_i^{mech} = u_i^{vir} + u_i^{exc}, \qquad i = 1, 2, 3 \tag{A11}$$

$$\sigma_{ij}^{mech} = \sigma_{ij}^{vir} + \sigma_{ij}^{exc}, \qquad i, j = 1, 2, 3 \tag{A12}$$

where u_i^{vir} = displacement (spurious) in the rock continuum caused by applying the virgin stresses as boundary loads and gravity,

u_i^{exc} = displacement induced by excavations

σ_{ij}^{vir} = stress in the rock continuum caused by applying the virgin stresses as boundary loads and gravity

σ_{ij}^{exc} = stress induced by excavations

Next a second run was made with thermal loading added. The total displacement, u_i^{tot}, and total stress, σ_{ij}^{tot}, would be

$$u_i^{tot} = u_i^{vir} + u_i^{exc} + u_i^{th} \tag{A13}$$

$$\sigma_{ij}^{tot} = \sigma_{ij}^{vir} + \sigma_{ij}^{exc} + \sigma_{ij}^{th} \tag{A14}$$

Hence, the thermally induced displacements and stresses are obtained by taking the differences

$$u_i^{th} = u_i^{tot} - u_i^{mech} \tag{A15}$$

$$\sigma_{ij}^{th} = \sigma_{ij}^{tot} - \sigma_{ij}^{mech} \tag{A16}$$

Table A1. Comparison of finite element solutions for Full-Scale Experiment 2, 730 days after turn-on using two different sets of boundary conditions

(a) Stress

r(m)	σ_r(MPa)		σ_z(MPa)		σ_θ(MPa)	
	BC1	BC2	BC1	BC2	BC1	BC2
0.2265	44.79	44.77	273.43	273.40	480.60	480.50
0.3	125.08	125.04	264.50	264.46	360.90	360.90
0.6	191.49	191.43	204.90	204.85	215.60	215.60
1.0	182.60	182.53	165.70	165.60	162.11	162.00
2.0	121.84	121.77	70.20	70.10	69.10	69.10
4.0	52.68	52.65	30.60	30.50	20.80	20.80
9.25	5.15	5.14	2.79	2.89	-12.33	-12.36
19.0	2.32	2.28	0.32	0.23	1.15	1.06
42.0	0.63	0.54	-0.29	-0.38	-0.25	-0.34

(b) Radial displacement

r(m)	u_r (mm)	
	BC1	BC2
0.203	-0.50	-0.50
0.25	-0.13	-0.13
0.35	0.43	0.43
0.55	1.15	1.15
0.95	2.11	2.11
2.125	3.05	3.05
4.75	3.52	3.52
10.0	4.08	4.08
14.0	0.59	0.61
24.0	0.72	0.73
46.0	0.20	0.24
56.0	0.13	0.17

Note:

(1) The numerical results given here are for Model Series 1 (i.e., using material properties 1 in Table 3) and are, therefore, not applicable to Stripa.

(2) All points are on heater midplane, i.e., z = 0.

(3) BC1 = zero normal displacement boundary condition
BC2 = virgin state of stress applied as boundary loading with gravity as body force.

(4) Mesh 7 used, i.e., drifts modeled.

As shown in Table A1, the results were found to be in close agreement with those obtained using zero normal-displacement boundary conditions.

Note that the material properties used in obtaining the numerical results in Table A1 are not Stripa granite properties. The sole purpose of this table is to demonstrate the absence of spurious boundary effects. The numerical values should not be used for comparison with experimental results from the Stripa heater project.

A.3. References

Chan, T., Cook, N. G. W., and Tsang C. F. 1978. "Theoretical temperature field for the Stripa heater project." Lawrence Berkeley Laboratory report LBL-7082. Berkeley, California.

Chan, T. and Remer, J. S. 1978. "Preliminary thermal and thermomechanical modeling for Near Surface Test Facility Heater Experiment at Hanford." Lawrence Berkeley Laboratory report LBL-7069. Berkeley, California.

Cook, N. G. W. 1978. "Mechanical and thermal design considerations for radioactive waste repositories in hard rock, part I: an appraisal of hard rock for potential underground repositories of radioactive wastes." Lawrence Berkeley Laboratory report LBL-7073, SAC-10. Berkeley, California.

Howells, D. A. 1977. "Effects of pressure and temperature changes in a compressed air storage cavern." Rockstore 77, Stockholm, Sweden. Sept.

Jeffry, J., Chan, T., Cook, N., and Witherspoon, P. 1979. "Determination of the in situ thermal properties of Stripa granite from temperature measurements in the full-scale heater experiments, I., Method and preliminary results." Lawrence Berkeley Laboratory report LBL-8423, SAC-24. Berkeley, California.

Leijon, B. 1978. "Predicted rock stresses for the Pilot Heater Test at Stripa Mine." Lawrence Berkeley Laboratory report LBL-7086, SAC-06. Appendix II, by Carlsson, H. Berkeley, California, August.

Timoshenko, S. P. and Goodier, J. N. 1951. Theory of Elasticity, 2nd. New York: McGraw Hill

APPENDIX B

SCALING LAWS FOR DISPLACEMENT AND STRESS

As explained by Cook and Witherspoon (1978) and demonstrated numerically by Chan et al. (1978), the concept of the time-scaled experiment is based on the law of similitude for linear conduction which states that the temperature fields caused by a scaled-down heater is related to that for a full-scale heater as

$$\Delta T^s(\vec{r}/L,\ t/L^2) = \Delta T^f(\vec{r},\ t) \tag{B1}$$

where

ΔT = temperature change

$\vec{r}$ = position vector

t = time

$L = \ell^f/\ell^s$ = scale factor for linear dimension

with ℓ being a characteristic length of the heat source and the superscripts f and s designating the full-scale and scaled-down systems, respectively. The purpose of this appendix is to examine scaling laws for the displacement and stress fields.

Inserting (B1) into equation (A9) of Appendix A we have

$$\Delta \bar{T}^s(r/L,\ t/L^2) = \frac{1}{r^2/L^2} \int_{a/L}^{r/L} \Delta T^s(r',\ t/L^2)\, r'dr'$$

$$= \frac{L^2}{r^2} \int_{a/L}^{r/L} \Delta T^f(r'L,\ t)\, r'dr'$$

Changing the dummy variable of integration from r' to R = r'L yields

$$\Delta\bar{T}^{s}(r/L,\ t/L^2) = \frac{L^2}{r^2}\ \frac{1}{L^2}\int_a^r \Delta T^{f}(R,\ t)RdR$$

or

$$\Delta\bar{T}^{s}(r/L,\ t/L^2) = \Delta T^{f}(r,\ t). \tag{B2}$$

This is, of course, expected since $\bar{T}$ is a "mean" temperature with the same dimension as T itself.

Substitution of (B2) into equation (A5) to (A8) then gives

$$u_r(r/L,\ t/L^2) = u_r^f/L \tag{B3}$$

$$\sigma_r^s(r/L,\ t/L^2) = \sigma_r^f(r,\ t)$$

$$\sigma_\theta^s(r/L,\ t/L^2) = \sigma_\theta^f(r,\ t) \tag{B4}$$

$$\sigma_z(r/L,\ t/L^2) = \sigma_z^f(r,\ t)$$

Although these scaling laws have been derived explicitly here for the case of infinitely long cylinders with the ratio of radii as the scale factor, it can easily be shown that, in general, the scaling laws

$$u_i^s(\vec{r}/L,\ t/L^2) = u_i^f(\vec{r},\ t)/L \tag{B5}$$

$$\sigma_{ij}^s(\vec{r}/L,\ t/L^2) = \sigma_{ij}^f(\vec{r},\ t) \tag{B6}$$

hold for heat sources of arbitrary shapes provided that the shapes of the heat sources are similar.

The important point to note here is that although the temperature, strain, and stress fields all scale similarly, the displacement field does not. Thus, for instance, in the case of the Stripa Time-scaled Experiment where the scale factor is 3.2, the displacement at a distance of 1 m from the center of the time-scaled heater (if only one single scaled heater with constant power output were used) one day after it was turned on would not be equal to the displacement at 3.2 m from the center of the full-scale (3.6 kW) heater 10.24 days since it was turned on, but would be smaller by a factor of 3.2 instead.

B. 1. References

Chan, T., Cook, N. G. W., and Tsang, C. F. 1978. Theoretical temperature field for the Stripa heater project. Lawrence Berkeley Laboratory report LBL-7082. Berkeley, California.

Cook, N. G. W. and Witherspoon, P. A. 1978. "In situ heating experiments in hard rock: their objective and design." Presented at seminar on in situ heating experiments in geological formations, Stripa, Sweden. September 12-15.

_____ 1978. "Mechanical and thermal design considerations for radioactive waste repositories in hard rock, Part I: an appraisal of hard rock for potential underground repositories of radioactive wastes." Lawrence Berkeley Laboratory report LBL-7073, SAC-10. Berkeley, California.

APPENDIX C

A NOTE ON THE COMPARISON OF PREDICTED THERMAL STRESS WITH USBM GAUGE MEASUREMENTS

C.1. INTRODUCTION

To compare the USBM gauge measurements with theoretical predictions from numerical models, two different types of plots, viz, (1) thermally induced stresses, and (2) borehole displacements, have been produced using the CDC-7600 computer at LBL. This note explains the theoretical basis behind these two types of plots and the difference between them. A rough estimate is made of the possible error introduced by the biaxial strain assumption used in calculating the stresses from the measured borehole displacements. Reference is also made to the MODCOMP plots produced at Stripa.

Numerical modeling gives the thermally induced stress at a point in the rock assuming that the instrument boreholes do not exist. However, a USBM gauge measures the displacements (changes in the diameter of a borehole) in three different directions 60° apart. Thus the computed and measured quantities are not directly comparable.

To effect the comparison one can either (1) invert the measured borehole displacements to obtain the actual thermal stresses which could prevail in the rock if the USBM borehole did not exist, or (2) calculate the borehole displacements from the predicted thermal stresses. Assuming that (1) the rock is a homogeneous isotropic, linear elastic medium, and (2) the thermally induced stress is uniform within a few diameters of the borehole, the well-

known Kirsch solution in the classical theory of elasticity can be applied to this problem (see, e.g., Obert and Duvall, 1967 or Jaeger and Cook, 1976).

C.2. STRESS PLOTS

Alternative (1) stated above has been adopted for the USBM stress plots on the MODCOMP IV computer at Stripa. As a first approximation it has further been assumed that a biaxial state of strain exists (Schrauf et al., 1979). The relevant equation is then

$$u = \frac{d(1 - \nu^2)}{E}[(S_p + S_q) + 2(S_p - S_q)\cos 2\theta_p] \qquad (C1)$$

where

d = borehole diameter

u = displacement (change in diameter)

S_p, S_q = maximum and minimum subsidiary principal stresses

θ_p = angle between the directions of u and S_p

E = Young's modulus (of the rock)

ν = Poisson's ratio (of the rock)

Knowing the three displacements u_1 (at angle θ_p), u_2 (at the angle $\theta_p + 60°$) and u_3 (at angle $\theta_p + 120°$), the system of equations is readily solved for the three unknowns, S_p, S_q, and θ_p. The results are

$$S_p = \frac{E}{6d(1 - \nu^2)}(u_1 + u_2 + u_3 + h) \qquad (C2)$$

$$S_q = \frac{E}{6d(1 - \nu^2)}(u_1 + u_2 + u_3 - h) \qquad (C3)$$

$$\theta_p = \frac{1}{2}\tan^{-1}\frac{\sqrt{3}(u_3 - u_2)}{2u_1 - u_2 - u_3} \qquad (C4)$$

where

$$h = \frac{1}{\sqrt{2}}\left[(u_1 - u_2)^2 + (u_2 - u_3)^2 + (u_3 - u_1)^2\right]^{1/2} \qquad (C5)$$

In the MODCOMP plots yet another approximation has been made, i.e., for gauges in vertical boreholes, S_p and S_q are identified with σ_r and σ_θ, respectively, while for gauges in horizontal boreholes, S_p and S_q are identified with σ_z and σ_θ. Here σ_r, σ_θ, and σ_θ are the radial, tangential and axial stresses in a cylindrical coordinate system with origin at the center of the central heater. The identification of the stress components mentioned above is basically correct except when the relative magnitudes of the components change with time. Examination of the predicted stress history indicates that this "cross-over" can occur. Therefore, in plotting the predicted and actual stresses using the LBL-CDC computer, we have labeled the different stress components separately. Except for this difference, the CDC stress plots are similar to the corresponding MODCOMP plots. An example CDC plot is shown in Figure C1. At any instant in time, the actual stresses should be compared to the predicted stresses according to the following scheme:

for a USBM gauge in a vertical hole, identify $S_p(S_q)$ with the greater (lesser) of σ_r and σ_θ;

for a USBM gauge in a horizontal hole, identify $S_p(S_q)$, with the greater (lesser) of σ_z and σ_θ

C.3. BOREHOLE DISPLACEMENT PLOTS

Although the biaxial strain approximation (1) used in the stress comparison above is usually adequate in mining applications, this may not necessarily be true with thermal stresses. A better and equally simple expression exists

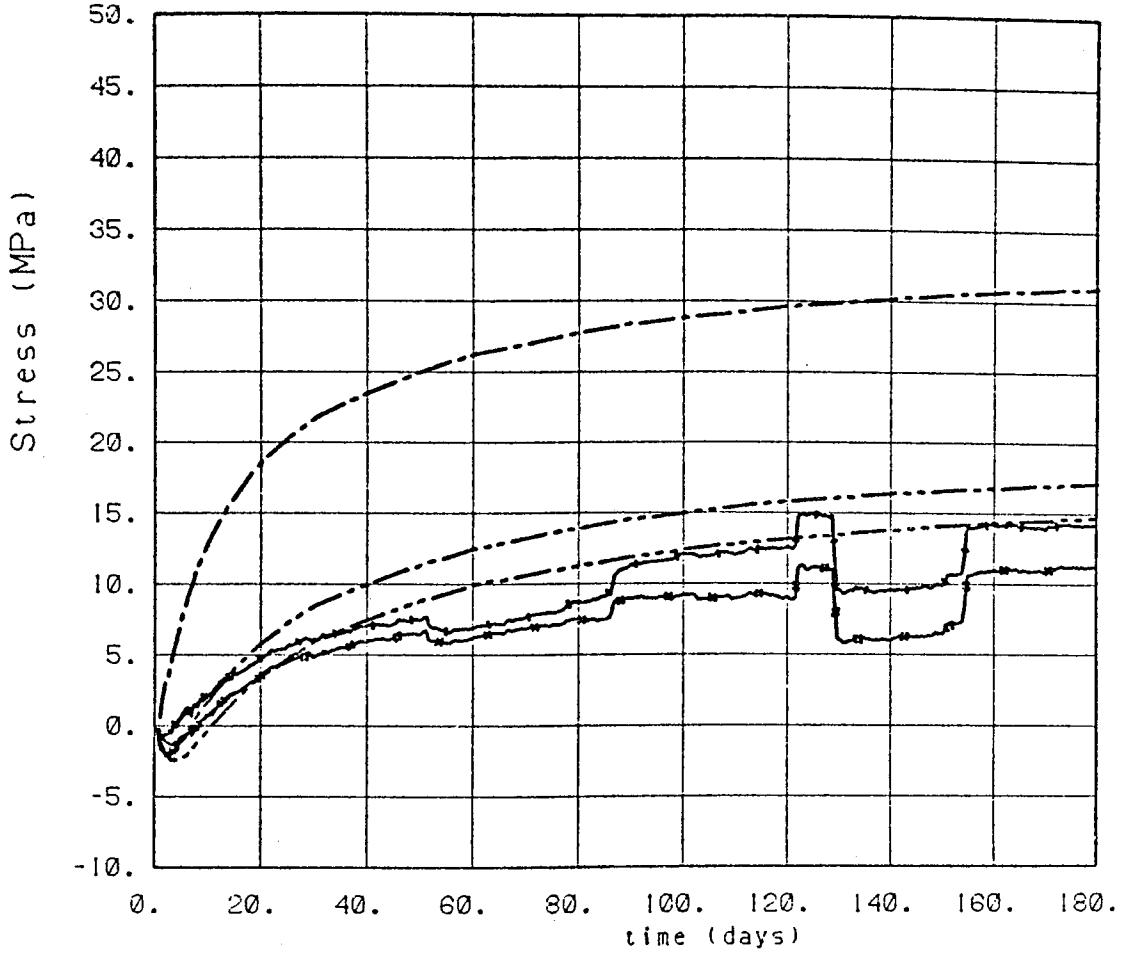

STRESS - USBM GAUGES

STRIPA FULL SCALE 2 - 5KW CENTRAL HEATER + PERIPHERALS

	instr		r	θ	z			
———	U24		2.00	-23.03	.66	S_{11} (σ_r) (MPa)		thy(1)
———	U24		2.00	-23.03	.66	S_{22} (σ_z) (MPa)		thy(1)
———	U24		2.00	-23.03	.66	S_{33} (σ_θ) (MPa)		thy(1)
——•——•——	U24	(744,745,746)	2.00	90.00	.85	S_P (MPa)		expt
——×——×——	U24	(744,745,746)	2.00	90.00	.85	S_Q (MPa)		expt

Theoretical model(s): (1) COMBINED

plotted 02/03/79 19.15.25 NPLOT43 - plot # 12

XBL 796-10414

Fig. C1. Predicted and measured stress history for a typical USBM gauge (U24) in the 5 kW experiment.

(Jaeger and Cook, 1976) relating the principal stresses S_1, S_2, S_3 (assumed to be applied from infinity) to the borehole displacement:

$$u = \frac{d}{E} (S_1 + S_2 - \nu S_3) + 2(1 - \nu^2)(S_1 - S_2) \cos 2\theta_p \qquad (C6)$$

with S_3 parallel to the axis of the hole. For the full-scale experiments and the sensor arrangements in the USBM gauges, the following equalities hold (either exactly or approximately)

Vertical holes

$$S_1 = \sigma_\theta, \quad S_2 = \sigma_r, \quad S_3 = \sigma_z$$

$$\theta_p = 0 \text{ for } u_1, \quad 60° \text{ for } u_2, \quad \text{and } 120° \text{ for } u_3.$$

Horizontal holes

$$S_1 = \sigma_\theta, \quad S_2 = \sigma_z, \quad S_3 = \sigma_r$$

$$\theta_p = 0 \text{ for } u_1, \quad 60° \text{ for } u_2, \quad \text{and } 120° \text{ for } u_3$$

Note that according to equation (C6), $u_2 = u_3$. Also, no prior assumption has been made regarding the relative magnitudes of S_1 and S_2.

A set of CDC plots has been made for the actual and predicted borehole displacements according to equation (C6). An example is shown in Fig. C2. While the discrepancies between theory and experiment appear to be similar for both Fig. C1 and Fig. C2 at first glance, a closer look reveals the agreement is in general better in the case of Fig. C2. It is therefore recommended that this set of plots, based on a closer approximation, should be used for quantitative comparison. The difference between the experimental u_2 and u_3 in Fig. C2 probably indicates anisotropy of the rock if the USBM gauge calibration is correct.

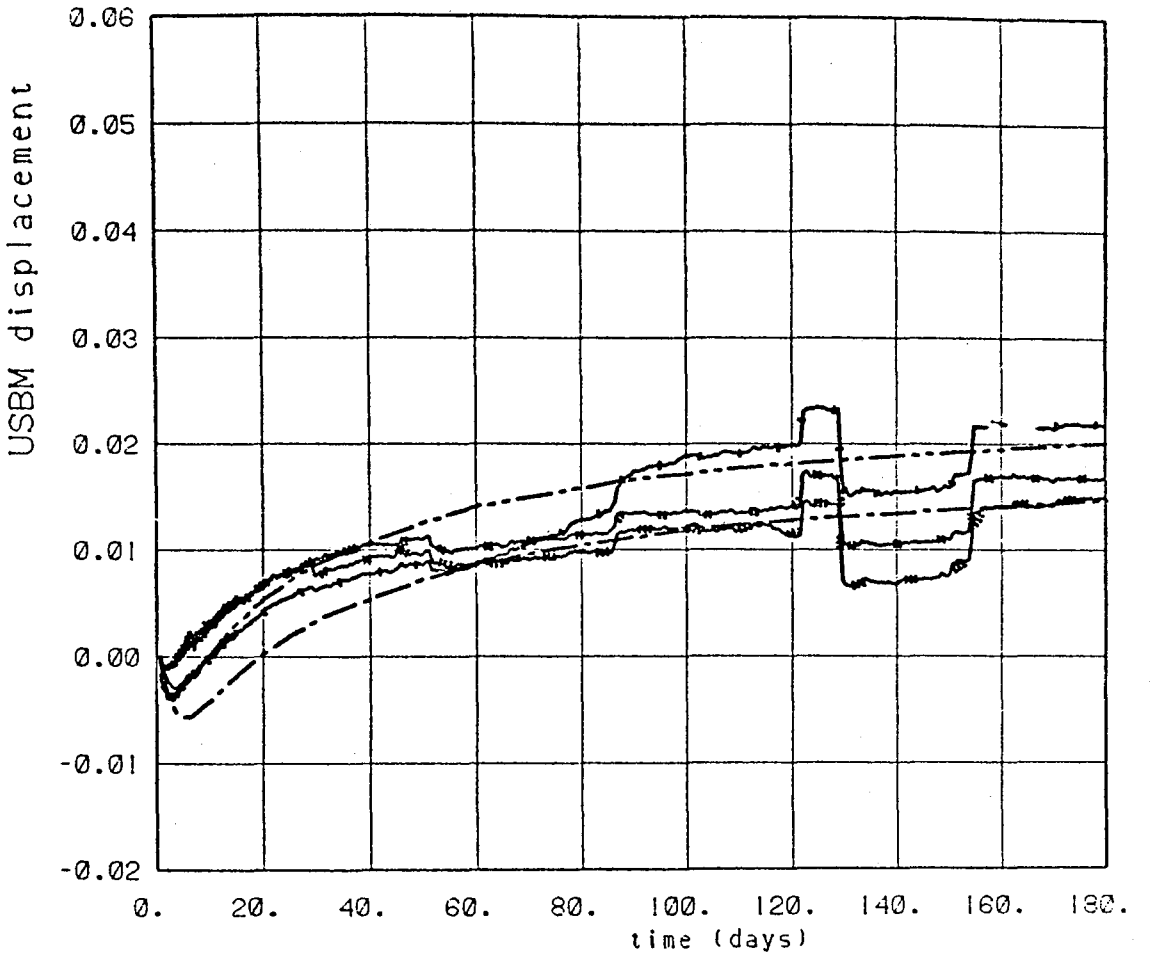

USBM GAUGE DISPLACEMENTS

STRIPA FULL SCALE 2 - 5KW CENTRAL HEATER + PERIPHERALS

	instr	r	θ	z			
——·——·——	U24	2.00	-23.03	.66	u_1	(mm)	thy(1)
——·——·——	U24	2.00	-23.03	.66	u_2	(mm)	thy(1)
——•——•——	U24 (744)	2.00	90.00	.85	u_1	(mm)	expt
——•——•——	U24 (745)	2.00	90.00	.85	u_2	(mm)	expt
——•——•——	U24 (746)	2.00	90.00	.85	u_3	(mm)	expt

Theoretical model(s): (1) COMBINED

plotted 02/03/79 19.14.03 NPLOT44 - plot # 12

XBL 796-10415

Fig. C2. Predicted and measured borehole deformation history for a typical USBM gauge (U24) in the 5 kW experiment. u_1, u_2, u_3 designate the change in borehole diameter in three different directions.

C.4. ERROR ESTIMATE

It is easy to understand why the difference between the biaxial and triaxial analyses is not always negligible. The borehole displacement obtained using equation (C6) differs from that given by equation (C1) by the amount

$$\frac{d}{E} = -\nu S_3 + \nu^2(S_1 + S_2) \qquad (C7)$$

which represents the Poisson effect. Comparing the leading terms in the expressions (C7) and (C1), it is seen that the fractional error introduced by omitting the effect of the stress component along the borehole axis is given approximately by the ratio

$$\frac{\nu S_3}{(S_1 + S_2)}$$

For hydrostatic state of stress, $S_1 = S_2 = S_3$, and $\nu = 0.23$ (the value used for the stress calculations), the error is about 11.5%, which is not very serious considering other possible sources of uncertainty. However, in the case of the horizontal USBM gauge U24 illustrated in Figs. C1 and C2, it is seen that S_3 ($= \sigma_r$) can be much higher than S_1 and S_2 so that, for examples, 20 days after the turn-on of the 5 kW heater, $S_3 \sim 2(S_1 + S_2)$ and the error is approximately 46%. This is probably one of the extreme cases. For other horizontal USBM gauges, the error may be smaller.

For the USBM gauges in vertical holes, the error introduced by using equation (C1) instead of equation (C6) is not significant since the principal stress along the axis of the hole is σ_z and

$$\frac{\sigma_z}{(\sigma_\theta + \sigma_r)} < \frac{1}{2}$$

for all these gauges.

A question that has not been addressed is the assumption of uniform stress around the USBM gauge borehole. Although the borehole diameter is small and the stress does not vary rapidly at the positions of these holes, a quantitative estimate is still desirable.

C.5. References

Jaeger, J. C. and Cook, N. G. W. 1976. Fundamentals of rock mechanics. 2nd. London: Chapman and Hall, London; New York: John Wiley and Inc.

Obert, L. and Duvall, W. I. 1967. Rock mechanics and the design of structures in rock. New York: John Wiley and Sons, Inc.

Schrauf, T. W., Pratt, H. R., Simonson, E. R., Hustrulid, W. A., Nelson, P., DuBois, A., Binnall, E., and Haught, R. 1979. Instrumentation evaluation, calibration, and installation for heater tests simulating nuclear waste in crystalline rock, Sweden. Lawrence Berkeley Labortory report LBL-8313 (in preparation). Berkeley, California.

This report is part of a cooperative Swedish-American project supported by the U.S. Department of Energy and/or the Swedish Nuclear Fuel Supply Company. Any conclusions or opinions expressed in this report represent solely those of the author(s) and not necessarily those of The Regents of the University of California, the Lawrence Berkeley Laboratory, the Department of Energy, or the Swedish Nuclear Fuel Supply Company.

TECHNICAL INFORMATION DEPARTMENT
LAWRENCE BERKELEY LABORATORY
UNIVERSITY OF CALIFORNIA
BERKELEY, CALIFORNIA 94720